Design Development of Brushless Doubly Fed Machines

by

Oreoluwa I. Olubamiwa

Dissertation presented for the degree of Doctor of Philosophy in Electrical Engineering in the Faculty of Engineering at Stellenbosch University

Supervisors:

Dr N. Gule
Prof. M. J. Kamper

April 2022

Declaration

By submitting this dissertation electronically, I declare that the entirety of the work contained therein is my own, original work, that I am the sole author thereof (save to the extent explicitly otherwise stated), that reproduction and publication thereof by Stellenbosch University will not infringe any third party rights and that I have not previously in its entirety or in part submitted it for obtaining any qualification.

Date: April 2022

Abstract

Design Development of Brushless Doubly Fed Machines

O.I. Olubamiwa

Department of Electrical and Electronic Engineering, University of Stellenbosch,
Private Bag X1, Matieland 7602, South Africa.

Dissertation: PhD

April 2022

Doubly fed induction generators (DFIGs) are the most widely used generators in large wind turbines, because of their cheap constructions, smaller converter sizes, and wide speed range. However, DFIGs have well known reliability issues stemming from their slip ring and brush failures. This is particularly problematic in remote areas like offshore wind sites. Currently, the operational and maintenance costs of DFIG based wind turbines are the highest among commonly used offshore wind topologies, due to the slip ring and brush failures. It should be noted that offshore wind power is getting increasing attention, and significant increases in offshore wind installations are projected in the coming years.

The use of brushless doubly fed (induction) machines (BDFMs) has been proposed as an alternative to DFIGs, especially in remote areas like offshore sites, as they do not have slip rings and brushes. BDFMs, which are typically medium speed machines, also have better low voltage ride through characteristics compared to DFIGs, which could help reduce cost and complexity of their drivetrains. However, BDFMs have a more complex structure to DFIGs, with considerably lower power densities. Also, BDFMs have higher total harmonic distortions and vibrations compared to DFIGs. With their development still being at experimental stages, there is no well-defined way to design BDFMs, with the design of certain parts still debated.

In this project, the start to finish design process of BDFMs is investigated. The thought process behind certain decisions like the placement of the stator windings are highlighted. The design of a suitable rotor topology per BDFM application is researched. The rotor design is conducted with power density and harmonics/vibrations considered.

A proper method for BDFM design evaluation is demonstrated especially when considering grid complaint operations. This evaluation method is compared with evaluation methods commonly used in available literature to demonstrate its suitability. With proper evaluation determined, the optimization of BDFM designs is investigated using different models. A coupled circuit model is developed for use in the rotor design. Results from finite element analysis models are used to develop response surface approximations which are coupled with a genetic algorithm for power density optimizations.

There are established values of certain input parameters such as the electric and magnetic loadings in DFIG design. This is however not the case with BDFMs. Consequently, in this project, practical values of these parameters are researched for different BDFM power ratings. The disparities in power density between BDFMs with different pole pair combinations and DFIGs at corresponding rated speeds across different power ratings are mapped out. These disparities in power density are used to recommend the best performing pole pair combinations at different power ratings.

Uittreksel

Ontwerpontwikkeling van borsellose dubbele gevoerd masjiene

(Design Development of Brushless Doubly Fed Machines)

O.I. Olubamiwa

Departement Elektries en Elektroniese Ingenieurswese, Universiteit van Stellenbosch,
Privaatsak X1, Matieland 7602, Suid Afrika.

Proefskrif: PhD

April 2022

Dubbel gevoerde induksie generators (DGIGs) word gereeld in groot wind turbines gebruik omdat dit goedkoop is om aan mekaar te sit, kleiner omskakelaar groottes het, en ‘n wye spoed verskeidenheid het. Ten spyte hiervan het DGIGs betroubaarheid probleme wat veroorsaak word deur die gly ring en borsel mislukkings. Dit is veral ‘n probleem in afgesonderde areas soos buitelandse wind plase. As gevolg hiervan is DGIG gebaseerde wind turbines se kostes die hoogste onder algemeen gebruikte buitelandse wind tipologieë. Dit is belangrik om in ag te neem dat daar meer aandag aan buitelandse wind krag gegee word en dus word daar ‘n beduidende toename in buitelandse wind installasies vir die komende jare geprojekteer.

Die gebruik van borsellose dubbel gevoerde (induksie) masjiene (BDGMe) is al as ‘n alternatiewe opsie vir DGIGs voorgestel, veral vir afgesonderde areas omdat hulle nie gly ringe of borsels het nie. BDGMe, wat tipies medium spoed masjiene is, het ook beter lae spanning rit deur eienskappe as DGIGs wat kan help om die kostes en kompleksiteit van die dryf stelsels te verminder. Daar moet egter in ag geneem word dat BDGMe ‘n baie meer komplekse struktuur het met laer krag digthede. BDGMe het ook hoër totale harmonieë versteurings en vibrasies wanneer dit met DGIGs vergelyk word. Met die masjiene se ontwikkeling wat nog in eksperimentele fases is, is daar nog nie ‘n goed-gedefinieerde manier om BDGMe te ontwerp nie, veral omdat sekere dele se ontwerpe nog gedebatteer word.

In die projek word die proses van BDGMe ontwerp van begin tot einde ondersoek. Die proses van sekere besluite wat gemaak is, soos die plasing van die stator windings, word uitgelig.

Die ontwerp van ‘n toepaslike rotor topologie per BDGM toepassing word ook in die studie nagevors. Die rotor ontwerp is met die inagneming van krag digtheid en harmonieë/vibrasies uitgevoer. ‘n Gepaste metode vir die evaluering van BDGM ontwerp is gedemonstreer, veral wanneer krag-netwerk voldoende bedrywighede in ag geneem word. Die evaluasie metode is met ander metodes wat algemeen in beskikbare literatuur gebruik word vergelyk om die geskiktheid daarvan te demonstreer. Met die gepaste evaluasie wat bepaal is, is die optimalisering van BDGM ontwerpe ondersoek deur gebruik te maak van verskeie modelle. ‘n Gekoppelde baan model is vir die gebruik in rotor ontwerp ontwikkel. Resultate van beperkte element analise modelle is gebruik om reaksie oppervlak benaderings te ontwerp wat aan die genetiese algoritme vir krag digtheid optimaliserings ontwikkel is.

Daar is bepaalde waardes van sekere inset parameters, soos die elektriese en magnetiese ladings in die DGIG ontwerp. Dit is egter nie die geval vir BDGMe nie. As gevolg hiervan word daar in die projek praktiese waardes van die parameters vir verskillende BDGM krag graderings nagevors. Die ongelykhede in krag digtheid tussen BDGMe met verskillende pool paring kombinasies en DGIGs teen ooreenstemmende gegradeerde spoed oor verskillende krag graderings is uiteengesit. Die ongelykhede is gebruik om die beste pool paring kombinasies teen verskillende spoed graderings voor te stel.

Acknowledgements

I would (in no particular order) like to express my sincere appreciation to the following people and organisations

- My supervisor **Dr Nkosinathi Gule** for his invaluable supervision, and creating a conducive environment for me to thrive with my research. My Co supervisor **Prof. Maarten J. Kamper** for his meticulous oversight, and efforts in getting funding for my research.
- Mr P. Petzer, Andre Swart, Howard Koopman, Kenan Cloete and Kenan Fillies for their kind assistance during the construction and testing of my prototype.
- My parents **Dr Olayiwola** and **Mrs Abiodun Olubamiwa** for their prayers, encouragement, and support. God bless you.
- My colleagues at the EMLab for great times. Thanks Dr (MK) Mabhula, Hannes Labuschagne, Dillan Ockhuis and Stephan Botha for countless relevant discussions and contributions. Special thanks to **Tainton Hutton** for the development of a control system to test my prototype.
- My siblings **Tolu** and **Tinu Olubamiwa** for their support and encouragement, big hugs to you! Thanks **AyoOluwa Aderibigbe** for cheering me on, was lekker having someone to compare final year PhD notes with.
- The Centre for Renewable and Sustainable Energy Studies (CRSES) for providing financial support.

Blessed be the name of God forever and ever, for wisdom and might are His.

List of Publications

Local Conferences

1. O. I. Olubamiwa and N. Gule, “Rotor selection for brushless doubly fed machines using coupled circuit models,” in *Southern African Sustainable Energy Conference (SASEC) 2021*, Stellenbosch, November 2021.

International Conferences

1. O. I. Olubamiwa and N. Gule, “Prioritizing power factor in power density assessments of doubly fed induction generator alternatives,” in *2020 International Symposium on Power Electronics, Electrical Drives, Automation and Motion (SPEEDAM)*, June 2020, pp. 47-52.
2. O. I. Olubamiwa and N. Gule, “Design and optimization of a cage + nested loops rotor BDFM,” in *2020 International Conference on Electrical Machines (ICEM)*, vol. 1, August 2020, pp. 1868-1874.

Journal Publications

1. O. I. Olubamiwa, N. Gule, and M. J. Kamper, “Coupled circuit analysis of the brushless doubly fed machine using the winding function theory,” *IET Electric Power Applications*, vol. 14, pp. 1558-1569(11), September 2020.
2. O. I. Olubamiwa and N. Gule. “ Review of the Advancements in the Design of Brushless Doubly Fed Machines”. *Energies*, vol. 15, no.3, pp 725, January 2022.

Contents

List of Figures

List of Tables

Nomenclature

Acronyms

BDFIM	Brushless doubly fed induction machine
BDFM	Brushless doubly fed machine
Cage+NL	Combination of nested loops and a cage
CC	Coupled circuit
CW	Control winding
DD	Direct drive
DFIG	Doubly fed induction generator
DFIM	Doubly fed induction machine
DOE	Design of experiment
EEC	Electric equivalent circuit
EESG	Electrically excited synchronous generator
Ef	Efficiency
FEA	Finite element analysis
IL	Isolated loop
IM	Induction machine/motor
LHS	Latin hypercube sampling
LVRT	Low voltage ride through
MEC	Magnetic equivalent circuit
MMF	Magnetomotive force
NL	Nested loop
NSGA-II	Non-dominated sorting genetic algorithm
O&M	Operational and maintenance

PD	Power density
Pf	power factor
PMSG	Permanent magnet synchronous generator
PW	Power winding
RDFIG	Rotor-tied doubly fed induction generator
RSA	Response surface approximation
SCIG	Squirrel cage induction generator
SW	Series wound
UMP	Unbalanced magnetic pull
WF	Winding function
WFT	Winding function theory

BDFM design parameters

α	Rotor loop span	
$\bar{B}$	BDFM specific magnetic loading	T
λ	Stack length ratio	
ϕ_i	Flux produced in winding i	Wb
τ_i	Pole pitch of winding i	T
B_1	Power winding magnetic loading	T
B_2	Control winding magnetic loading	T
B_c	Core flux density	T
B_t	Teeth flux density	T
b_t	slot teeth width	mm
B_{sum}	Maximum BDFM airgap flux density	T
D	Airgap diameter	mm
g	Airgap length	mm
h_c	core height	mm
J_1	Power winding electric loading	kA/m
k_{wi}	Winding factor of winding i	
l	Stack length	mm
N_{cw}	Control winding turns per phase	

N_i	Number of turns per phase of winding i	
N_{pw}	Power winding turns per phase	
N_r	Number of rotor slots	
n_{s1}	Number of power winding turns per slot	
n_{s2}	Number of control winding turns per slot	
N_s	Number of stator slots	
p_1/p_2	Pole pair combination	
p_1	Power winding pole pairs	
p_2	Control winding pole pairs	
q	Stator slots per pole per phase	
q_r	Number of rotor loops per nest	
r	Airgap radius	mm
ω_1	Power winding field angular speed	rads^{-1}
ω_2	Control winding field angular speed	rads^{-1}
$\omega_{\mathrm{r_f}}$	Rotor field angular speed	rads^{-1}
ω_{r}	Rotor mechanical angular speed	rads^{-1}
ω_n	BDFM natural speed	rads^{-1}/rpm
f_1	Grid frequency	Hz
f_2	Maximum control winding frequency	Hz
I_1	Power winding maximum current	A
I_2	Control winding maximum current	A
P_{cw}	Control power winding power	kW
P_{pw}	Maximum power winding power	kW
P_t	Total power rating	kW
V_1	Grid voltage	V
V_2	Maximum control voltage	V

Constants

μ_0	Permeability of free space	1.256 x 10^{-6} H/m

Coupled/Equivalent circuit parameters

$\boldsymbol{\lambda}_p$	Power winding flux linkage matrix	
$\boldsymbol{\lambda}_r$	Rotor loops flux linkage vector	
$\boldsymbol{I}_c$	Control winding current vector	
$\boldsymbol{I}_p$	Power winding current vector	
$\boldsymbol{I}_r$	Rotor current vector	
$\boldsymbol{L}_{cr}$	Mutual inductance matrix between the control winding and rotor loops	
$\boldsymbol{L}_{pr}$	Mutual inductance matrix between the power winding and rotor loops	
$\boldsymbol{L}_p$	Power winding inductance matrix	
$\boldsymbol{L}_r$	Rotor loops inductance matrix	
$\boldsymbol{R}_p$	Power winding resistance matrix	
$\boldsymbol{R}_r$	Rotor loops resistance matrix	
$\boldsymbol{V}_p$	Power winding voltage vector	
$\boldsymbol{V}_r$	Rotor loops voltage vector	
$\mathrm{h_{cw}}$	Control winding harmonics	
$\mathrm{h_{pw}}$	Power winding harmonics	
L_{er}	Cage rotor upper end ring segment leakage inductance	H
L_e	Lower rotor end ring segment leakage inductance	H
L_{sr}	Mutual inductance between arbitrary stator winding and rotor loop	H
R_b	Rotor bar resistance	Ω
R_{er}	Cage rotor upper end ring segment resistance	Ω
R_e	Lower rotor end ring segement resistance	Ω
R_{ri}	Resistance of ith loop	Ω
T_e	Electromagnetic torque	Nm

Symbols

$\langle n(\theta) \rangle$	Average turns function
$N(\theta)$	Winding function
$n(\theta)$	Turns function

Chapter 1

Introduction

From a public perspective, renewable energy usage is almost unanimously encouraged for different reasons. Health considerations from reduced pollution, climate change check, increased energy reliability and resilience are among the reasons listed in [1]. As a result, the adoption of renewable energy has experienced rapid growth in recent years. In 2005, renewable energy (excluding hydro power) accounted for about 2.65 % of global power generating capacity [2]; by 2020, this percentage had grown to about 11.4 % [1].

Although solar PV has registered as the fastest growing renewable energy sector in recent times, wind energy retains the top spot in terms of global renewable capacity, accounting for about 22 %. Wind energy is also the second fastest growing sector [1]. There is a forecasted increase in offshore wind installations in the coming years, to the extent that offshore wind is expected to contribute about 15 % in new wind energy installations for the next five years [3]. Previously, offshore wind accounted for about 4 % of global wind capacity [3].

Wind turbines, which are used to harness wind energy, generally consist of a generator, gearbox (except in direct drive systems), power electronic converters and a transformer. In this chapter, generator technologies employed in wind turbines are briefly discussed, culminating in the introduction of brushless doubly fed (induction) machines (BDFIMs/BDFMs). The objectives set out for this study are then delineated, after which the dissertation outline is presented.

1.1 Wind turbine generators

Depending on the specific design requirements, wind turbines are operated at either fixed speeds or with variable speed capabilities. Fixed speed turbines are typically associated with squirrel cage induction generators (SCIGs), while a variety of generators are used in variable speed turbines. Modern wind turbines are commonly operated at variable speeds because

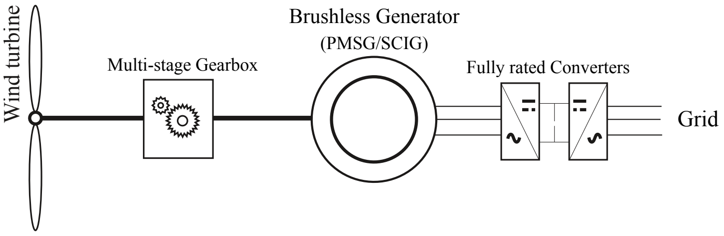

Figure 1.1: *Geared brushless generator drivetrain*

of the advantages of cost effectiveness, islanding capabilities, decreased mechanical stresses, improved power quality, and increased efficiency [4, 5]. The tip speed ratio in wind turbines can be kept constant for variable speed operations, and this helps in maximizing the harnessed wind energy [4].

The common variable speed wind turbine topologies include geared brushless generators with fully rated converters, direct drive systems, and doubly fed induction generators (DFIGs) with fractionally rated converters [4]. A review of the topologies is given in the following subsections.

1.1.1 Geared brushless generator with fully rated converters

In this topology as illustrated in Figure 1.1, a permanent magnet synchronous generator (PMSG) or squirrel cage induction generator (SCIG) is employed with a fully rated converter. The absence of slip ring and brush assemblies leads to high reliability. Although, synchronous generators can be PMSGs or electrically excited synchronous generators (EESGs), EESGs require slip rings and brushes, and are therefore not in this classification.

PMSGs have high power densities, and superior efficiencies compared to other generators due to the absence of field winding losses [4]. However, the permanent magnets and fully rated converters used give rise to a costly setup in PMSG based drivetrains. Also, synchronous generators exhibit low damping, so gusts of wind are not always effectively absorbed [6]. SCIGs have robust structures at relatively low costs compared to PMSGs. SCIGs also have high damping allowing for better rotor speed fluctuation and drive transient absorption [6].

1.1.2 Direct drive systems

Direct drive (DD) systems use synchronous generators with fully rated converters. DD systems are illustrated in Figure 1.2. Early DD systems in the 90s used EESGs, as permanent magnets were expensive. The recent resurgence of DDs stems from the push for increased reliability in wind turbines. DDs have a potential to achieve less maintenance downtime by

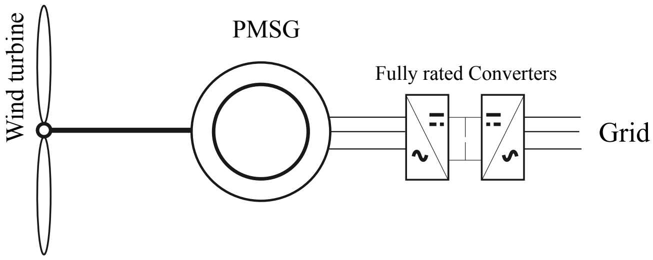

Figure 1.2: *Direct drive generator drivetrain*

avoiding the use of gearboxes. However, in the absence of gearboxes, the low speed generators required in DD systems are costly, bulky and have lower efficiency than other higher speed generators [4]. As a result, recent DD systems use PMSGs which are brushless, and typically high in power density and efficiency.

1.1.3 Doubly fed induction generator systems

Doubly fed induction generators (DFIGs) are the most commonly used generators in medium and large wind turbines. DFIGs are wound rotor induction machines which have their stator windings connected to the grid and their rotor windings also connected to the grid via fractionally rated power converters. The DFIG based wind turbine drivetrain is illustrated in Figure 1.3. Slip ring and brush assemblies provide access to the rotor windings to facilitate the adjustment of rotor current magnitude, frequency and phase angle. As a result, DFIGs can be operated over a wider speed range compared to SCIG based drivetrains.

Other advantages of DFIGs include low cost compared with PMSGs, easily implemented power factor control, less mechanical stresses and power fluctuations [5]. The power converters used with DFIGs, which are fractionally rated, have lower converter losses compared to fully rated converters used with SCIGs and PMSGs.

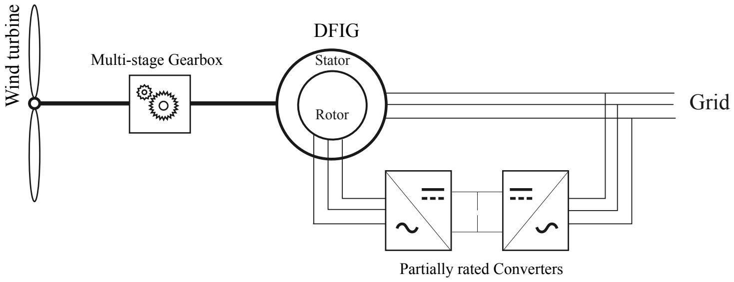

Figure 1.3: *Geared DFIGs with partially rated converters*

DFIGs tend to have less reliability than other commonly used wind turbine generators [7]. This is due to the slip ring and brush assemblies in DFIGs which have to be frequently maintained. This is particularly problematic in remote areas like offshore sites for wind turbines. Operational offshore wind expenditure is estimated at about 30 % of the cost of energy in [4], and mitigating failures could significantly reduce the offshore generation costs. Also, operational and maintenance (O&M) costs are critical factors in the selection of wind turbine drivetrains in offshore sites, and DFIG based wind turbines currently have the highest O&M costs [8].

The brushless DFIG (BDFIG/BDFM) is an alternative to conventional DFIGs with potentially higher reliability, as slip ring and brush assemblies are avoided. BDFMs and DFIG drivetrains operate similarly, as they employ the use of fractionally rated converters. The better low voltage ride through performances of BDFMs could also reduce cost and complexity in drivetrain setup [4]. With the combination of an increasing push for renewable energy adoption, and a growing trend of offshore wind turbine installations, brushless doubly fed machines (BDFMs) are well positioned to find relevance in the coming years. However, BDFMs have a more complex structure than DFIGs, and are yet to be commercialized.

1.2 Overview of BDFMs

BDFMs are typically medium speed generators due to the pole addition aspect in the doubly fed synchronous mode, thereby reducing the number of gearbox stages required and thus the drivetrain reliability. This however is not necessarily an advantage over conventional DFIGs with similar rated speeds. A BDFM based wind turbine drivetrain is illustrated in Figure 1.4. In the following subsections, an overview of the BDFM structure and modes of operation is given.

1.2.1 BDFM Structure

The contemporary version of BDFMs consists of a stator having two windings, and a special rotor. The stator primary/power winding (PW) with p_1 pole pairs, bears the bulk of the BDFM power, and is connected directly to the grid. The secondary/control winding (CW) with p_2 pole pairs, is connected to the grid via fractionally rated power converters. The stator windings are wound such that $p_1 \neq p_2$ to avoid direct coupling. Instead, the individual stator windings directly couple with the rotor, which facilitates cross-coupling between the two windings [9–11]. Different types of rotors have been proposed for BDFMS, but the most commonly seen in literature is the nested loop (NL) rotor [12].

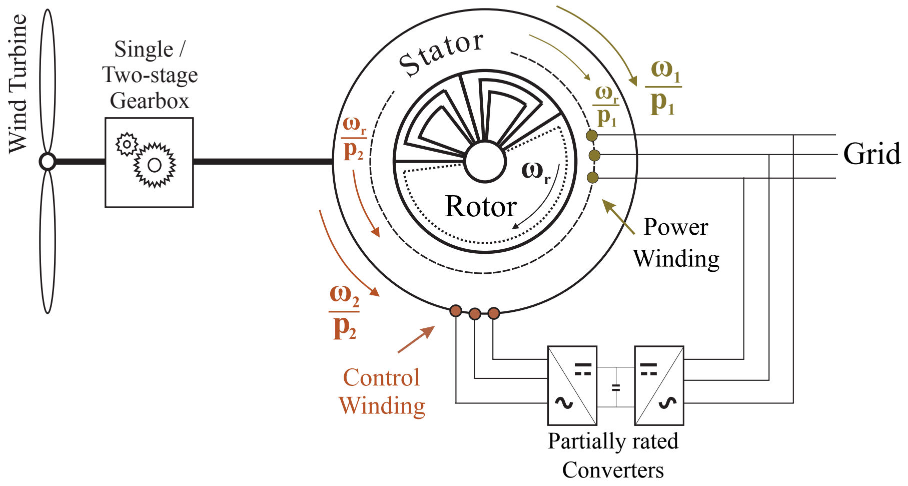

Figure 1.4: *BDFM synchronous mode of operation*

1.2.2 BDFM Modes of Operation

BDFMs are capable of different modes of operations including the single fed (simple induction) mode, the cascade operation and the doubly fed operation. In the single fed operation, only one of the stator windings is energised with the other open circuited. The machine in this mode behaves like an induction machine with the number of poles of the energised winding. The performance is however relatively poor [13].

In the cascade operation, one stator winding is connected to a mains supply while the other is short circuited. In this mode, the machine performs like an induction machine with $p_1 + p_2$ pole pairs [14]. The simple induction and cascade modes are both asynchronous in nature as the loading determines the mechanical speed of the machine [13].

The doubly fed operation in which both stator windings are energised, can either be asynchronous or synchronous. In the asynchronous mode, both stator windings work against each other with consequent undesirable torque and speed oscillations [14].

The synchronous doubly fed mode is the mode desirable for wind turbine drivetrains as illustrated in Figure 1.4. The synchronous doubly fed mode is put into effect by the rotor cross-coupling the two stator windings. In this mode, the machine operates with a constant torque [13]. The mechanical rotor angular speed, (ω_r) in this mode is calculated as

$$\omega_r = \frac{\omega_1 + \omega_2}{p_1 + p_2}, \tag{1.2.1}$$

where, ω_1 & ω_2 are the electrical frequencies of PW and CW respectively. The CW frequency is at slip frequency in the synchronous mode, similar to DFIGs. The BDFM ”natural” speed,

ω_n, which is analogous to the synchronous speed of a DFIG is given as

$$\omega_n = \frac{\omega_1}{p_1 + p_2}. \tag{1.2.2}$$

It should be noted that at this speed, the CW is fed with DC, i.e $\omega_2 = 0$. The BDFM operation at its natural speed is similar to a DFIG at synchronous speed such that the CW neither absorbs nor generates power. The rotor field frequency (ω_{r_f}) is

$$\omega_{r_f} = \omega_1 - p_1\omega_r = -\omega_2 + p_2\omega_r. \tag{1.2.3}$$

In this study, identified problematic aspects of the BDFM design are investigated. These challenges investigated, and the objectives pursued are outlined in sections 1.3 & 1.4 respectively.

1.3 BDFM design challenges considered

In recent times, improvements in design and control methods are gearing BDFMs towards commercial feasibility. In the build up to this, different aspects of the BDFM design require further research, and the specific areas being considered in this study include the following.

- Comprehensive design processes of IMs/DFIGs machines are available in chapters of books like [15–18] to mention a few. These provide detailed start to finish guides and information about the design of IMs/DFIGs. On the other hand, literature dealing with the design of BDFMs typically deal with specific design sections, without direct unification to other sections. Also, BDFM design is not yet at an established level, and a lot of design development is still ongoing. Therefore, there is no fixed or unified design procedure at present.

- Two rotor types, the nested loop (NL) and cage+NL rotors are the most commonly used BDFM rotors because of their robust structure and ease of manufacture [12]. In some cases, cage+NL rotors have less impedance than NL rotors [19–21], however, NL rotors are still more widely used [12]. Further investigation is needed to determine suitability of either rotor type per application. Also, the number of rotor loops per nest for either rotor type needs a closer investigation. Although more loops per nest help to reduce the rotor harmonic inductances [10], too many loops per nest can lead to saturation.

- Prevalent power (density) evaluation methods of BDFM designs in available literature are sometimes flawed in predicting suitable BDFM designs for wind turbine operations. In some cases, motoring performances are used in evaluation, while maximum generating torque performances are considered in other cases. The power factor at operating points is often conspicuously missing, and this is potentially problematic, considering grid code requirements.

- The stack aspect ratio, electric loading and airgap flux density are very critical variables to consider in BDFM design. However, there is a general lack of information about specific values of these variables at different power ratings.

- One of the reasons hampering the commercialization of BDFMs is the reduction in power ratings compared with similarly sized DFIGs. The estimate from equivalent circuit deductions stands at about a quarter reduction in rating [22]. Potential MW rated BDFM drivetrains are compared with conventional DFIG and PMSG drivetrains in [23], and the difference between the highlighted BDFM and DFIG designs is higher than a quarter of ratings. However, the capital expenditure and efficiency of these drivetrains were the focus of comparison. A broader comparison of BDFM and DFIG power densities across different power ratings is required in painting a clearer picture of the discrepancy in BDFM power density.

- The choice of pole pair combinations for BDFMs transcends desired speed. Performances such as torque density, harmonics and efficiency are major factors in the selection. Presently, there is no clear favorite pole pair combination among researchers. The $p_1/p_2 = 2/4$ combination is used in the largest BDFM prototype built to date [24], while multiples of the $p_1/p_2 = 2/3$ combination have been shown to perform quite well.

1.4 Study objectives

In light of the challenges highlighted in the previous section, the following objectives are sought in this study.

- Given that the BDFM design process is still undergoing rapid development, a comprehensive review of the BDFM design development is presented. Current conventional BDFM structures are highlighted, and the thought process behind their prevalent usage is discussed. Noteworthy BDFM design procedures in available literature are also featured.

- The development of a quick analytical (coupled circuit) model to aid in the BDFM rotor topology (type and number of loops) selection is presented. The model application in evaluating potential rotor topologies per specific BDFM application is demonstrated, from which the best performing topology can be selected. The calculation of the NL and cage+NL loop currents is also considered in the analytical model.

- A proper context for BDFM power density evaluation is described, with proper considerations for grid side power factor, and synchronous doubly fed generating operations.

- The development of a design process for optimizing the power density and efficiency of BDFMs at a particular power rating will be highlighted. This design process will incorporate the developed coupled circuit model to determine an appropriate rotor topology. An optimization process is then used to determine design variable values for optimal performance.

- Specific values for variables such as the stack aspect ratio, electric loading and airgap flux density are usually determined based on empirical data. Such data is unavailable for BDFMs, as only a handful of BDFM designs are reported in literature. However, suitable ranges across different power ratings are investigated in this study. Design optimization data will be used to determine these ranges.

- A comparison of BDFM and DFIG power densities across different power ratings is presented. Pareto fronts from optimizations are used as basis for these comparisons. The relative performance of BDFMs with different pole pair combinations to DFIGs at corresponding rated speeds, is used to investigate suitable pole pair combinations.

1.5 Dissertation Layout

The subsequent chapters are outlined as follows:

- In **Chapter 2**, a review of BDFM design is presented. The evolution of BDFMs is detailed, and different aspects of BDFM design from literature are reviewed.

- In **Chapter 3**, a BDFM coupled circuit model using the winding function theory to calculate the machine inductances, is presented. Machine design related applications of this model are highlighted.

- In **Chapter 4**, proper evaluations of BDFM designs are investigated, and it is illustrated how assessments without power factor and relevant operating mode considerations can be insufficient.

- In **Chapter 5**, a methodical approach to BDFM design and optimization is presented.

- In **Chapter 6**, BDFM designs with different pole pair combinations and power ratings are compared with DFIGs with similar speeds and power ratings.

- In **Chapter 7**, contributions of this study, conclusions, recommendations and future directions are discussed.

Chapter 2

A review on the design development of BDFMs

2.1 Introduction

Doubly fed induction generators (DFIGs) are the most widely employed generators in medium and large wind turbines, but due to slip ring and brush problems, DFIG based wind turbines have the highest operational and maintenance (O&M) costs [8]. Brushless doubly fed machines (BDFMs) have similar advantages with DFIGs, and the absence of slip ring and brush assemblies would improve their reliability [25], thereby potentially reducing the O&M costs of wind turbine drivetrains using BDFMs.

Although BDFMs are being researched as alternatives to DFIGs to achieve better reliability, their development can be traced to machines preceding DFIGs. The applications of BDFMs have also shifted significantly from the original applications of their predecessors. In light of these, the historical evolution of BDFMs is first outlined to paint a clear picture of the design development of BDFMs.

BDFMs have more complex structures compared to DFIGs, with accompanying design related problems. Also, it was noted in [26] that there was a dearth of BDFM design studies in literature. This still rings true if one considers the vast array of available literature with comprehensive information on the design of conventional machines, like [16–18] to mention a few. However, there are quite a number of articles dealing with aspects of BDFM design, and these are summarized in a topical review on the design of BDFMs.

It is recognized, that reviews on BDFMs are available in literature such as [12, 27, 28]. These listed reviews are multifaceted, in that different aspects of BDFMs are covered, including brief histories, electromagnetic design, modelling techniques, modes of operation, and control strategies. Consequently, condensed essays of the different aspects of BDFMs are given. Doubly fed reluctance machines are also discussed in these reviews. However in this chapter, there is a comprehensive focus on the advancement and procedures involved in the design of BDFMs. Doubly fed machines with reluctance rotors, hybrid rotors and dual stators are not considered in this chapter. Whereas the available BDFM reviews serve as valuable overviews on BDFMs, this review can be a beneficial resource/guide for researchers interested in the design of BDFMs.

This chapter is divided into two main sections:

1. The evolution of cascaded IMs to contemporary BDFM topologies. In this section, significant contributions to the present day BDFM topologies are highlighted, with the underlying reasons for these design developments, and their impact on modern day BDFMs.
2. A comprehensive run-down of recent developments in the design of BDFMs, and design approaches employed in available literature.

2.2 Development of BDFMs from cascade Induction Motors

At the turn of the 19th century, polyphase induction motors were gaining traction in industry usage. As seen in [29], there were good reasons for this; simplicity and reliability of induction motors being key factors. However, this was before the advent of power electronics, and variable speed motor operations commonly employed direct current motors [30, 31]. Induction motors were also used for variable speed operations, howbeit with the use of rheostatic control, with analogous performances to shunt motors [31], which have significant losses [32].

Similarly in [33], it was indicated that Squirrel cage induction motors (SCIMs) were preferred in environments where rough and rigorous handling of equipment were required, like in mining industries. However, SCIMs were only relevant for constant speed and moderate starting torque operations. Instead, wound rotor (slip ring) induction motors with rheostats seem to have been used for variable speed applications at the time, as alluded to in [34, 35].

In the pursuit of short-circuited rotor type machines like SCIMs with characteristics comparable to slip ring IMs, cascade induction motors were developed [33, 35]. This systems consisted of two or more motors having a common connecting shaft. A good example of these cascade systems is the Steinmetz cascade IM system which was patented in 1897 [36]. These motors were connected according to different configurations to achieve different speed and power configurations. Examples of these connections are illustrated in Figure 2.1. In Figure

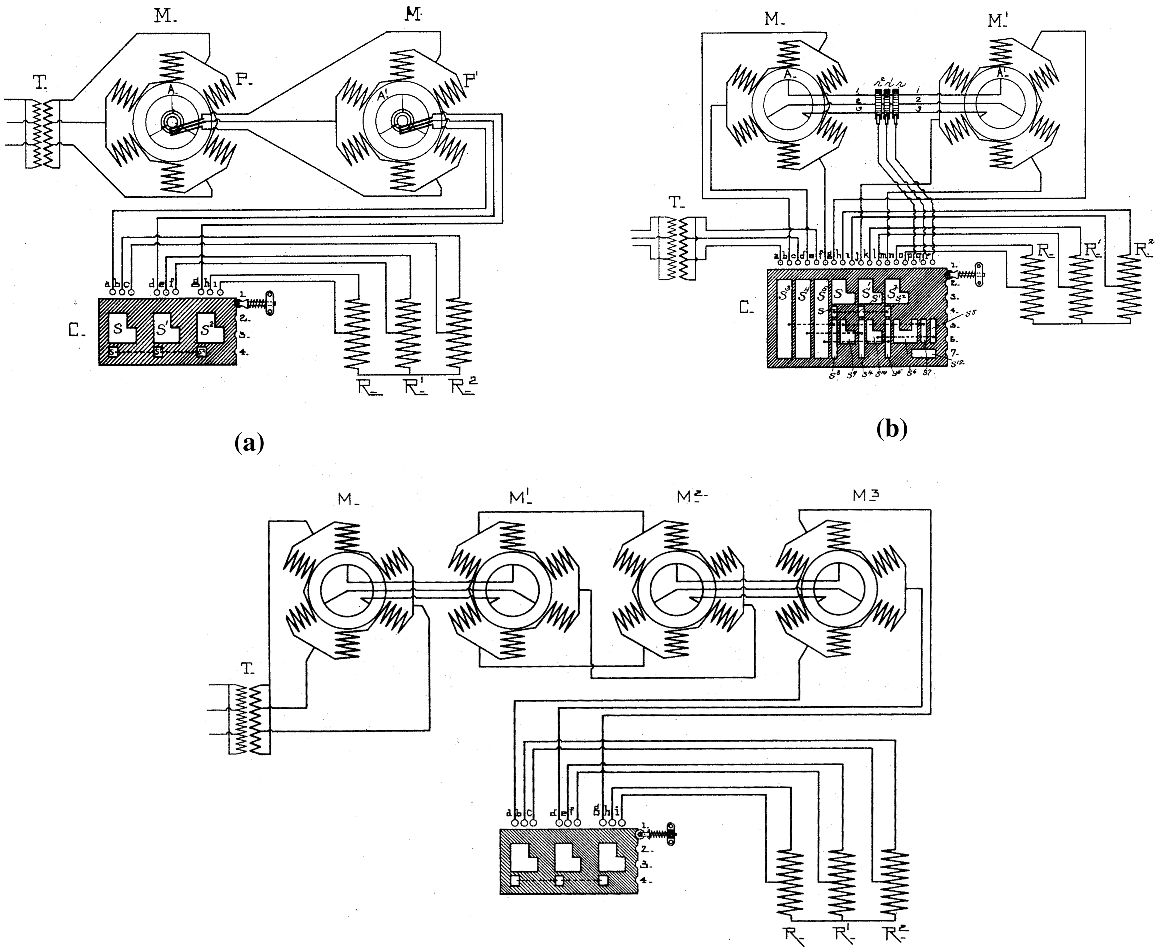

(a)

(b)

(c)

Figure 2.1: *Steinmetz cascade system examples (a) two motors with rotor of primary motor connected to secondary stator, (b) two motors with both rotors connested to each other, (c) four motors [36].*

2.1(a), the stator of the secondary motor is connected to the rotor of the primary motor. By this connection, a starting torque almost double one of the motors is achievable without the losses common with rheostatic controls. The connection in Figure 2.1(b) enables speed control capabilities similar to the series-parallel control of DC motors; likewise Figure 2.1(c), with more options [36].

Cascade systems however had disadvantages of high cost, low efficiency, low power factor, and poor overload capacity [35]. Over time, different machines were designed with inspiration from cascade systems, from which modern day BDFMs eventually developed. In the following subsections, distinct pioneering machines are highlighted, with their major contributions to the development of BDFMs underscored. A summary of the shift from cascade operations to synchronous doubly fed operations is also given.

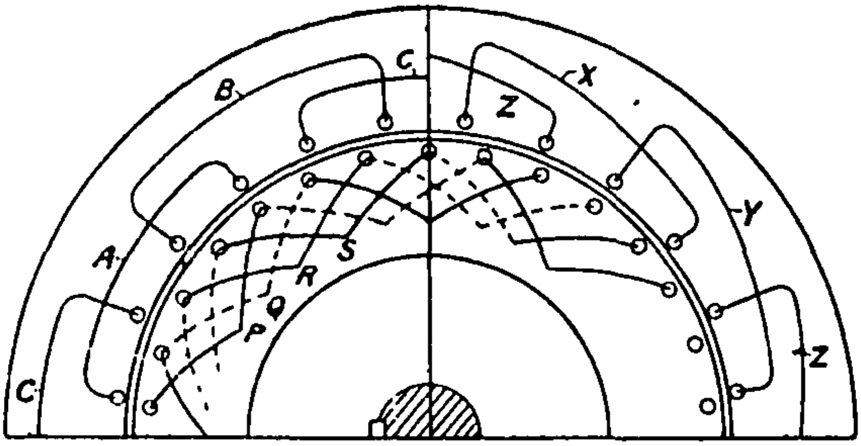

Figure 2.2: *Winding arrangement in the Thompson motor [35].*

2.2.1 The Thompson motor

A motor patented by S. Thompson in 1901 was highlighted in [35] as essentially being equivalent to a two motor cascade. The stator was divided into segments occupied by the primary and secondary windings. Alternate segments had different windings preventing mutual induction, as illustrated in Figure 2.2. The primary windings were connected directly to the main supply, while the secondary windings were connected to regulating resistances. The rotor had a wave winding which coupled with the primary stator field and induced a field on the secondary stator winding. Placing all the windings on one core was to reduce the setup cost, as opposed to two separate machines connected in cascade. The Thompson motor helped shape the shift from multiple motors in a cascade system to a single motor with cascaded operations.

2.2.2 The Lydall motor

A patent for a polyphase motor which could be operated at three speeds without rheostatic loss was accepted in 1903 [34]. This motor was developed by the Siemens brothers & Co. Limited and Francis Lydall, with two stator windings which had different pole numbers preventing direct inductive coupling. The rotor also had two windings wound in similar fashion as the stator, with connections made possible by slip rings. In Figure 2.3 is an illustration of the stator and rotor connections of this motor as given in [34]. Two different speeds could be obtained by short-circuiting either rotor (windings') set of slip rings $(R^1, R^2, R^3)/(r^1, r^2, r^3)$. A third (cascade) speed could be obtained by connecting the first rotor winding (R^1, R^2, R^3) to the second stator winding (a^1, a^2, a^3), or connecting both rotor windings together and short-circuiting the second stator winding [35].

The difference in pole numbers made segmentation of the stator windings unnecessary, as one

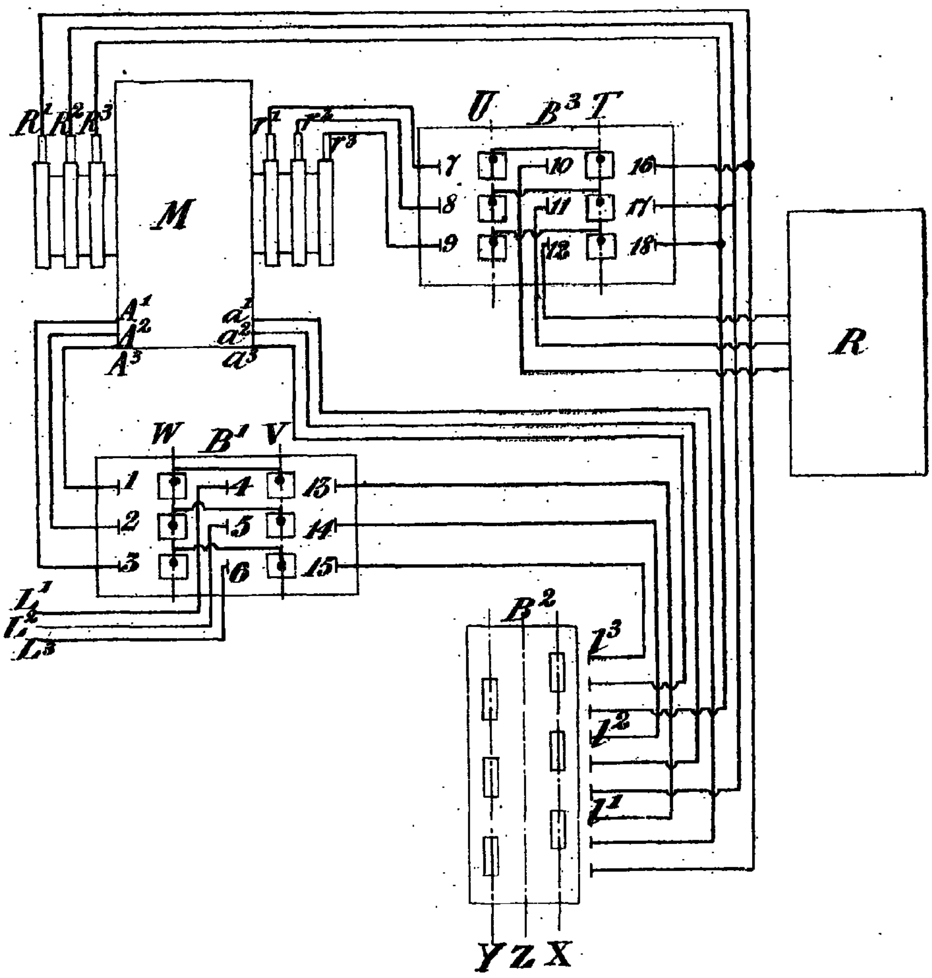

Figure 2.3: *Stator and rotor connections in the Lydall motor [34].*

could be placed on top the other. However there was increased copper losses from the two sets of windings (on the stator and rotor), and increased magnetic leakage due to deeper slots, and especially from the winding farthest from the air-gap [35]. Despite this, it should be noted that present day BDFMs use the Lydall type of stator, with windings of different pole numbers; one on top of the other.

2.2.3 The Hunt motor

L.J. Hunt introduced a cascade motor in [35] with single stator and rotor windings. This motor had regulating resistances connected to tappings on the stator winding, and could avoid the use of slip rings. Slip rings could however be employed if more efficient speeds were desired. The special stator winding allowed for reduction of magnetic leakage and copper losses incurred by

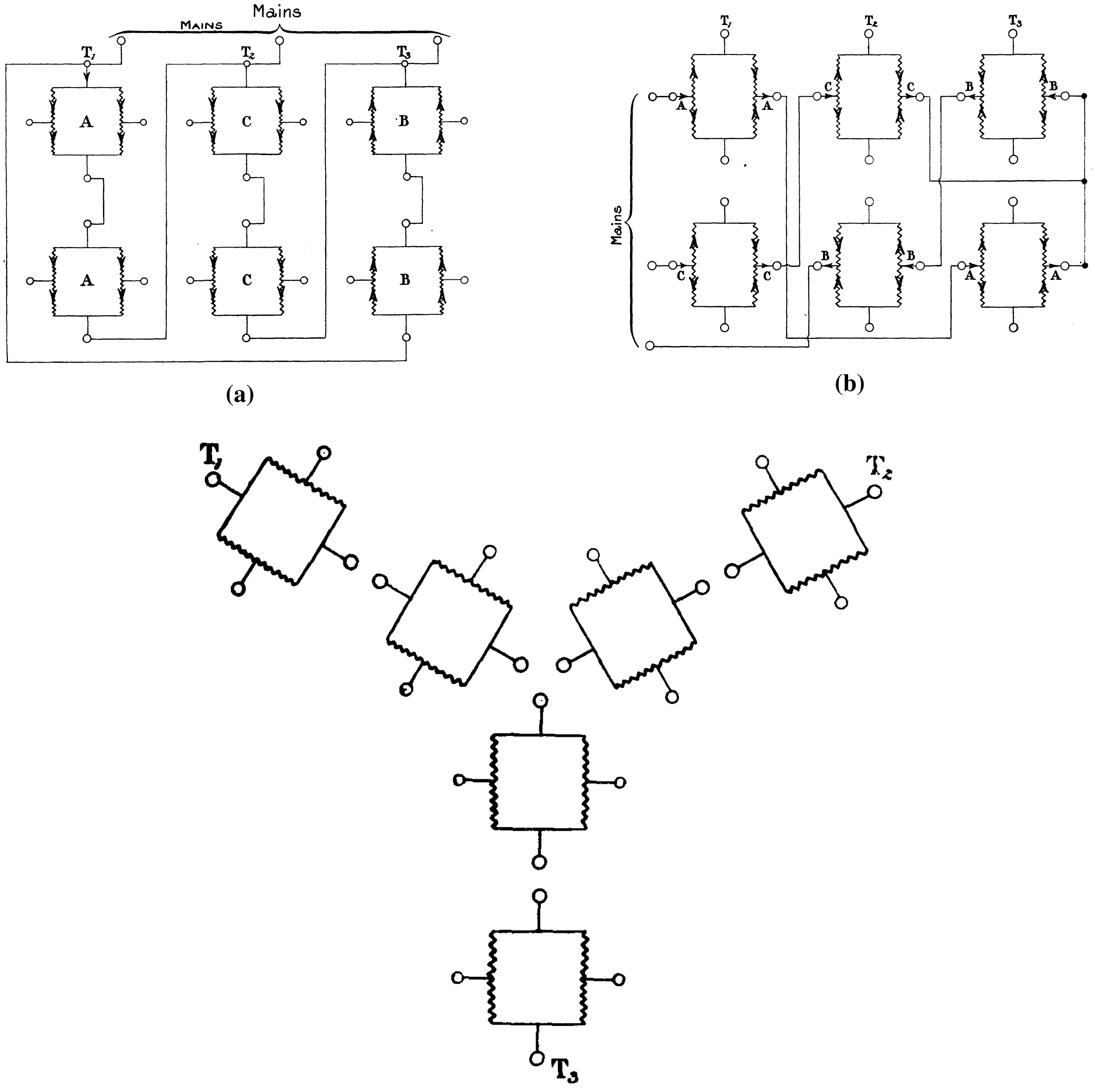

(a)

(b)

(c)

Figure 2.4: *Hunt motor stator connections (a) for 4 poles, (b) for 8 poles, (c) (4 + 8) poles [33].*

the two stator windings in prior cascade motors. Hunt continued to work on the development of this motor, fine tuning the design and making it more practical.

Upon the successful construction and usage of large numbers of these machines, another paper [33], was published in 1914. This paper gave more details as to the design of the Hunt motor, and also notably a brief guide into the selection of the number of poles on the stator. In Figure 2.4, the stator connections to obtain 4 poles, 8 poles, and (4 + 8) poles configurations from a single stator are illustrated. In 1921, F. Creedy published a paper [37], which shed more light on the pole number selections, paving the way for new combinations. Improved rotor and stator winding designs for this type of cascade motor were also discussed in [37]. The works of L.J. Hunt and F. Creedy were foundational for the selection of suitable pole pair combinations for BDFM stator windings.

2.2.4 The Broadway & Burbridge motor

In [38], Broadway and Burbridge sought to design a simpler rotor than the irregularly grouped double layer wound rotors in the Hunt/Creedy motors, while using a similar stator. Two single layer winding rotor types, the graded winding rotor and the multicircuit winding rotor, were investigated. The structures of these rotor types are illustrated in Figure 2.5. Although, the coils of the graded winding are not short circuited together in Figure 2.5(a), the prototype of a graded winding rotor in Figure 2.6(a) has a common endring for the coils. The rotor in Figure 2.6(a) is built for a (6 + 2) poles cascade machine. A multicircuit rotor is also built in [38] for a (18 + 12) poles machine as shown in Figure 2.6(b). These rotors presented in [38], which are now more commonly called the nested loops (NL) and cage+NL rotors, are currently the most widely used rotors in contemporary BDFMs.

2.2.5 Cascade systems to brushless doubly fed operations

The cascade IM systems/cascade motors were conceived at a time before power electronic converters. The early cascade systems were mostly concerned with obtaining efficient motor operations at different (usually low) speeds. The cascade systems were also developed with the view of obtaining robustness and reliability similar to squirrel cage induction motors [35, 38].

The synchronous operation of machines similar to Thompson motors were detailed by B.H.

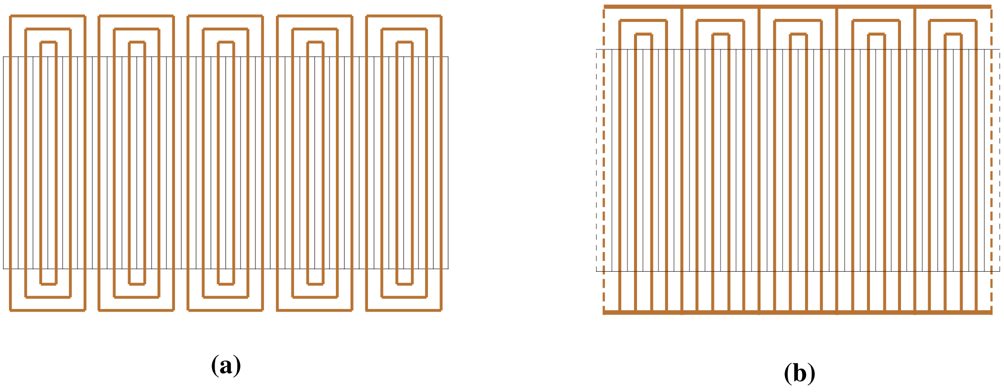

(a)

(b)

Figure 2.5: *Rotor types considered by Broadway & Burbridge (a) Graded windng rotor, (b) Multicircuit winding rotor [38].*

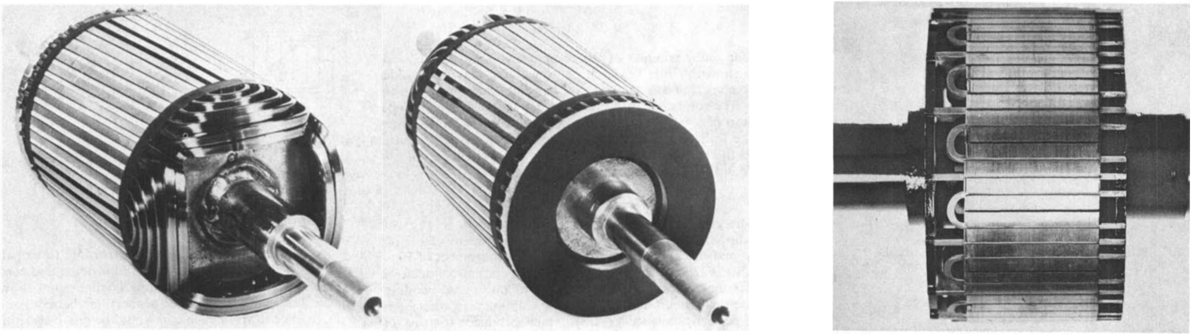

(a) (b)

Figure 2.6: *Broadway & Burbridge rotors (a) Graded winding rotor for (6 + 2) poles machine, (b) Mutlicircuit rotor for (18 + 12) poles machine [38].*

Smith in 1966-7 [39, 40]. The motors used by B.H. Smith were at the time called twin stator induction machines, and the stator windings were both fed with three phase supplies at different frequencies. This was the first of analyses of what were hitherto cascade motors operating similarly to doubly fed induction machines. Slip frequency excitation from a low power frequency converter for harnessing slip power from the machine rotors was discussed.

In 1970 [38], Broadway and Burbridge also discussed the synchronous operations of cascade machines. However, this synchronous operations were limited to the machine synchronous speed, such that AC was applied to one stator winding and DC to the other. Full load performance of the synchronous operations were notably superior to an equivalent multipole IM. Also, there was an increase in power factor compared to asynchronous operations.

The first traceable mention of the term ”brushless doubly fed machine (BDFM)” is in a 1989 paper [41], about a dynamic model of BDFMs. In 1994, Brune et al. tested the possibilities of using the BDFM in a variable speed wind turbine in [42]. The use of a BDFM in a wind turbine was an attempt to obtain the benefits of a DFIG in a more robust structure, which is still the main reason for the recent push in research about BDFMs. A 1.5 kW prototype was built to demonstrate the viability of BDFM based wind turbines. In the following sections, the discussion is shifted to recent developments in the design of BDFMs. Research challenges with the design, and approaches to solving these issues are also discussed.

2.3 Recent BDFM design development

In a push towards ultimately a commercial MW rated BDFM, the authors in [24] up-scaled from their previous 20 kW machine built around 2009 [43], and constructed and tested a 250 kW rated machine. This being the largest BDFM/BDFIG tested to date, showed expected performances and stable control, and thus the possible upwards scalability of the technology.

Although the BDFM is not yet at a commercial scale of implementation, the prospects of usage in wind turbines have recently piqued the interests of several research groups globally. As a result, a number of notable developments have occurred with the BDFM. A lot of recent design developments of BDFMs have focussed on suitable pole pair combinations for the stator windings and optimum rotor design. Optimizing the power density and reduction of harmonics have also received their fair share of attention. Different design approaches of BDFMs have also been presented and all these aspects are discussed in the subsequent sections.

2.3.1 Stator winding development

Up until around 1989, as seen in [41], the L.J. Hunt type of stator windings [33], in which coils of the same winding were interconnected in a way to accommodate two AC supplies (or pole pairs) were used for BDFMs. However in [44], Rochelle suggested that the L.J. hunt type of stator winding, which efficiently utilized stator conductors, was better suited for applications in which only one set of terminals are connected to a power source at a time.

For synchronous BDFM operation, with two AC supplies connected to the terminals, there are unbalances in the Hunt type of stator, which lead to internal circulating currents. Therefore Rochelle recommended reverting to isolated stator windings like in the Lydall motor, which could avoid the circulating current problems, while affording greater simplicity and flexibility.

Consequently, contemporary BDFM stators have two isolated windings, the power winding (PW) and the control winding (CW). As already suggested in [35], the winding in this configuration which is farthest from the airgap has increased leakage. Placing the PW at the bottom layer would have significant effects on the converter ratings, as higher leakage would increase the difficulty in controlling the grid side power factor as noted in [45]. Thus, the PW with p_1 pole pairs typically occupies the bottom layer (closest to the airgap) of the stator slots, while the CW with p_2 pole pairs occupies the top layer. This type of stator for a p_1/p_2 = 2/3 BDFM, is illustrated in Figure 2.7.

2.3.1.1 Relative winding pole size

Typically, p_1 is lower than p_2 for a number of reasons. A significant reason for using the lower pole as p_1 is the higher magnetizing requirements with increasing poles [46–48]. Thus higher poles for p_1 can increase the power ratings of the converters used. Furthermore, the lower pole number for p_1 affords better winding distribution, as the PW and CW occupy the same number of slots, and this helps with harmonic mitigation.

The BDFM torque breaks down at the synchronous speed of a p_1 machine, thus favouring a

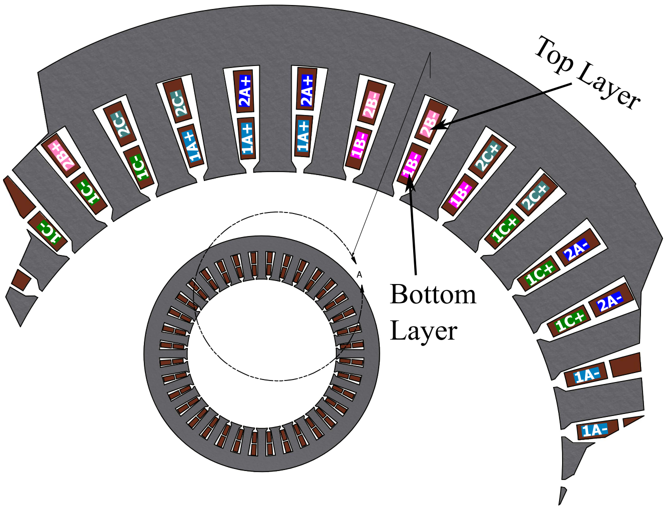

Figure 2.7: *Stator winding arrangement of a 2/3 BDFM.*

lower p_1 for a wider operating speed range [47]. However, this hardly applies to BDFMs with regards to being alternatives to DFIGs in wind turbines. To use fractionally rated converters within a third of the BDFM power ratings, the BDFM speed range will typically be lower than the synchronous speed of the higher pole [49].

The rotor field frequency (ω_{r_f}) is calculated from the formula in [13, 50],

$$\omega_{r_f} = \omega_1 - p_1\omega_r = -\omega_2 + p_2\omega_r, \tag{2.3.1}$$

where, ω_1 & ω_2 are the electrical angular speeds of the PW and CW respectively, while ω_r is mechanical angular speed of the rotor. It can be observed that ω_{r_f} is higher with if p_1 is lower than p_2. This has implications as core losses [51, 52], and rotor impedances, considering that skin effect is lower at lower frequencies. The disparity between p_1 and p_2 should not be too high to reduce copper losses due to skin effect [51].

2.3.1.2 Unbalanced magnetic pull and magnetic coupling

In [53], it was established that when a x-pole pair field is combined with a $(x+y)$-pole pair field, a force imbalance occurs when y = 1. This imbalance, now commonly called an unbalanced magnetic pull (UMP), was then illustrated (Figure 2.8) with a 2/3 pole pair combination. It can be observed from the force diagram in Figure 2.8, that a strong zone is directly opposite to a weak force zone giving rise to the imbalance. If $y > 1$, then there will be equal y strong and weak zones [53], and UMPs can be avoided.

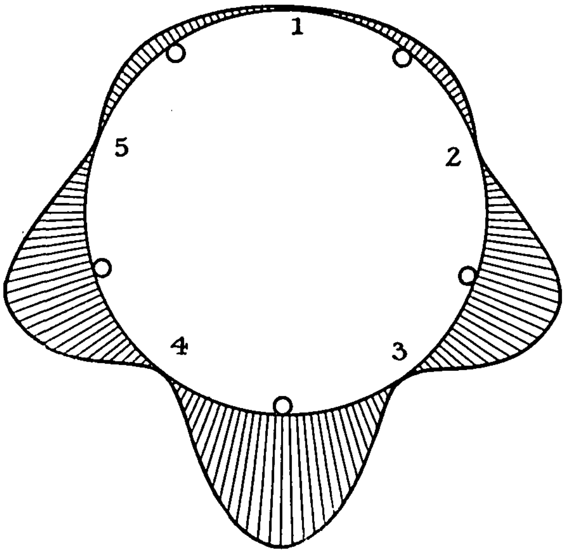

Figure 2.8: *Force diagram of a 2/3 pole pair combination [53].*

The harmonics generated by the PW and CW are given respectively as

$$\begin{aligned} h_{pw} &= p_1(2t-1), \quad t \in \mathbb{N}, \\ h_{cw} &= p_2(2t-1), \quad t \in \mathbb{N}. \end{aligned} \tag{2.3.2}$$

If the windings have no common harmonic, they do not couple inductively. A bit more nuance to the combinations to ensure non coupling is given in [13]. However, the rules given in [13] only guarantee non coupling when series windings are used. The use of parallel coil group connections can enable direct coupling of the PW and CW, which produces circulating currents. Practical connections of coil groups in parallel while avoiding direct coupling are discussed in [54], and these parallel paths are shown to help mitigate UMPs.

2.3.1.3 Commonly used pole combinations

Pole pair combinations which do not produce UMP were tested using 2D FE BDFM models in [55], to highlight suitable combinations. Although the $p_1/p_2 = 2/4$ pole pair combination is used for a 250 kW BDFM prototype in [56], the results in [55] suggest that the $p_1/p_2 = 4/6$ combination is more suitable in terms of power, efficiency and torque ripple. However, optimization results in [57] indicate that the $p_1/p_2 = 2/4$ combination performs better than the $p_1/p_2 = 4/6$ combination for a BDFM in a D180 frame size. Analytical estimations in [49] also point to better performance from the $p_1/p_2 = 2/4$ combination compared to the $p_1/p_2 = 4/6$ in terms of power and efficiency.

Table 2.1: *Relative performance of popular BDFM pole pair combinations*

Parameters	**Pole pair combinations (p_1/p_2)**		
	2/3	2/4	4/6
Power density [49, 57, 60]	High	Medium	Low
Efficiency [49, 57, 60]	High	Medium	Low
Torque ripple [57]	Low	High	Low
Harmonic distortion [58, 59]	Low	High	Low
UMP [54, 55]	Present	-	-

In spite of these, the $p_1/p_2 = 2/3$ is the preferred combination for the D180 frame BDFM in [57], as it produces the best performance in terms of efficiency and generated torque. The $p_1/p_2 = 2/3$ combination in [57] also has considerably lower torque ripple and time harmonic distortions compared to the $p_1/p_2 = 2/4$ combination. Concerns of UMP with the p_1/p_2 = $2/3$ combinations were considered minor in [57], due to the small size of the machine. In [58], the $p_1/p_2 = 4/6$ is the preferred combination for a 3.2 MW BDFM due to the less coupling of higher space harmonics compared to the $p_1/p_2 = 2/4$ combination, and absence of UMP compared to the $p_1/p_2 = 2/3$ combination. The lower harmonic content in the $4/6$ combination relative to the $2/4$ combination is also alluded to in [59], however the PW has the higher pole number. A summary of the relative performances of the $2/3$, $2/4$ and $4/6$ pole pair combinations as described in literature is given in Table 2.1.

2.3.2 Rotor winding development

The nested loop (NL) and cage+NL rotors, whose origins are traced to [38], are currently deemed the most suitable for BDFMs [9, 12, 13]. The NL rotor winding arrangement and prototype example are shown in Figures. 2.9(a) & 2.9(b) respectively, while an example of the cage+NL rotor is shown in Figure 2.9(c). The winding arrangement in Figure 2.9(a) differs from that in Figure 2.5(a) by the presence of a common end ring, with the rotor illustrated in Figure 2.5(a) now sometimes called an isolated loop (IL) rotor [13]. These (NL, IL, & cage+NL) rotor types have robust builds with better torque performance and lower losses, compared to BDFM wound rotors [12].

A rotor similar to the NL rotor, but with double layers of bars, is highlighted in [13]. It is suggested that this double layer bar rotor has a larger torque envelope, and higher efficiency due to less excess harmonic reactance in comparison with the NL rotor. However, the increased complexity has manufacturing and control implications. The double layer bar rotor winding arrangement is illustrated in Figure 2.10(a), while a prototype is shown in Figure 2.10(b).

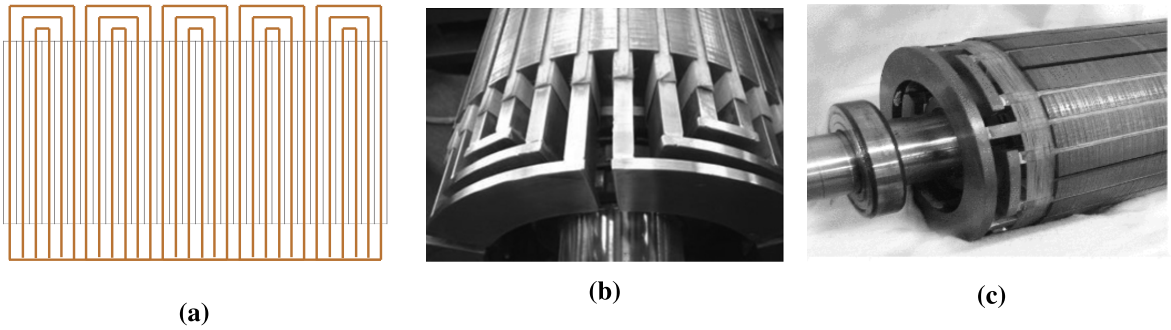

Figure 2.9: *(a) NL rotor winding arrangement, (b) NL rotor prototype [9], (c) cage+NL rotor prototype[19].*

Whilst considering the high harmonic reactance and potential considerable skin effect in large BDFMs using NL rotors, series wound (SW) rotors are compared with NL rotors in [9]. The winding arrangement of the SW rotor is illustrated in Figure 2.11(a), with a prototype shown in Figure 2.11(b). Although the SW rotor has lower harmonic content and no skin effect issues, it has higher impedance and develops lower torque. Despite this, the performance of the SW rotor is deemed acceptable. It is also indicated that with similar slot fill factors, the SW and NL rotors will have similar torque performance due to identical referred rotor resistance. Also, in [61], details of the design of a 60 kW BDFM with a special ”double-sine” rotor are given. This rotor was designed as a potential BDFM rotor with greatly reduced harmonic content.

Although, the cage+NL rotor has similar advantages with the NL rotor, the NL configuration is more commonly used [12]. In [20, 21], the NL and cage+NL rotors are compared based on their rotor equivalent circuit parameters, and it is suggested that the cage+NL rotors provide better performance due to their lower impedances. This advantage of cage+NL rotors is shown in [19] to be more evident when the disparity between p_1 and p_2 is greater. In cases where the p_1 value is close to p_2, the NL rotor may perform better due to lower leakage inductance.

Initial guidelines for loop design of the NL and cage+NL rotors are given in [62]. It is suggested that loops with spans closer to the pitch of the higher pole number in the BDFM are more efficient, and more effective in torque production. It is also suggested in [62] that loops with small spans have minor contributions to torque production, similar to suggestions in [10, 20, 63]. Observations in [10, 20, 62] indicate that the rotor loops should not necessarily be evenly spaced, and the width of the outer loops should be maximized. An increase in rotor loops per nest help to mitigate space harmonics in BDFMs [10, 47], and helps with better current distribution in BDFM rotors [47].

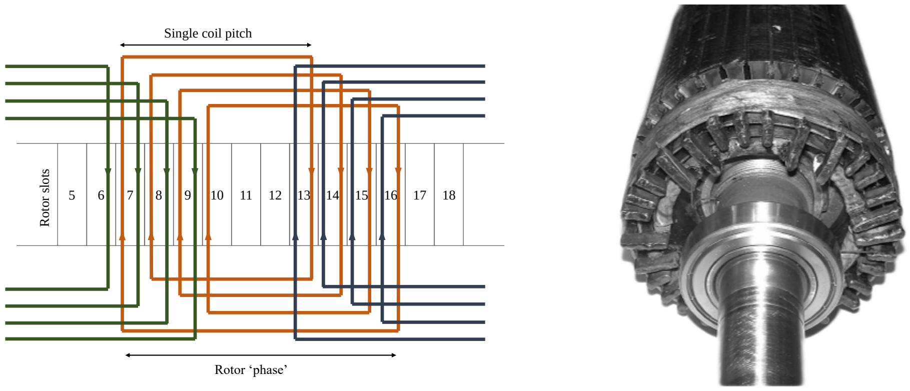

(a) **(b)**

Figure 2.10: *Double layer bar rotor (a) Winding arrangement for a 4/8 pole pair combination, (b) Prototype [13].*

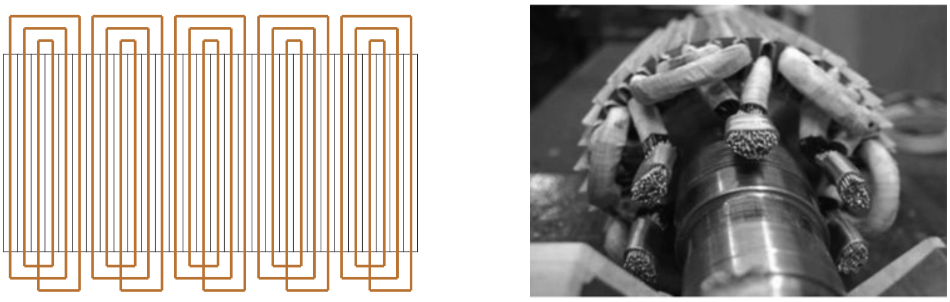

(a) **(b)**

Figure 2.11: *SW rotor (a) Winding arrangement (b) Prototype [9].*

2.3.3 BDFM sizing and power ratings

By analyzing the stator magnetic fields in BDFMs using a per phase equivalent circuit, a composite magnetic loading based on the stator fields is derived in [22]. An expression for the BDFM power rating as a function of the electric loading, magnetic loading, and some geometric parameters related to the BDFM size, is also given in [22]. The magnetic loading derivation in [22] was further modified in [47], as the loading derived in [22] was deemed too conservative leading to over-sizing. Other aspects of the BDFM geometric sizing such as the slot teeth width and core height/depth are also given in [47].

The BDFM power ratings expression in [22] is used to predict about a quarter reduction of the power rating in BDFMs compared to conventional DFIGs of the same size. The influence of pole pair combinations on this disparity in power between BDFMs and DFIGs is investigated in [49]. It is suggested that combinations with lower (p_1/p_2) pole ratios have slight reduction in this disparity. These observations are somewhat echoed in [23], however, the analysed MW rated BDFMs have more than a quarter increase in mass when compared with DFIGs of similar power and operating speed. BDFMs also suffer a reduction in efficiency compared to DFIGs due to the added rotor winding losses [12].

The impact of pole combination choice on the BDFM core depth is characterized in [49]. For the pole pair combinations investigated in [49], it is observed that the BDFM core depths are at least two times bigger than DFIG core depths. However, it is also observed that as p_1 gets closer to p_2, the core depth ratio of a BDFM to a DFIG of similar speed gets smaller. Also, it is demonstrated in [64], how sections of an NL rotor core which do not contribute to the rotor magnetic circuit can be removed for weight reduction.

The effects of rotor leakage inductances on inverter ratings are illustrated in [45]. An increase in the rotor leakage inductance reduces the inverter ratings required for crowbar-less low voltage ride through (LVRT) requirements, but reduces the power factor management abilities. A trade-off between LVRT and power factor management requirements is therefore advocated in the choice and design of BDFM rotors. In [65], the effects of magnetic wedges on magnetizing currents and stator/rotor inductances are investigated. It is observed that the use of magnetic wedges can lead to increases in the stator and rotor leakage inductances with reductions in the magnetization currents. With these effects having significant implications on the machine performance, methods of optimally designing magnetic wedges for optimal inverter power ratings are discussed in [56].

2.3.4 Vibrations and Harmonics mitigation

In [66], it is affirmed that the combination of two magnetic fields of different poles renders BDFMs susceptible to extra vibrations not present in single field induction machines. It is further revealed that the bending forces on the stator back iron, which are significantly dependent on the pole pair combinations, contribute greatly to these vibrations. Apparently, combinations with pole numbers which are close tend to produce higher vibrations. A method to mitigate these vibrations is also given, such that the machines are ”stiffened” by increasing the stator core depth. This solution would have to be applied with caution, as BDFMs already have longer core depths compared to DFIGs [49].

In [67], it is stated that the most significant source of torque ripple in BDFMs is the winding distribution space harmonics; the excessive space harmonics present in the nested loop rotor structure being a major culprit. In [10, 20, 59], it is suggested that increasing the rotor loop spans helps in reducing harmonic content in BDFMs. Also, increase in rotor loops per nest help to mitigate space harmonics in BDFMs [10, 47]. Using a coupled circuit model, the effect on torque ripple of the NL and cage+NL rotor loop spans relative to the PW and CW pole pitches, is illustrated. It is then shown how the coupled circuit model can be used to find suitable rotor designs for specific BDFM applications.

Slot types have effects on torque ripple [67]. Also, a double layer CW is expected to reduce torque ripple according to [68]. It is shown analytically in [69], that rotor skews help to reduce torque ripple. The effects of rotor skewing are further investigated in [70], and it is determined that skewing has little effects on losses, however, there is a slight reduction in the average torque.

As noted in section 2.3.1, suitable pole pair combinations are investigated for torque ripple and harmonic content in [55, 57, 58]. Pole pair combinations that are multiples of the 2/3 combination have low harmonic content [12, 55, 57, 58], however, the 2/3 combination itself suffers from UMP.

2.3.5 BDFM design and optimization procedures

A proposed design procedure for a 6 MW BDFM is presented in [25], as illustrated in Fig. 2.12. The power rating is selected because the largest DFIG generators used in wind turbines are rated similarly. In the design process, the BDFM equivalent circuit in [71] is used to obtain an initial design from the determined machine specifications. A coupled circuit BDFM model is then employed to evaluate the designed nested loop rotor. Finite element analysis (FEA) of the design is conducted to investigate the peak flux densities in the different iron parts, and obtain a close estimate of the magnetizing current. Thermal evaluation of the BDFM design is also recommended alongside discussions with machine manufacturers to aid practicality. System performances such as dynamics, control stability and LVRT capabilities are then considered in a fine-tuning of the design. This design procedure is reportedly employed for the 250 kW built and tested in [24].

Available BDFM electric equivalent circuit (EEC) models are limited in evaluating saturation, and FEA models are computationally costly. In light of these, a design approach for BDFMs using an EEC and a magnetic equivalent circuit (MEC) model is presented in [72]. The MEC developed in [73], is used to determine the flux distribution by the PW and CW, while the EEC model uses the MEC results to determine the machine performance.

It is noted in [26] that investigations on the design of BDFMs are limited in available literature. To that effect, a comprehensive BDFM design procedure considering the electromagnetic and thermal aspects of the BDFM, is presented in [26], with details of some of the models used given in [74]. A flowchart of the design procedure is given in Fig. 2.13. An EEC model is used to evaluate stator and rotor currents, while a static MEC as presented [74], is used to analyse the flux density distributions and core loss caused by these currents.

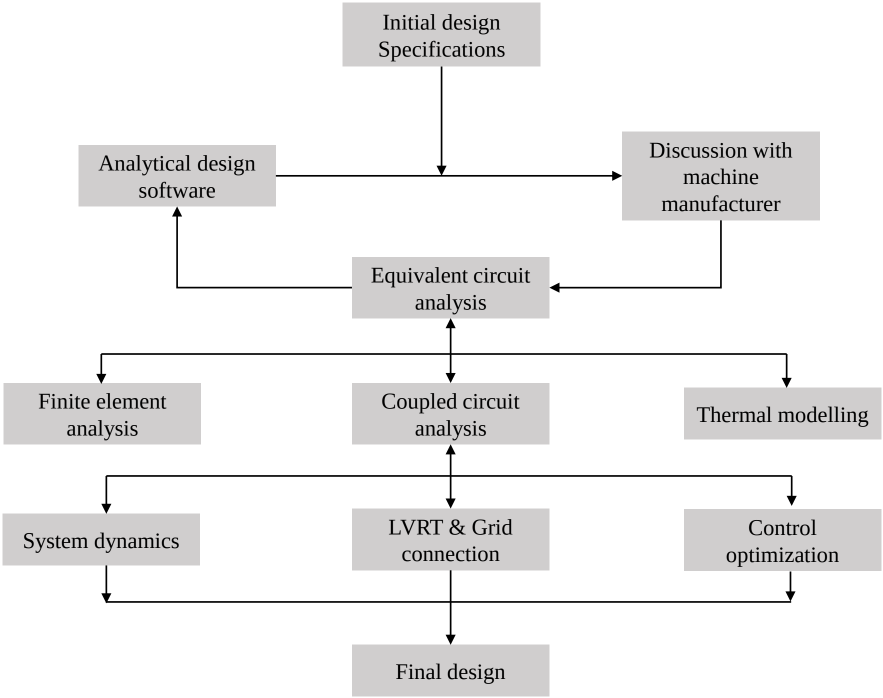

Figure 2.12: *Proposed design procedure for a 6 MW BDFM [25].*

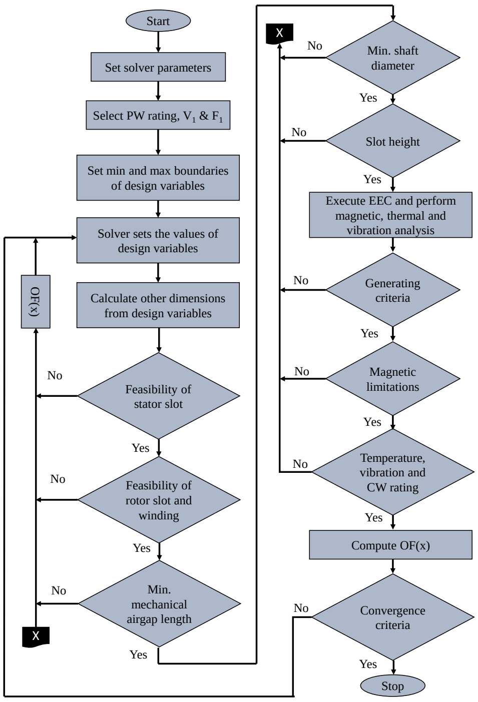

Figure 2.13: *Design procedure in [26].*

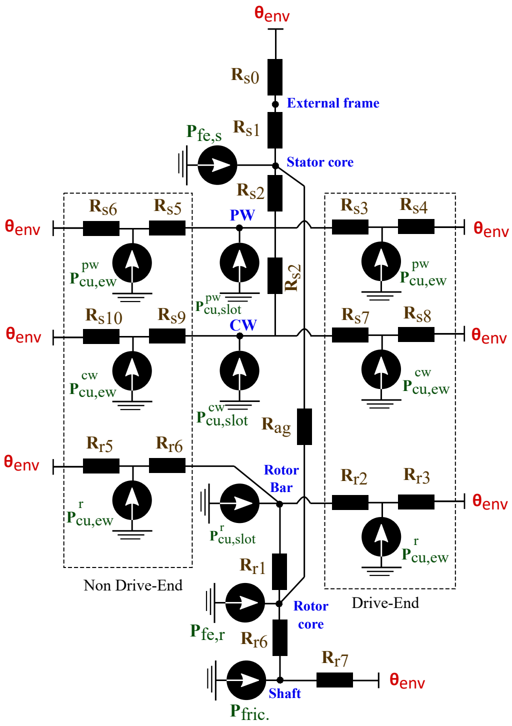

Figure 2.14: *Radial equivalent thermal network of a BDFM [26].*

Table 2.2: *Resistance descriptions in thermal model [26]*

Component	Description
R_{s0}	Thermal resistance between external frame and environment with thermal resistance of external frame
R_{s1}	Thermal resistance of stator core
R_{s2}	Thermal resistance of coil insulator
R_{s3}/R_{s5} R_{s7}/R_{s9}	Thermal resistance of PW & CW end-winding to middle of slot at drive end/non drive end sections
R_{s4}/R_{s6} R_{s8}/R_{s10}	Thermal resistance between PW & CW end-winding and environment at drive end/non drive end sections
R_{ag}	Thermal resistance between rotor and stator
R_{r1}	Thermal resistance of rotor slot insulator
R_{r2}/R_{r4}	Thermal resistance of rotor end-winding to middle of slot at drive end/non drive end sections
R_{r3}/R_{r5}	Thermal resistance between rotor end-winding and environment at drive end/non drive end sections
R_{r6}	Thermal resistance of rotor core
R_{r7}	Thermal resistance between shaft and environment
$P_{fe,(s/r)}$, P_{fric}	Stator/rotor iron, Frictional losses
$P_{cu,ew}$, $P_{cu,slot}$	End-winding, slot copper losses

Temperature analysis is conducted in the design process in [26], using a lumped parameter thermal model illustrated in Fig. 2.14. The machine sections are designated as resistances, with the losses identified as heat sources. The description of the thermal model components are given in Table 2.2. A simple vibration analysis is also used to estimate vibrations in designs, and the optimization results are verified using 2-D FEA.

An optimization process using the imperialist competitive algorithm is used to maximize the power to weight ratio, efficiency, power factor, while minimizing the voltage regulation and rotor differential leakage inductance in [26]. Feasibility of different aspects of the BDFM design are monitored such as the stator and rotor slots, the airgap length, shaft diameter etc. However, it is the CW power factor that was being maximized, also the CW is seemingly placed closest to the airgap.

An iterative method (Tabu search) is used to optimize the stator of a 180 frame size BDFM based on its per phase equivalent circuit model in [75]. The optimization was used to demonstrate how appropriate division of the stator slot area between the PW and CW can enable BDFM operation at the magnetic and electric loading limits. This maximizes the power output, as was demonstrated by the 21 % increase in power from the original design. This method of optimization is also applied to a D160 frame BDFM in [76], to optimize the electric and magnetic loadings. The maximum motoring torque with a lower limit on the PW power factor of 0.75 is used for machine evaluation in the optimization process.

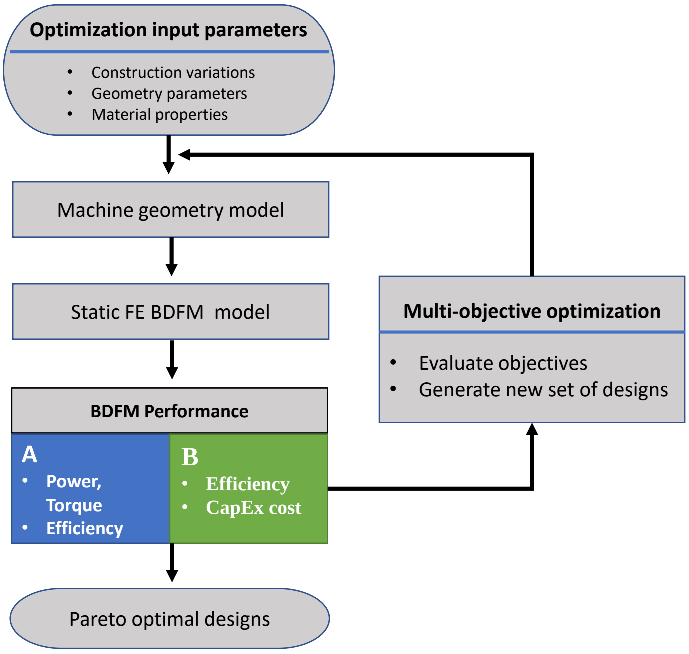

Figure 2.15: *Optimization processes in [58, 60].*

A magnetostatic FE BDFM model is presented in [60, 77] to enable computationally efficient and accurate optimization processes. The non-dominated sorting genetic algorithm II (NSGA-II) is used in [60] alongside the magnetostatic FE model to optimize the torque and efficiency of a BDFM designed for a D180 frame size. Geometric variables such as the stator inner radius and the ratios of slot/yoke height are used in the optimization process. The NSGA-II is also used in an optimization process in [58] to optimize the material cost and efficiency of a 3.2 MW BDFM. Similar geometric variables and magnetostatic FE models like in [60], are used in the optimization process in [58].

Both optimization processes in [60] and [58] are illustrated in Fig. 2.15; A & B representing the optimized BDFM performances in [60] and [58] respectively. Different pole pair combinations (p_1/p_2 = 1/3, 2/3, 2/4 & 4/6) are tested in the optimization process in [60], with the 2/3 combination having the superior performance. However the 4/6 pole pair combination is used for the 3.2 MW BDFM in [58], because of the effects of the presence of UMP using the 2/3 combination. It is worth noting that the machines in [60] and [58] are optimized at the maximum torque operation points.

2.4 Conclusion and future research

This review on the design of BDFMs can be divided into two parts; the evolution of cascade motors to BDFMs, and the recent developments in BDFM design. BDFMs have a rich history in terms of development, which has been laid out. The evolution was detailed in a way to provide the reader with perspective on BDFM development by highlighting pioneering designs and prototypes. Contemporary developments in the design of BDFMs are also described. These recent developments have revolved around the stator winding pole pair combinations, rotor topology and performance optimizations.

Recurring themes in recent design related articles on BDFMs include the selection of suitable pole pair combinations for the stator windings for desired performances, vibrations and harmonic mitigation, optimization of machine power density and efficiency. The stator structure design seems to be settled on the electrically isolated windings occupying different layers in the stator slots, with the PW typically closest to the airgap and the CW closer to the core. However, there is no clear candidate for the pole pair combinations of these windings. Researchers seem split between the 2/4 and 4/6 combinations for different reason which are detailed. Thus further insight on suitable pole pair combinations is crucial. The use of fractionally distributed windings for harmonics mitigation also needs to be further investigated.

On the other hand, a lot of research is still being conducted on the type and structure of BDFM rotors. Two rotor types, the NL and cage+NL rotors are the leading choices of rotor types. The number of loops per nest for either rotor type is not fixed, and varies for reasons like harmonics, vibrations and torque performance. There is still a potential of significant skin effect in large BDFMs using NL or cage+NL rotors, which needs more in-depth research.

BDFM sizing is detailed in available literature. However, the equations used for parameters like the airgap flux density or core depths are not definitive. To this effect, investigations across different power ratings may be required to identify the saturation tolerances of BDFMs. This will also help provide a more accurate basis for power density comparisons between BDFMs and DFIGs. Different models have been used for design purposes, giving researchers interested in BDFM designs a variety of options. However, many require individual implementation as none of these models are available in software form for public use, or in commercial software packages. This generally makes the design of BDFMs a longer process than conventional machines. Different design procedures have also been presented, and these provide useful insight into the design of BDFMs. A design process unifying the machine and converter designs would provide a comprehensive understanding of the BDFM in wind turbine system.

Chapter 3

Coupled circuit analysis of the brushless doubly fed machine using the winding function theory

---

The emergence of brushless doubly fed induction machines (BDFMs) as an alternative to doubly fed induction generators (DFIGs) in wind energy conversion systems is fascinating. However, BDFMs have a complex machine structure, and their operations are relatively complicated. In this chapter, the winding function theory (WFT) is used in the development of a coupled circuit (CC) model for BDFMs with nested loop (NL) and cage+NL rotors, in order to give a robust representation of the electrical operations of BDFMs.

The electrical circuit analysis of BDFMs having NL and cage+NL rotors is comprehensively detailed, with the stator and rotor inductances calculated using their winding functions. The interactions of BDFM rotor loops with stator windings are demonstrated in terms of mutual inductances. CC models of different BDFMs are simulated for synchronous doubly fed BDFM operations with emphasis on generating regions. Also, fresh insight into the torque production in BDFMs is provided, with the rotor loops and stator windings contributions to torque magnitude and ripple examined. This chapter is based on the journal publication by Olubamiwa, Gule & Kamper (2020) [63].

3.1 Introduction

The BDFM structure and operations are more complex than conventional DFIGs, and they require extensive analysis. Different BDFM analytical models have been developed to aid understanding of the operations of BDFMs, and for design related objectives [12]. The coupled circuit (CC) modelling has been commonly used in developing non salient pole electric machine models, and is a relatively easy to understand approach to machine modelling. From the CC viewpoint, a machine is modelled as an electric circuit with variable inductances dependent on the rotor position [78]. The flux linkages and magnetic field co-energy in a CC are based on currents and inductances. Furthermore, the CC approach has been utilized to develop BDFM models in [41, 79], [50], [80], and [81] with reasonably accurate results, and have provided useful insight about BDFM operations.

The CC BDFM model in [41] is developed for BDFMs with cage+NL rotors in pumped storage hydro generation and regenerative traction applications. Steady state and dynamic operations are investigated for the machine in the simple induction mode and during no load acceleration. The simulation results of the CC model introduced in [41] are compared with experimental results in [79]. The response of the motor in the synchronous doubly fed mode to increasing load torque till loss of synchronism is also illustrated in terms of the PW currents and the motor speed. It should be noted that the stator of the BDFM in [41, 79] consists of 9 similarly wound coil groups arranged in 3 Y-connected sets supplied by 2 independent 3-phase supplies. Also, only the CC model results are illustrated for the synchronous motoring mode.

The CC BDFM model in [50] builds on the model described in [41, 79]. The CC is transformed to the dq axis in the synchronous reference frame. Only the NL rotor is considered in [50], and a model reduction procedure is performed to represent the rotor as a single dq pair. The model in [50] is ultimately developed for simplification of BDFM controllers.

The CC models in [80, 81] are developed for dual stator winding induction machines. Although the dual stator winding induction machine is differentiated from the contemporary BDFM in [80, 81], the structures and operations of both machine types have similarities. The models in [80, 81] are predominantly focussed on wide speed range motoring operations. Also, the machine rotor in [80, 81] is the standard squirrel cage rotor, which is not ideal for BDFMs. The machine inductances are calculated using the winding function theory (WFT) in [81].

The WFT, described in [82], uses details about the machine geometry and the physical arrangement of the windings to calculate the MMF per unit current in the windings. The MMFs are used to calculate flux linkages in the windings, from which the self and mutual inductances are calculated. The WFT is used in [83] in the modelling of non sinusoidally wound induction machines for steady state and dynamic simulations, and in [84], it is used in the dynamic analysis of induction machines with stator, rotor bars and end ring faults. In [85], the WFT is also used in the evaluation of rotor bar and end ring currents of multiphase induction machines.

In [10], different loops with varying loop spans are combined to configure a number of NL rotor constructions. These rotors are simulated using finite element analysis (FEA) to investigate the contributions of NL rotor loops to torque production and total harmonic distortion. It was observed that the outer loops contributed more to the torque, and the determined the overall harmonic distortion. Suggestions for further investigation of the contributions of the loops to torque ripple were also raised.

In this chapter, the WFT is used to calculate inductances in the development of a CC model for BDFMs with NL and cage+NL rotors. BDFMs with NL and cage+NL rotors designed for the 160L induction machine frames are simulated using the developed CC model. Instead of solely examining motoring operations like in [41], [79], [80] and [81], synchronous doubly fed generating conditions are investigated extensively. The CC model simulation results are compared with FEA simulation results of the same machines.

Different simulation results are used to illustrate preliminary design applications of the CC model, and to provide insight on the operations of BDFMs. The effect of the rotor loop spans on the BDFM stator to rotor mutual inductances are discussed, and used to illustrate the torque contributions of the BDFM rotors loops. The effect of rotor loops on BDFM torque ripple is also investigated, and potential ways of mitigating the torque ripple by proper selection of rotor type and/or number of rotor loops are discussed and illustrated. The CC model is also used to provide a quick and robust method for determining BDFM rotor currents at different operating conditions.

3.2 Coupled circuit model

The following assumptions are made in the modelling of BDFMs

- The effects of saturation are neglected
- The air gap of the BDFM is uniform, and there is no rotor eccentricity
- $p_1 \neq p_2$, therefore, there is no direct coupling between the PW and the CW
- Voltage excitations are used at the PW, with current excitations at the CW
- The PW (slot, zigzag and end connection) leakages are calculated according to formulas in [16]. Rotor slot and differential leakages are also calculated from formulas in [16]. The rotor end connection segment leakages are calculated in similar manner with squirrel cage rotors, and segments occupied by loops are aggregated to determine the loop end connection leakage.

3.2.1 Stator voltage & current equations

The 3 phase PW voltage vector ($\boldsymbol{V_p}$) can be represented as

$$\boldsymbol{V}_p = [V_{p_1}\ V_{p_2}\ V_{p_3}]^t. \tag{3.2.1}$$

Using general winding voltage equations as used in [81] and [83], $\boldsymbol{V_p}$ can be calculated as follows

$$\boldsymbol{V}_p = \boldsymbol{R_p}\boldsymbol{I}_p + \frac{d\boldsymbol{\lambda}_p}{dt}, \tag{3.2.2}$$

where, $\boldsymbol{R_p}$ is the PW resistance matrix, $\boldsymbol{I_p}$ is the PW current vector, and $\boldsymbol{\lambda_p}$ is the PW flux linkage matrix. $\boldsymbol{R_p}$ is given as

$$\boldsymbol{R_p} = r_p\boldsymbol{I}, \tag{3.2.3}$$

where, r_p is the PW phase winding resistance, and $\boldsymbol{I}$ is a 3 x 3 identity matrix. The PW current vector ($\boldsymbol{I_p}$) is represented as

$$\boldsymbol{I_p} = [I_{p_1}\ I_{p_2}\ I_{p_3}]^t. \tag{3.2.4}$$

$\boldsymbol{\lambda_p}$ is then calculated as

$$\boldsymbol{\lambda_p} = \boldsymbol{L_p}\boldsymbol{I_p} + \boldsymbol{L}_{pr}\boldsymbol{I_r}, \tag{3.2.5}$$

where, $\boldsymbol{L_p}$ is the PW inductance matrix, $\boldsymbol{L}_{pr}$ is the instantaneous mutual inductance matrix between the PW and the rotor windings (loops), and $\boldsymbol{I_r}$ (illustrated in Figures 3.1 & 3.2) is the rotor loops current vector.

$\boldsymbol{L_p}$ can be written as

$$\boldsymbol{L_p} = \begin{bmatrix} L_{p_{11}} & L_{p_{12}} & L_{p_{13}} \\ L_{p_{21}} & L_{p_{22}} & L_{p_{23}} \\ L_{p_{31}} & L_{p_{32}} & L_{p_{33}} \end{bmatrix}. \tag{3.2.6}$$

With, $\boldsymbol{V}_p$ being the grid voltage, the PW flux linkages, $\boldsymbol{\lambda_p}$, can also be calculated from (3.2.2) as

$$\boldsymbol{\lambda}_p = \int (\boldsymbol{V_p} - \boldsymbol{R_p}\boldsymbol{I_p})dt. \tag{3.2.7}$$

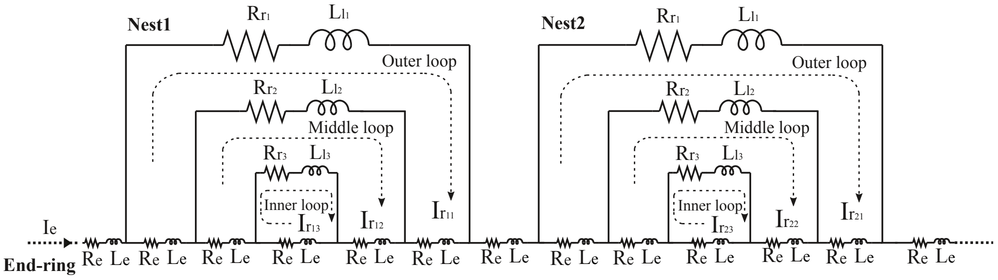

Figure 3.1: *Circuit model of NL rotor.*

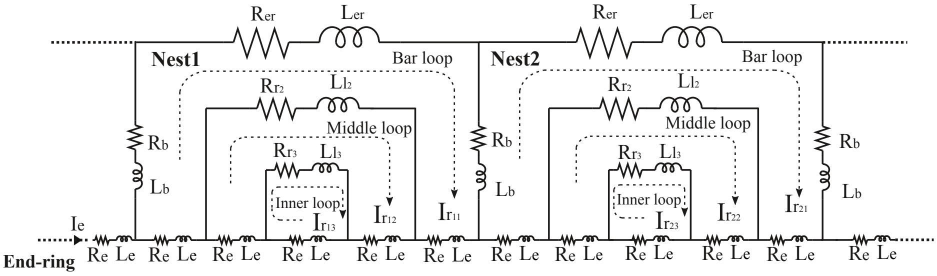

Figure 3.2: *Circuit model of Cage+NL rotor.*

The PW current ($\boldsymbol{I_p}$) is then calculated from (3.2.5) as

$$\boldsymbol{I_p} = \boldsymbol{L_p}^{-1}\boldsymbol{\lambda_p} - \boldsymbol{L_p}^{-1}\boldsymbol{L}_{pr}\boldsymbol{I_r}. \tag{3.2.8}$$

3.2.2 Rotor voltage & current equations

The circuit models of the NL and cage+NL rotors are illustrated Figures 3.1 & 3.2 respectively. The rotor loops voltage vector ($\boldsymbol{V_r}$) obtained by mesh analysis of the loops is given by

$$\boldsymbol{V_r} = \boldsymbol{R_r}\boldsymbol{I_r} + \frac{d\boldsymbol{\lambda_r}}{dt}, \tag{3.2.9}$$

where, $\boldsymbol{R_r}$ is the rotor loops resistance matrix illustrated in (3.2.10) & (3.2.11) for the NL and cage+NL rotors respectively.

$$\boldsymbol{R}_r = \begin{bmatrix} R_{r_1}+5R_e & 3R_e & R_e & 0 & 0 & 0 & \cdots & -5R_e \\ 3R_e & R_{r_2}+3R_e & R_e & 0 & 0 & 0 & \cdots & -3R_e \\ R_e & R_e & R_{r_3}+R_e & 0 & 0 & 0 & \cdots & -R_e \\ 0 & 0 & 0 & R_{r_1}+5R_e & 3R_e & R_e & \cdots & -5R_e \\ 0 & 0 & 0 & 3R_e & R_{r_2}+3_e & R_e & \cdots & -3R_e \\ 0 & 0 & 0 & R_e & R_e & R_{r_3}+R_e & \cdots & -R_e \\ \vdots & \vdots & \vdots & \vdots & \vdots & \vdots & \ddots & \vdots \\ -5R_e & -3R_e & -R_e & -5R_e & -3R_e & -R_e & \cdots & N_rR_e \end{bmatrix} \tag{3.2.10}$$

$$\boldsymbol{R}_r = \begin{bmatrix} 2R_b+5R_e+R_{er} & 3R_e & R_e & -R_b & 0 & 0 & \cdots & -5R_e \\ 3R_e & R_{r_2}+3R_e & R_e & 0 & 0 & 0 & \cdots & -3R_e \\ R_e & R_e & R_{r_3}+R_e & 0 & 0 & 0 & \cdots & -R_e \\ -R_b & 0 & 0 & 2R_b+5R_e+R_{er} & 3R_e & R_e & \cdots & -5R_e \\ 0 & 0 & 0 & 3R_e & R_{r_2}+3R_e & R_e & \cdots & -3R_e \\ 0 & 0 & 0 & R_e & R_e & R_{r_3}+R_e & \cdots & -R_e \\ . & . & . & -R_b & . & . & \cdots & . \\ \vdots & \vdots & \vdots & \vdots & \vdots & \vdots & \ddots & \vdots \\ -5R_e & -3R_e & -R_e & -5R_e & -3R_e & -R_e & \cdots & N_rR_e \end{bmatrix} \tag{3.2.11}$$

From (3.2.10) and (3.2.11), R_{ri} is the i^{th} resistance of a nested loop and it consists of the resistances of rotor bars from two slots and the loop overhang. R_e is the lower end ring segment resistance for both rotor types, while R_{er} is the cage upper end ring segment resistance for the cage+NL rotor, and N_r is the total number of rotor slots.

Reverting to (3.2.9), $\boldsymbol{I_r}$ is the rotor loops current vector, and $\boldsymbol{\lambda_r}$ is the rotor loops flux linkage vector. $\boldsymbol{I_r}$ can be represented as

$$\boldsymbol{I_r} = [I_{r_{11}}\ I_{r_{12}}\ I_{r_{13}}\ I_{r_{21}}\ ..\ I_{r_{ni}}\ ..\ I_e]^t, \tag{3.2.12}$$

where, $I_{r_{ni}}$ is the current in the ith loop of a rotor nest n, and I_e is the end ring current. $\boldsymbol{\lambda_r}$ can be calculated as

$$\boldsymbol{\lambda_r} = \boldsymbol{L_r}\boldsymbol{I_r} + \boldsymbol{L}^{\boldsymbol{t}}_{pr}\boldsymbol{I_p} + \boldsymbol{L}^{\boldsymbol{t}}_{cr}\boldsymbol{I_c}, \tag{3.2.13}$$

where, $\boldsymbol{L_r}$ is the rotor loops inductance matrix illustrated in (3.2.14) & (3.2.15) for the NL and cage+NL rotors respectively.

$$\boldsymbol{L}_r = \begin{bmatrix} L_{r_{11}} + L_{l_1} + 5L_e & L_{r_{12}} + 3L_e & L_{r_{13}} + L_e & L_{r_{1,1}} & L_{r_{1,2}} & L_{r_{1,3}} & \cdots & -5L_e \\ L_{r_{21}} + 3L_e & L_{r_{22}} + L_{l_2} + 3L_e & L_{r_{23}} + L_e & L_{r_{2,1}} & L_{r_{2,2}} & L_{r_{2,3}} & \cdots & -3L_e \\ L_{r_{31}} + L_e & L_{r_{32}} + L_e & L_{r_{33}} + L_{l_3} + L_e & L_{r_{3,1}} & L_{r_{3,2}} & L_{r_{3,3}} & \cdots & -L_e \\ L_{r_{1,1}} & L_{r_{1,2}} & L_{r_{1,3}} & L_{r_{11}} + L_{l_1} + 5L_e & L_{r_{12}} + 3L_e & L_{r_{13}} + L_e & \cdots & -5L_e \\ L_{r_{2,1}} & L_{r_{2,2}} & L_{r_{2,3}} & L_{r_{21}} + 3L_e & L_{r_{22}} + L_{l_2} + 3L_e & L_{r_{23}} + L_e & \cdots & -3L_e \\ L_{r_{3,1}} & L_{r_{3,2}} & L_{r_{3,3}} & L_{r_{31}} + L_e & L_{r_{32}} + L_e & L_{r_{33}} + L_{l_3} + L_e & \cdots & -L_e \\ \vdots & \vdots & \vdots & \vdots & \vdots & \vdots & \ddots & \vdots \\ -5L_e & -3L_e & -L_e & -5L_e & -3L_e & -L_e & \cdots & N_rL_e \end{bmatrix} \tag{3.2.14}$$

$$\boldsymbol{L}_r = \begin{bmatrix} L_{r_{11}} + 2L_b + 5L_e + L_{er} & L_{r_{12}} + 3L_e & L_{r_{13}} + L_e & L_{r_{1,1}} - L_b & L_{r_{1,2}} & L_{r_{1,3}} & \cdots & -5L_e \\ L_{r_{21}} + 3L_e & L_{r_{22}} + L_{l_2} + 3L_e & L_{r_{23}} + L_e & L_{r_{2,1}} & L_{r_{2,2}} & L_{r_{2,3}} & \cdots & -3L_e \\ L_{r_{31}} + L_e & L_{r_{32}} + L_e & L_{r_{33}} + L_{l_3} + L_e & L_{r_{3,1}} & L_{r_{3,2}} & L_{r_{3,3}} & \cdots & -L_e \\ L_{r_{1,1}} - L_b & L_{r_{1,2}} & L_{r_{1,3}} & L_{r_{11}} + 2L_b + 5L_e + L_{er} & L_{r_{12}} + 3L_e & L_{r_{13}} + L_e & \cdots & -5L_e \\ L_{r_{2,1}} & L_{r_{2,2}} & L_{r_{2,3}} & L_{r_{21}} + 3L_e & L_{r_{22}} + L_{l_2} + 3L_e & L_{r_{23}} + L_e & \cdots & -3L_e \\ L_{r_{3,1}} & L_{r_{3,2}} & L_{r_{3,3}} & L_{r_{31}} + L_e & L_{r_{32}} + L_e & L_{r_{33}} + L_{l_3} + L_e & \cdots & -L_e \\ . & . & . & L_{r_{1,1}} - L_b & . & . & . & . \\ \vdots & \vdots & \vdots & \vdots & \vdots & \vdots & \ddots & \vdots \\ -5L_e & -3L_e & -L_e & -5L_e & -3L_e & -L_e & \cdots & N_rL_e \end{bmatrix} \tag{3.2.15}$$

From (3.2.14) and (3.2.15), $L_{r_{ii}}$ is the magnetizing inductance of any ith loop, while L_{l_i} is the total leakage inductance in any ith loop. The total leakage in the outer (bar) loops of the cage+NL rotors is $2L_b + L_{er} + 5L_e$, where L_b is the rotor bar leakage inductance, L_{er} is the cage upper end ring segment leakage inductance, and L_e is the lower end ring segment leakage inductance. $L_{r_{ij}}$ is the mutual inductances between any loops i and loop j from the same nest, while $L_{r_{i,j}}$ is the mutual inductances between any loops i and loop j from different nests. Since similar loops in different nests have the same characteristics, there is no need to identify each loop by its nest. The mutual inductances between loops within the same nest are positive because they overlap, while those from different nests do not overlap, and are negative.

Reverting to (3.2.13), $\boldsymbol{L}_{pr}^{t}$ is the instantaneous mutual inductance between the PW and the rotor loops matrix transpose, while $\boldsymbol{L}_{cr}^{t}$ is the instantaneous mutual inductance between the CW and the rotor loops matrix transpose. The lower end ring short-circuits the loops in both rotor types, effectively making all elements of $\boldsymbol{V_r}$ equal to zero at any time instance. Thus, (3.2.9) can be modified to calculate $\boldsymbol{\lambda_r}$ as

$$\boldsymbol{\lambda_r} = -\int \boldsymbol{R_r I_r} dt. \tag{3.2.16}$$

$\boldsymbol{I_r}$ can then be calculated from (3.2.13) as

$$\boldsymbol{I_r} = \boldsymbol{L_r}^{-1}\boldsymbol{\lambda_r} - \boldsymbol{L_r}^{-1}\boldsymbol{L}_{pr}^{t}\boldsymbol{I_p} - \boldsymbol{L_r}^{-1}\boldsymbol{L}_{cr}^{t}\boldsymbol{I_c}. \tag{3.2.17}$$

The instantaneous mutual inductance matrix between the PW and the rotor loops ($\boldsymbol{L}_{pr}$) is represented as

$$\boldsymbol{L}_{pr} = \begin{bmatrix} L_{p_1 r_{11}} & L_{p_1 r_{12}} & \cdots & L_{p_1 r_{ni}} \\ L_{p_2 r_{11}} & L_{p_2 r_{12}} & \cdots & L_{p_2 r_{ni}} \\ L_{p_3 r_{11}} & L_{p_3 r_{12}} & \cdots & L_{p_3 r_{ni}} \end{bmatrix}, \tag{3.2.18}$$

where, $L_{p_m r_{ni}}$ is the instantaneous mutual inductance between PW winding m and a rotor loop i in a nest n. The instantaneous mutual inductance matrix between the CW and the rotor loops, $\boldsymbol{L}_{cr}$, is represented as

$$\boldsymbol{L}_{cr} = \begin{bmatrix} L_{c_1 r_{11}} & L_{c_1 r_{12}} & \cdots & L_{c_1 r_{ni}} \\ L_{c_2 r_{11}} & L_{c_2 r_{12}} & \cdots & L_{c_2 r_{ni}} \\ L_{c_3 r_{11}} & L_{c_3 r_{12}} & \cdots & L_{c_3 r_{ni}} \end{bmatrix}. \tag{3.2.19}$$

where, $L_{c_m r_{ni}}$ is the instantaneous mutual inductance between CW winding m and a rotor loop i in a nest n.

3.2.3 Torque equation

Considering BDFMs as linear magnetic systems, the electromagnetic torque (T_e) can be obtained from the partial derivative of the co-energy with respect to the rotor position. Similar to [80, 81], T_e is calculated as

$$T_e = \begin{bmatrix} \boldsymbol{I}_{\boldsymbol{p}}^{t} & \boldsymbol{I}_{\boldsymbol{c}}^{t} \end{bmatrix} \begin{bmatrix} \frac{d\boldsymbol{L}_{pr}}{d\theta} \\ \frac{d\boldsymbol{L}_{cr}}{d\theta} \end{bmatrix} \boldsymbol{I_r}, \tag{3.2.20}$$

where, $\boldsymbol{I_c}$ is the CW current vector represented as

$$\boldsymbol{I_c} = [I_{c_1}\ I_{c_2}\ I_{c_3}]^{t}. \tag{3.2.21}$$

$\frac{d\mathbf{L}_{pr}}{d\theta}$ is the matrix of the change in mutual inductances between the PW and the rotor loops with changes in position, and $\frac{d\mathbf{L}_{cr}}{d\theta}$ is the matrix of the change in mutual inductances between the CW and the rotor loops with changes in position.

3.2.4 Inductance calculation using the WFT

The winding function (WF), $N(\theta)$, of a machine winding is the MMF distribution of that winding for a current of 1 A [82]. The WF can be calculated as

$$N(\theta) = n(\theta) - \langle n(\theta) \rangle, \tag{3.2.22}$$

where, $n(\theta)$ is the turns function, and $\langle n(\theta) \rangle$ is the average value of the turns function along the core periphery. The turns function is the number of series turns (N) enclosed in the winding [82]. The average turns function ($\langle n(\theta) \rangle$) can be calculated as

$$\langle n(\theta) \rangle = \frac{1}{2\pi} \int_0^{2\pi} n(\theta) d\theta. \tag{3.2.23}$$

Single layer phase windings with p pole pairs can be considered as consisting of q concentrated full pitch coils, where q is the number of slots per pole per phase. These concentrated coils with N number of series turns (equal to the number of turns in the slot), are displaced by $\frac{\pi}{3pq}$ for 3-phase windings. The phase WF can then be obtained by adding the WFs of these concentrated coils together. In Figure 3.3, the WF of an arbitrary phase winding with p pole pairs and q = 3, is illustrated by combining WFs of 3 concentrated full pitch coils. It should be noted that in Figure 3.3, n_c is the number of turns in a slot.

The magnetizing inductance of phase winding a (L_{aa}) is calculated using its WF ($N_a(\theta)$) as

$$L_{aa} = \frac{\mu_0 r l}{g} \int_0^{2\pi} N_a^2(\theta) d\theta, \tag{3.2.24}$$

where, μ_0 is the permeability of free space, r is the machine airgap radius, l is the machine stack length, and g is the airgap length [82]. The mutual inductance between phase winding a and another phase winding b (L_{ab}) is calculated as

$$L_{ab} = \frac{\mu_0 r l}{g} \int_0^{2\pi} N_a(\theta) N_b(\theta) d\theta. \tag{3.2.25}$$

3.2.5 NL rotor inductance calculations using the WFT

The turns function and WF of a rotor loop are illustrated in Figure 3.4. The number of series turns for a nested loop made of bars is 1, and the magnetizing inductance of an arbitrary rotor loop i, $L_{r_{ii}}$, is

$$L_{r_{ii}} = \frac{\mu_0 r l}{g} \alpha_i \left(1 - \frac{\alpha_i}{2\pi}\right), \tag{3.2.26}$$

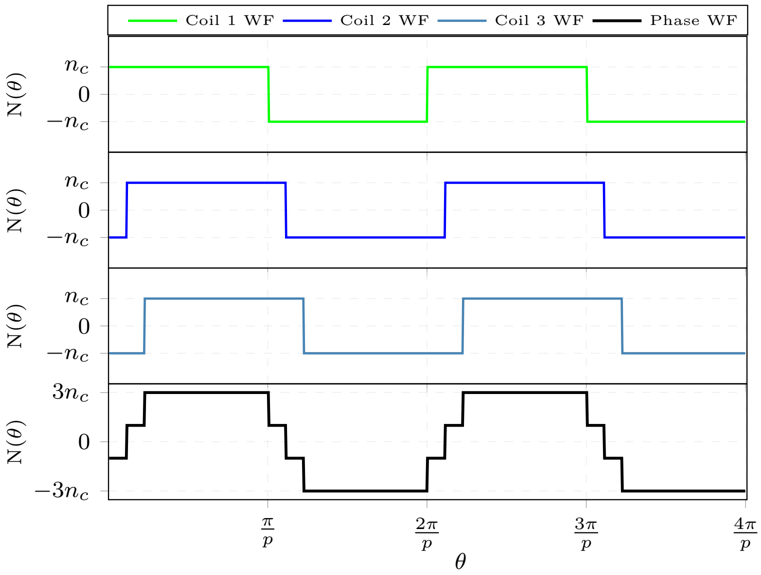

Figure 3.3: *Combination of the WFs of 3 concentrated full pitch coils to form the WF of a phase winding with p pole pairs and q = 3.*

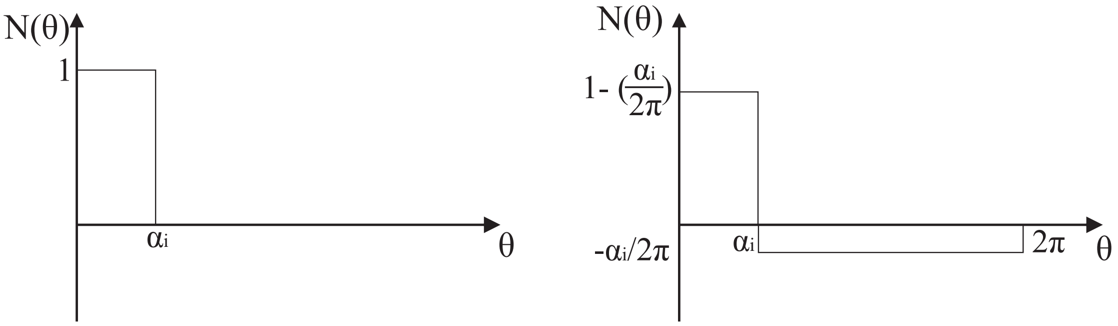

(a) **(b)**

Figure 3.4: *(a) Turns function of a rotor loop$_i$ (b) WF of loop$_i$.*

where, α_i is the angular loop span of loop i [83]. The mutual inductance, $L_{r_{ni,nj}}$, between two rotor loops i and j in the same nest n, with loop spans α_i & α_j respectively, is calculated as

$$L_{r_{ni,nj}} = \frac{\mu_0 rl}{g} \alpha_j \left(1 - \frac{\alpha_i}{2\pi}\right), \tag{3.2.27}$$

where, $\alpha_i > \alpha_j$. For loops in different nests, e.g. loop i in nest n and loop j in nest k, with loop spans α_i and α_j respectively, the mutual inductance $L_{r_{ni,kj}}$ is

$$L_{r_{ni,kj}} = \frac{\mu_0 rl}{g} \left(\frac{-\alpha_i \alpha_j}{2\pi}\right). \tag{3.2.28}$$

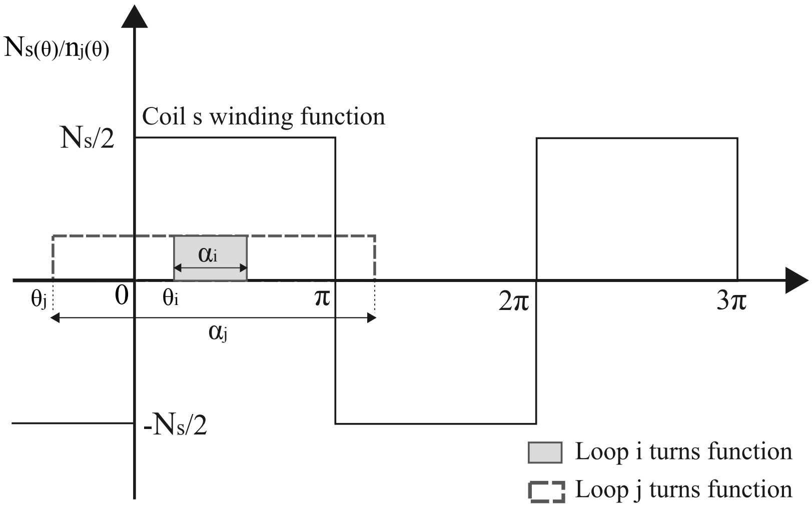

Figure 3.5: *Rotor loops turns functions in relation to a concentrated stator coil winding function*

3.2.6 Mutual inductance between stator and rotor windings calculation using WFT

For convenience, the mutual inductances between a stator winding and rotor loops are first described using a full pitch, 2 pole, concentrated stator coil. The positioning of two rotor loops i and j with different loop spans relative to the concentrated stator coil s with N_s [1] series turns, is illustrated in Figure 3.5. Loop i has a loop span, α_i, which is less than the pole span of the coil s, while loop j has loop span, α_j, which is greater than the pole span of coil s. In general, most loops in BDFM rotors are like loop i, with loop spans less than either the PW or the CW pole spans. However, the loops formed by the (p_1+p_2) cage bars in the cage+NL rotor are generally longer than the CW pole span, hence the consideration of loop type j.

The instantaneous mutual inductance L_{sr_k} between coil s and any rotor loop k regardless of loop span is given as

$$L_{sr_k} = \frac{\mu_0 rl}{g}\int_0^{2\pi} N_s(\theta)N_k(\theta)d\theta, \tag{3.2.29}$$

where, $N_s(\theta)$ is the WF of coil s, and $N_k(\theta)$ is the WF of rotor loop k. Four distinct regions in the calculation of the mutual inductance (L_{sr}) between the 2 pole concentrated stator coil s and the rotor loops are illustrated in Figure 3.6. It should be noted that the left hand side of the rotor turns functions is taken as the reference point for θ.

---

[1] N_s is used for consistency with conventional WF notations in literature. N_s refers to number of stator slots in other chapters of this dissertation

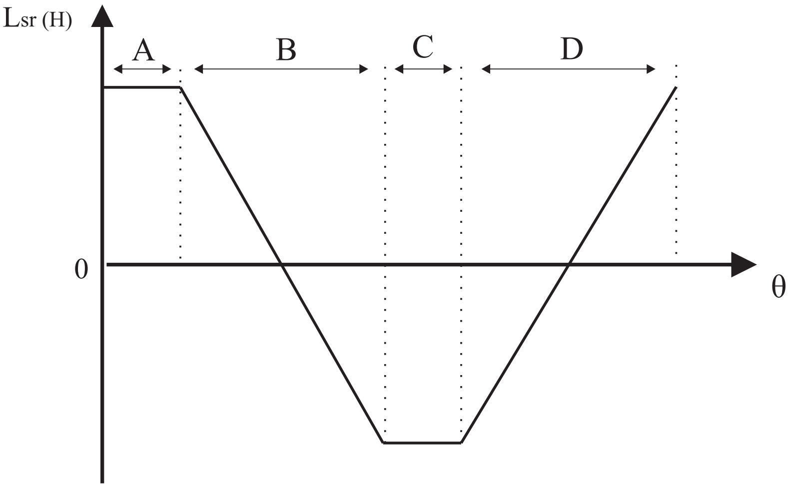

Figure 3.6: *Mutual inductance between a concentrated stator coil and a rotor loop*

The mutual inductance between coil s and rotor loop type i (L_{sr_i}) in these regions is calculated as

$$\begin{array}{lll}
A. & L_{sr_i} = \frac{\mu_0 rl}{g}\frac{N_s}{2}\alpha_i, & 0 \le \theta_i \le \pi - \alpha_i. \\
B. & L_{sr_i} = \frac{\mu_0 rl}{g}\frac{N_s}{2}(2\pi - 2\theta_i - \alpha_i), & \pi - \alpha_i < \theta_i \le \pi. \\
C. & L_{sr_i} = -\frac{\mu_0 rl}{g}\frac{N_s}{2}\alpha_i, & \pi < \theta_i \le 2\pi - \alpha_i. \\
D. & L_{sr_i} = \frac{-\mu_0 rl}{g}\frac{N_s}{2}(4\pi - 2\theta_i - \alpha_i), & 2\pi - \alpha_i < \theta_i \le 2\pi.
\end{array} \tag{3.2.30}$$

The mutual inductance between coil s and rotor loop type j (L_{sr_j}) in these regions is calculated as

$$\begin{array}{lll}
A. & L_{sr_j} = \frac{\mu_0 rl}{g}\frac{N_s}{2}(2\pi + \alpha_j), & \theta_j \le 0\ ,\ \theta_j + \alpha_j \ge \pi. \\
B. & L_{sr_j} = \frac{\mu_0 rl}{g}\frac{N_s}{2}(2\pi - 2\theta_j - \alpha_j), & \theta_j > 0\ ,\ \theta_j + \alpha_j < 2\pi. \\
C. & L_{sr_j} = -\frac{\mu_0 rl}{g}\frac{N_s}{2}(2\pi + \alpha_j), & \theta_j \le \pi\ ,\ \theta_j + \alpha_j \ge 2\pi. \\
D. & L_{sr_j} = -\frac{\mu_0 rl}{g}\frac{N_s}{2}(4\pi - 2\theta_j - \alpha_j), & \theta_j > \pi\ ,\ \theta_j + \alpha_j < 3\pi.
\end{array} \tag{3.2.31}$$

The change in mutual inductance between coil s and loop type i with respect to position $\left(\frac{dLsr_i}{d\theta_i}\right)$

is calculated in the four regions as

$$\begin{aligned}
&A. \quad \frac{dL_{sr_i}}{d\theta_i} = 0, && 0 \leq \theta_i \leq \pi - \alpha_i. \\
&B. \quad \frac{dL_{sr_i}}{d\theta_i} = \frac{-2\mu_0 rl}{g}\frac{N_s}{2}, && \pi - \alpha_i < \theta_i \leq \pi. \\
&C. \quad \frac{dL_{sr_i}}{d\theta_i} = 0, && \pi < \theta_i \leq 2\pi - \alpha_i. \\
&D. \quad \frac{dL_{sr_i}}{d\theta_i} = \frac{2\mu_0 rl}{g}\frac{N_s}{2}, && 2\pi - \alpha_i < \theta_i \leq 2\pi.
\end{aligned} \tag{3.2.32}$$

The change in mutual inductance between coil s and loop type j with respect to position $\left(\frac{dLsr_j}{d\theta_j}\right)$ is calculated in the four regions as

$$\begin{aligned}
&A. \quad \frac{dL_{sr_j}}{d\theta_j} = 0, && \theta_j \leq 0\,,\ \theta_j + \alpha_j \geq \pi. \\
&B. \quad \frac{dL_{sr_j}}{d\theta_j} = -\frac{2\mu_0 rl}{g}\frac{N_s}{2}, && \theta_j > 0\,,\ \theta_j + \alpha_j < 2\pi. \\
&C. \quad \frac{dL_{sr_j}}{d\theta_j} = 0, && \theta_j \leq \pi\,,\ \theta_j + \alpha_j \geq 2\pi. \\
&D. \quad \frac{dL_{sr_j}}{d\theta_j} = \frac{2\mu_0 rl}{g}\frac{N_s}{2}, && \theta_j > \pi\,,\ \theta_j + \alpha_j < 3\pi.
\end{aligned} \tag{3.2.33}$$

Generally, distributed phase windings with p pole pairs greater than 1 are used in BDFM stators. In applying equations (3.2.30) - (3.2.33), the $\frac{Ns}{2}$ term becomes $\frac{Ns}{2p}$. It should also be noted that θ is the mechanical angle. Coils with higher p pole pairs will have smaller pole spans, such that during one complete mechanical revolution, there will be p repetitions of the regions in equations (3.2.30) - (3.2.33).

It should be recalled that the stator phase windings can be broken down into a group of q concentrated coils displaced by a stator slot pitch. These concentrated coils WFs can be used in calculating the mutual inductances between a stator phase winding and a rotor loop.

3.3 Simulation Results and Discussion

The CC model is developed using MATLAB®scripts, and two BDFMs sized for a 160L induction machine frame (with identical stator windings) are simulated. One BDFM has an NL rotor, and the other, a cage+NL rotor. The specifications of the BDFMs are given in Table D.2. Three rotor loops per nest are initially considered because of the machine ratings and following trends in literature like [9, 50, 86]. Rotors with more loops per nest are considered later.

A flow chart summarizing the CC model simulation and highlighting the relevant equations at each step is illustrated in Figure 3.7. The WFs of the PW and CW are first obtained. The PW

Table 3.1: *160L frame BDFM design specifications*

Item	Symbol	Unit	Value
Grid voltage (rms)	V_p	V	230
PW frequency	f	Hz	50
Rated slip	-	-	-0.35
PW current (rms)	I_p	A	4.77
CW current (rms)	I_c	A	3.16
PW pole pairs	p_1	-	2
CW pole pairs	p_2	-	3
Natural speed	ω_n	rpm	600
Airgap length	g	mm	0.35
Stack length	l	mm	240
Airgap radius	r	mm	85.5
Stator slots	-	-	36
PW turns per phase	N_{pw}	-	234
CW turns per phase	N_{cw}	-	432
NL rotor slots	-	-	30
Cage+NL rotor slots	-	-	25

inductances, L_p, are calculated using the PW WFs, while the PW resistances, R_p, are calculated using the stator resistance formula in [16]. Initial simulation conditions such as the initial rotor position, load angle etc., are set and a time function is initialized. The instantaneous stator excitations are calculated together with the stator to rotor mutual inductances. The first set of simulation output are the rotor loop currents and flux linkages. These are used to calculate the PW flux linkages and currents from which the machine torque is then calculated.

2D time stepping FEA simulations of the two BDFMs are compared with the CC models simulations. The FEA models are developed in ANSYS Maxwell®. An axial cross section of a 2D FEA model of the BDFM with an NL rotor is illustrated in Figure 3.8. The full model has to be simulated because of the lack of symmetry in the machine, leading to lengthy simulations. The flux lines in Figure 3.8 demonstrate the $p_1 + p_2$ (5 in this case) rotating machine pole pairs. The PW occupies the bottom layer of the stator in the FEA model, while the CW occupies the top layer. The FEA models' rotor windings are developed using external circuits in ANSYS Maxwell®. Each rotor loop is designated as a winding connected to its calculated resistances and end connection leakage similar to Figure 3.1. However, the bars in the cage+NL rotor are designated as individual windings with resistances to enable parallel connections like in Figure 3.2. The M400-50A steel lamination type is used for all the BDFM FEA models with non-linearity of the core B-H curve considered.

The (CC & FEA) models PWs are excited with 3-phase voltage excitations, while the CWs are excited with 3-phase current excitations which have load angles relative to the PW voltage

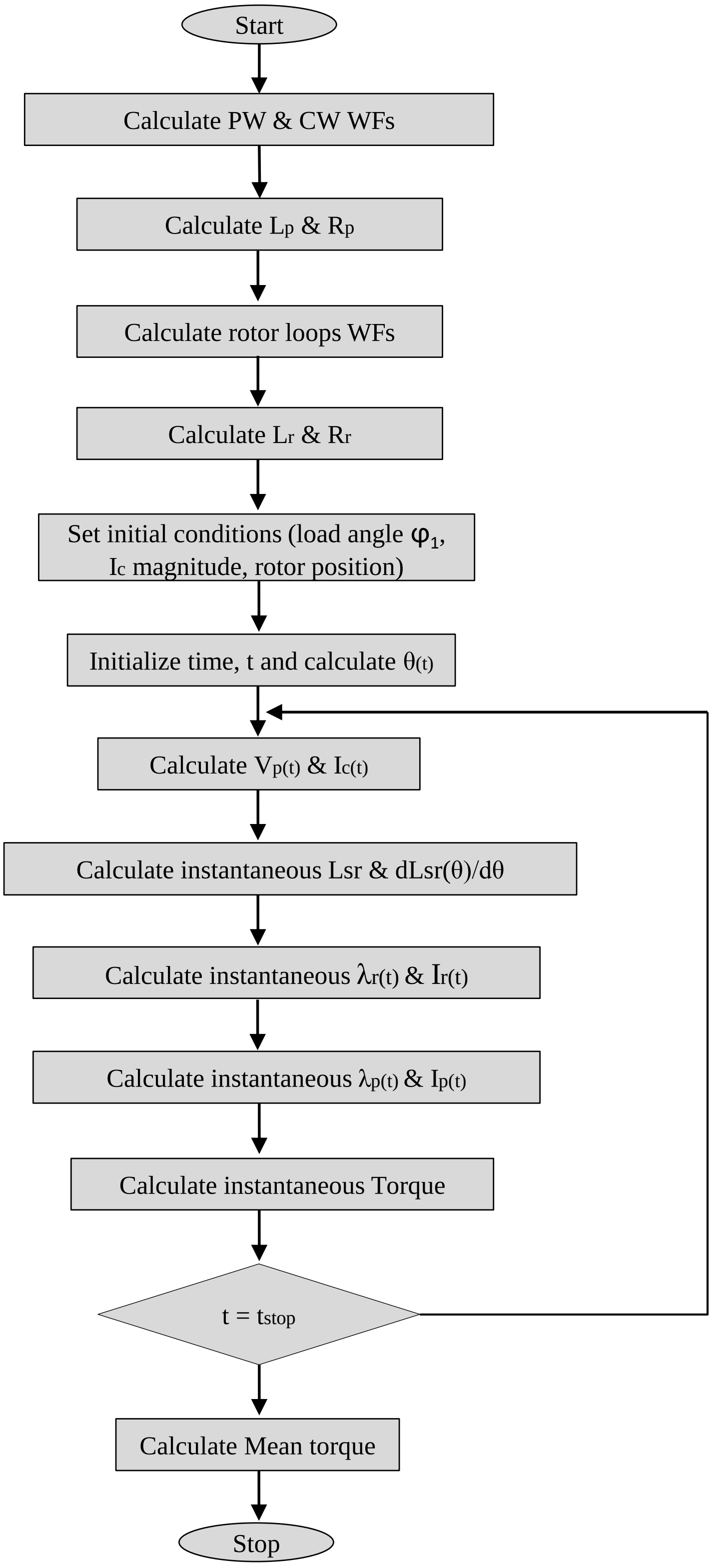

Figure 3.7: *Flowchart of CC model simulation in MATLAB®.*

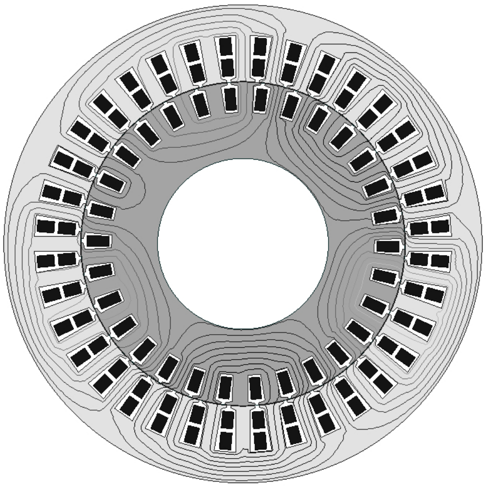

Figure 3.8: *FEA model with flux lines of BDFM with an NL rotor.*

excitations. The instantaneous 3-phase CW currents ($\boldsymbol{I_c}$) are calculated as

$$\begin{aligned} I_{c_1} &= \hat{I}_c\, sin(2\pi f_2 t - \varphi_1), \\ I_{c_2} &= \hat{I}_c\, sin(2\pi f_2 t - \frac{2\pi}{3} - \varphi_1), \\ I_{c_3} &= \hat{I}_c\, sin(2\pi f_2 t + \frac{2\pi}{3} - \varphi_1), \end{aligned} \tag{3.3.1}$$

where, $\hat{I}_c$ is the peak value of the rated CW current, and φ_1 is the load angle. All simulations results for the (CC & FEA) models are obtained at steady states.

3.3.1 Stator to rotor mutual inductances

The CC model mutual inductances between the stator windings (PW & CW) and rotor loops of the BDFM with NL rotor are illustrated in Figure 3.9, while mutual inductances between the stator windings (PW & CW) and rotor loops of the BDFM with cage+NL rotor are illustrated in Figure 3.10. At first glance, it appears that wider rotor loops lead to smaller flat tops with rounded/sinusoidal edges of the mutual inductance waveform. This is the case for rotor loops with loop spans less than the stator winding pole span like the outer loop in Figure 3.9(a), the cage bar loop in Figure 3.10(a) and the middle loop in Figure 3.10(b). For loops with spans greater than the stator pole spans (such as the bar loop compared to the CW in Figure 3.10(b)), a further increase in loop span leads to an increase in the waveform flat top, as can be observed from (3.2.31).

The outer loop of the BDFM with an NL rotor has a loop span which is the same as the CW pole span. In this case, the winding slot distribution of the CW has no major effect on its mutual inductance with the outer loop's waveform. The CW then couples similar to

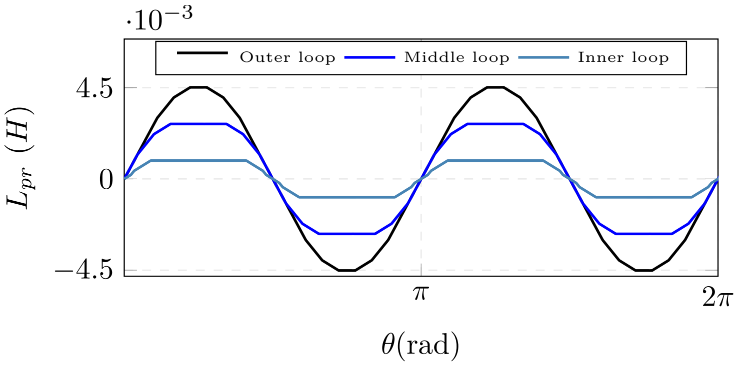

(a)

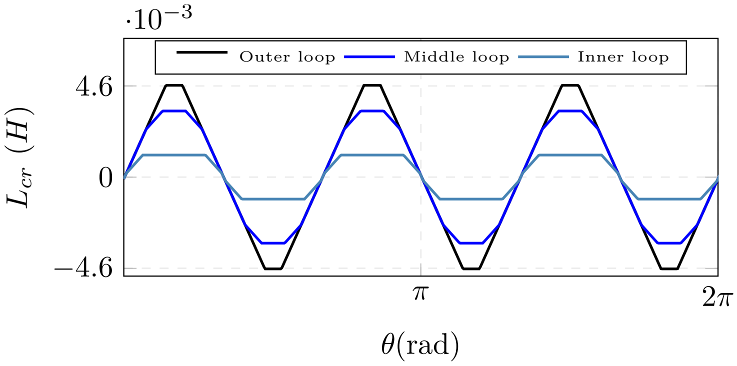

(b)

Figure 3.9: *CC model mutual inductances between rotor loops in the NL rotor and (a) the PW (b) the CW.*

a concentrated coil with the rotor outer loop, hence the similarity of the mutual inductance waveform illustrated in Figure 3.9(b) with Figure 3.6.

3.3.2 Electromagnetic Torque

The mean torques at varying load angles for the BDFM with the NL rotor are illustrated for the different models at zero and -0.35 slip in Figure 3.11(a) and Figure 3.11(b) respectively. It should be noted that the load angles in Figure 3.11 are used for illustration, and are not exact control based angles.

The mean torques at varying load angles for the BDFM with the cage+NL rotor are illustrated for the different models at zero and -0.35 slip in Figures 3.12(a) and 3.12(b) respectively. The torque values of the CC models closely match those of the FEA models for both rotor types at zero slip, with a slightly more noticeable variation at -0.35 slip.

The maximum generating torque achieved is higher than the maximum motoring torque for both BDFMs. Also, the BDFM with the cage+NL rotor produces slightly higher generating/-motoring torque than the BDFM with the NL rotor for both CC and FEA models.

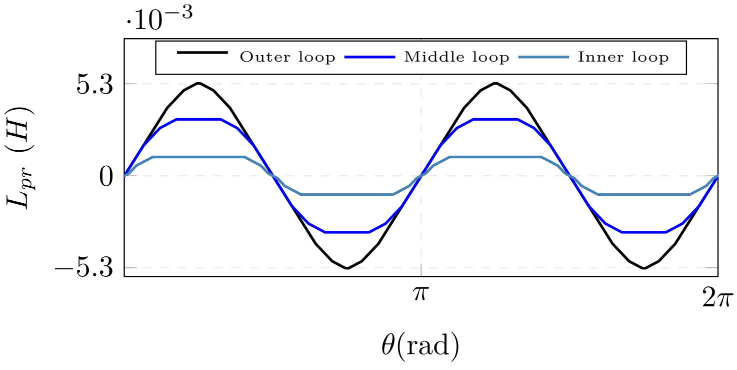

(a)

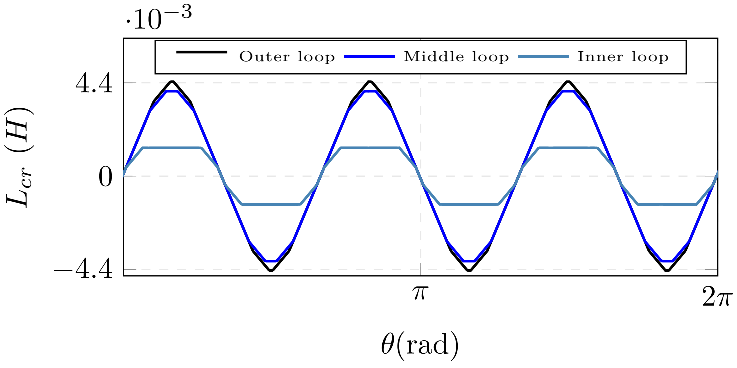

(b)

Figure 3.10: *CC model mutual inductances between rotor loops in the cage+NL rotor and (a) the PW (b) the CW.*

Using the CC model, the torque contributions of the rotor loops are investigated. This investigation is conducted using two sets of simulations. For the first set, different loops are removed from the rotors, and the total torques produced in the machines at varying load angle are illustrated in Figures 3.13(a) and 3.13(b) for the NL and cage+NL rotors respectively. It is observed that the removal of the outer loops leads to the highest drops in torque production in both rotors. This suggests that the outer loops in both rotors have the largest contributions to torque production. This also corresponds with suggestions in [10], that wider loops contribute more to torque production.

However, the drop in torque production due to the removal of the outer loop in the cage+NL rotor in Figure 3.13(b) is smaller than that of the outer loop of the NL rotor in Figure 3.13(a). The converse may have been expected as the outer loop of the cage+NL rotor is wider than the outer loop of the NL rotor.

To further investigate the loop contributions, the torque contributions of the loops at varying load angles are then separated without the removal of any loops using the CC models. These torque contributions of the loops at varying load angles are illustrated in Figures 3.14(a) and 3.14(b) for the BDFMs with NL and cage+NL rotors respectively. It should be noted that this

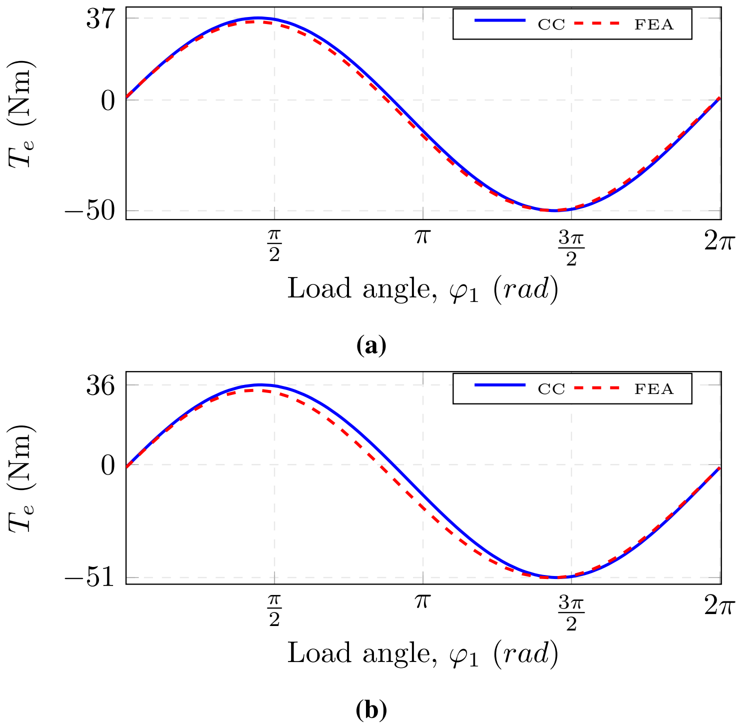

(a)

(b)

Figure 3.11: *CC and FEA models mean torque at varying load angles of BDFM with the NL rotor at (a) zero slip (b) -0.35 slip.*

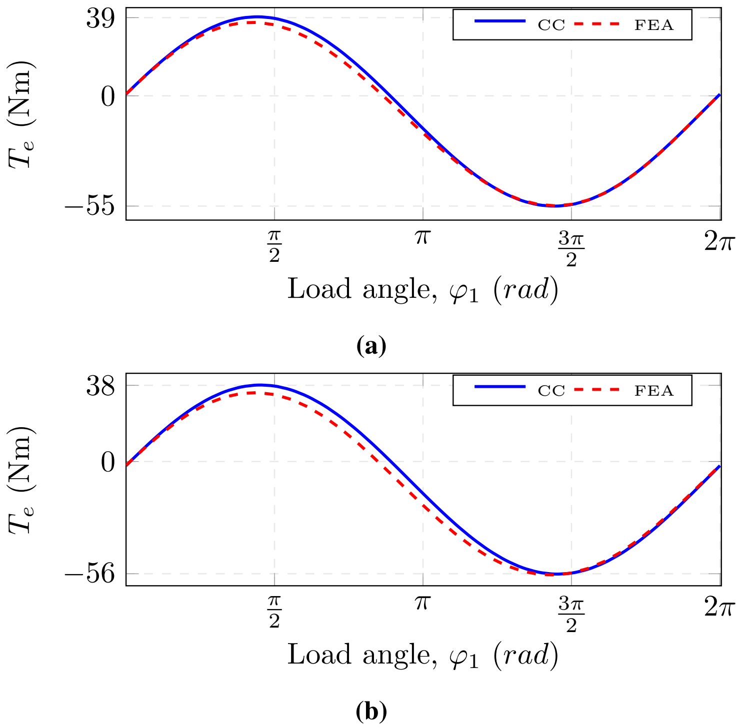

(a)

(b)

Figure 3.12: *CC and FEA models mean torque at varying load angles of BDFM with the cage+NL rotor at (a) zero slip (b) -0.35 slip.*

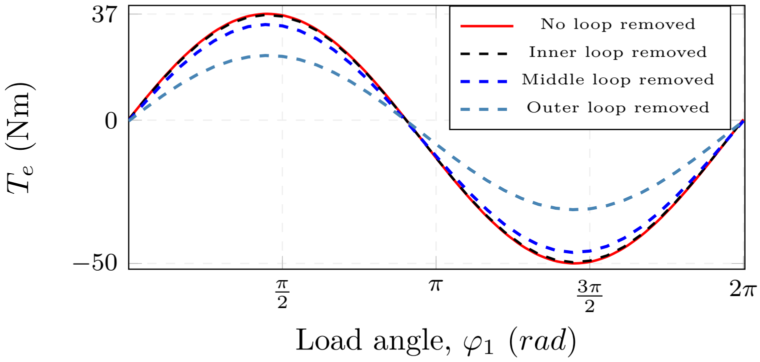

(a)

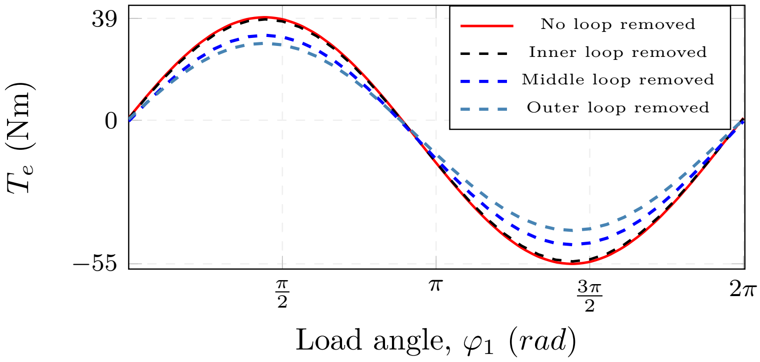

(b)

Figure 3.13: *CC models mean torque at varying load angles with different rotor loops removed (a) NL rotor (b) cage+NL rotor.*

type of separation is difficult to conduct using the FEA models.

The torque contributions of the loops of the BDFM with the NL rotor are straightforward; The wider the loop, the greater the torque contribution. However, for the BDFM with the cage+NL rotor, the outer loop does not provide the largest contribution to the torque as illustrated in Figure 3.14(b). The loss in torque contribution of the outer loops in the cage+NL rotor is attributed to the shared rotor bars of outer loops in adjacent nests.

3.3.3 Torque ripple

Wind turbines are typically required by grid codes to run between 0.95 leading and lagging power factors [87]. Unity power factor condition falls in the middle of this range, and the torque ripple produced in the machines at generating unity power factor is investigated. Using the FEA and CC models, the torque produced at generating unity power factor conditions are illustrated in Figures 3.15(a) & 3.15(b) for the BDFMs with the NL and cage+NL rotors respectively.

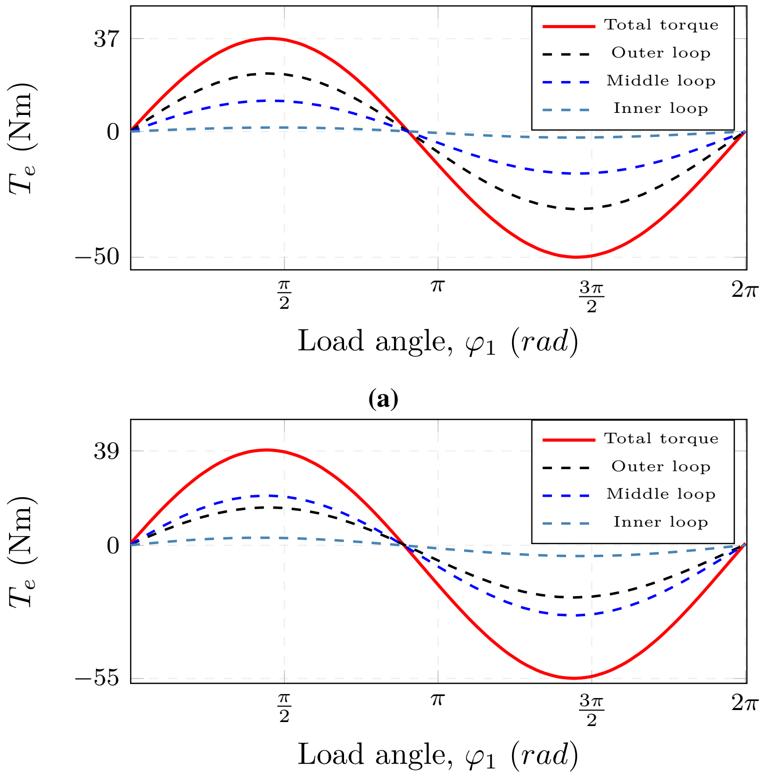

(a)

(b)

Figure 3.14: *CC models loop torque contributions at varying load angles of BDFM with the (a) NL rotor (b) cage+NL rotor.*

The FEA models produce less torque ripple than the CC models for both rotor types, and this is likely due to the absence of slot effects in the CC models. Also, the difference in leakage calculations between the CC and FEA models are possible additional causes for the difference in ripple. Although the CC models produced greater ripple, both models for the BDFM with the cage+NL rotor produced less ripple than their corresponding models for the BDFM with the NL rotor. This illustrates a sensitivity of the CC models to the different rotor types. The frequencies of torque oscillation are also the same for both model types.

Using the CC models, plots of the contributions of the different rotor loops to the unity power factor generating torque are illustrated in Figures 3.16(a) and 3.16(b) for the BDFMs with the NL and cage+NL rotors respectively. It is observed that the outer loops of both BDFMs produce the largest ripples. It should be recalled that the outer loop of the BDFM with the cage+NL rotor contributes less torque than the middle loop as illustrated in Figure 3.14(b), and also highlighted in Figure 3.16(b). Also, it can be observed that the loop torque ripples in the NL rotor are in step with each other, while the torque ripple of the outer loop of the cage+NL rotor is not in step with the ripples of the other loops. As a result, the torque ripples of the loops in an NL rotor add up, while the loop torque ripples in the cage+NL rotor have a

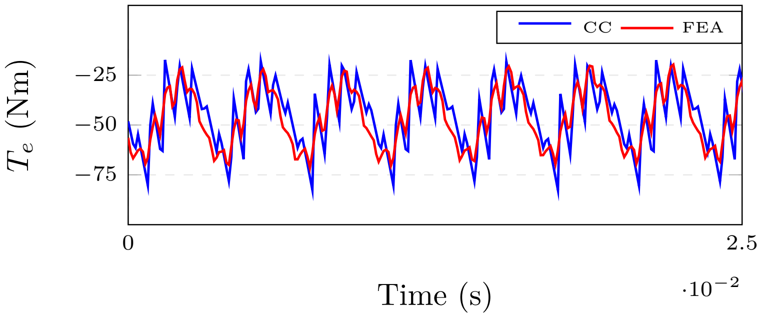

(a)

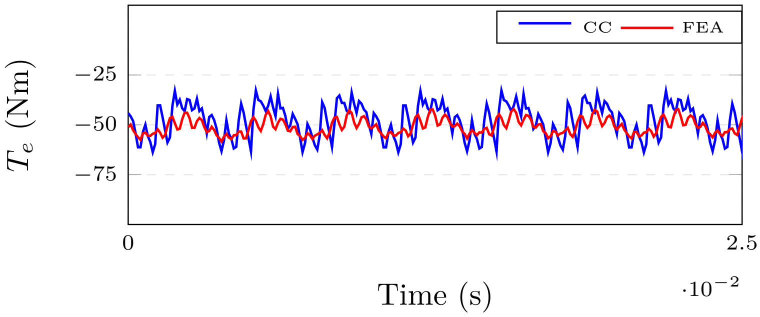

(b)

Figure 3.15: *Generating unity power factor torque from CC and FEA models of BDFM with the (a) NL rotor (b) cage+NL rotor.*

more complex interaction.

Using the CC models, the torque contributions of the PW and CW at generating unity power factor are separately illustrated in Figures 3.17(a) and 3.17(b) for the BDFMs with NL and cage+NL rotors respectively. The PW torque contribution for both rotor types are closely matched in ripple and magnitude. However, the torque ripple produced by the CW in the BDFM with NL rotor is significantly higher than the torque ripple produced by the CW in the BDFM with cage+NL rotor. Also, the CW contributes more torque in both BDFMs.

The reason for the higher torque ripple generated in the BDFM with the NL rotor can be explained using the mutual inductance between the CW and the outer loop of that particular NL rotor. Due to the peculiar situation where the CW pole span is equal to the NL rotor outer loop span, the effects of slot distribution are lost. The CW couples like a concentrated coil with the NL rotor outer loop, generating more harmonics, and consequently more torque ripple.

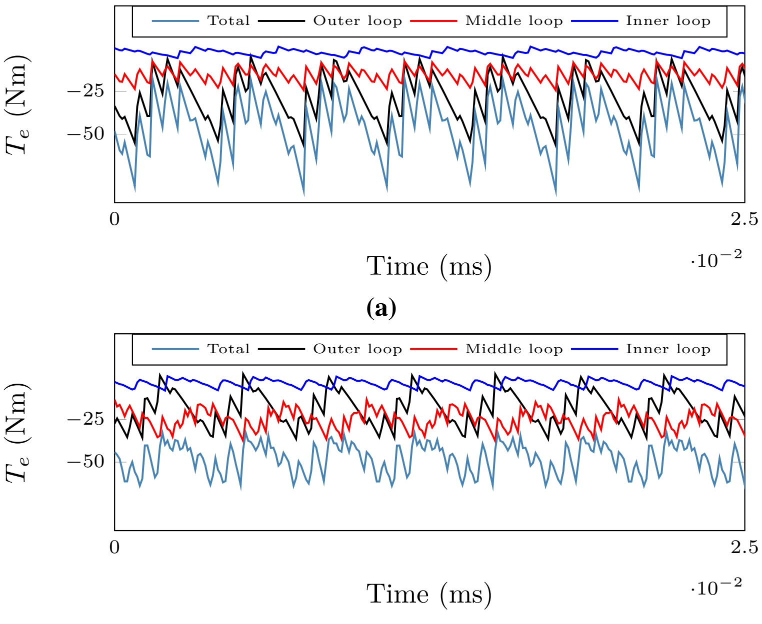

(a)

(b)

Figure 3.16: *Rotor loops torque contributions using CC models of BDFM with the (a) NL rotor (b) cage+NL rotor.*

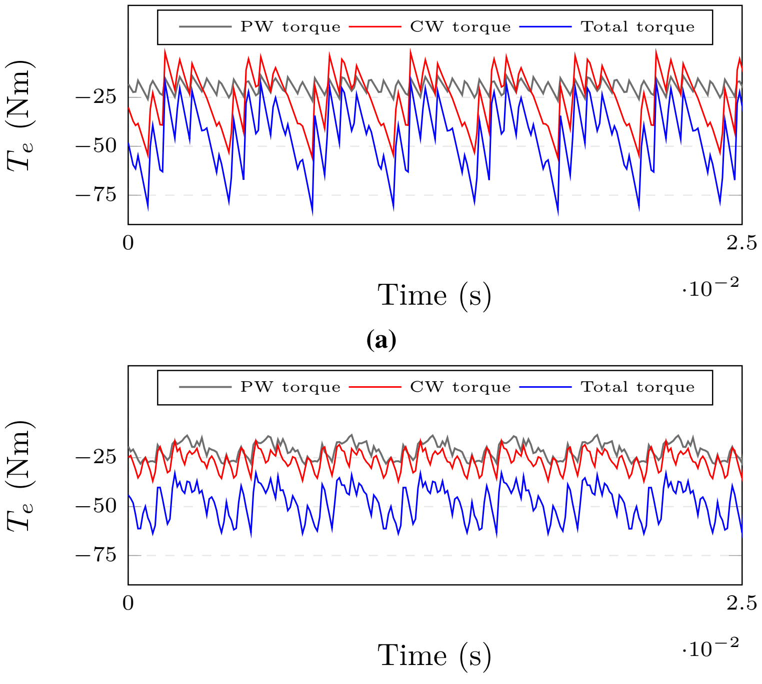

(a)

(b)

Figure 3.17: *PW and CW torque contributions using CC models of BDFM with the (a) NL rotor (b) cage+NL rotor.*

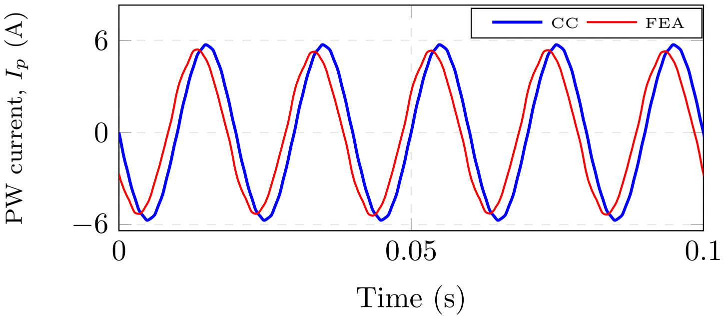

Figure 3.18: *CC and FEA models PW phase current at generating unity power factor of BDFM with the NL rotor.*

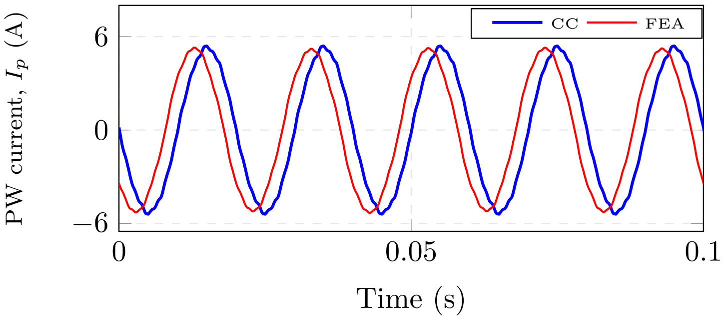

Figure 3.19: *PW phase current from CC and FEA models at generating unity power factor of BDFM with the cage+NL rotor.*

3.3.4 Stator and Rotor currents

The FEA and CC models PW phase currents are illustrated in Figures 3.18 and 3.19 for the BDFMs with the NL and cage+NL rotors respectively at unity power factor generating conditions. The PW currents of both BDFMs with the different rotors and both models match closely. The loop currents of the BDFM with the NL rotor at peak generating torque are illustrated in Figure 3.20 for the CC and FEA models, while those of the BDFM with the cage+NL rotor at generating unity power factor are illustrated in Figure 3.21. It should be noted that the FEA model currents in Figures 3.18 - 3.21 are shifted ahead slightly for clearer illustration.

The loop currents in the NL rotor for both models have similar waveforms and peak values. It can be observed that the loop currents in an NL rotor nest are all in phase, with the wider loops having higher current magnitudes.

Different windings cannot share coil-sides/bars in ANSYS Maxwell®. Thus, the cage+NL rotor outer loops (cage loops) cannot be modeled as windings, as done in the CC model. Instead, for the FEA model, the cage bars in the cage+NL rotor are modeled as individual windings and connected to the other loops using the external circuit, as mentioned in section 3.3. As a result, the FEA bar currents are obtainable, but the outer loop currents are not.

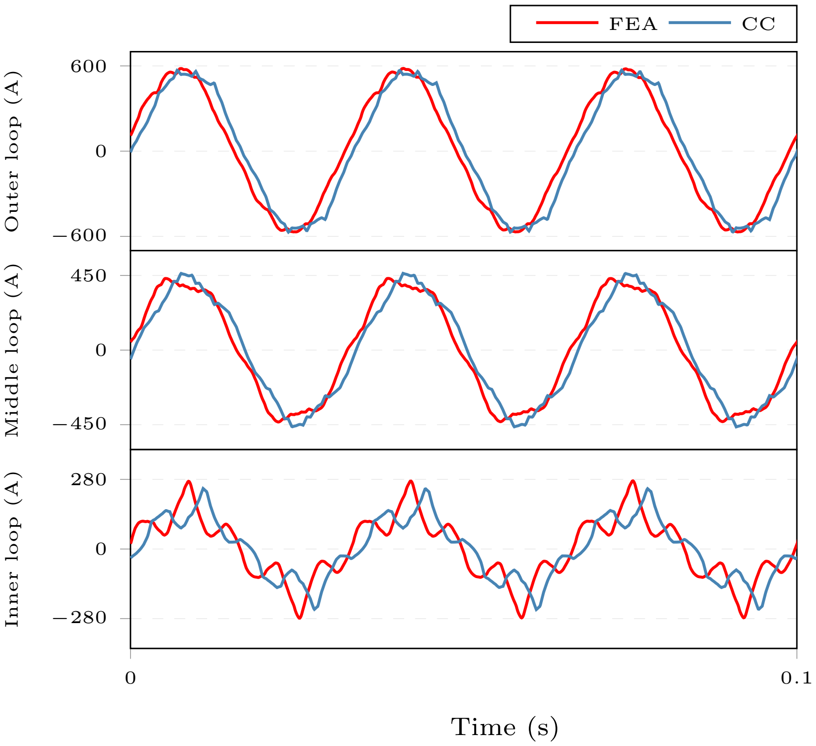

Figure 3.20: *Rotor loop currents of BDFM with the NL rotor at peak generating torque.*

This is why only the CC model outer loop currents are illustrated in Figure 3.21. The bar currents in the CC model are obtained by post-processing operations whereby adjacent outer loop currents are subtracted to obtain their shared bar currents.

The currents of the nested loops in the cage+NL rotor are also in phase, and the current waveforms and peak values for both model types are similar. The illustrated bar currents lead the nested loop currents by approximately the rotor slot pitch. However, the combinations of adjacent bars which form the outer loops of the cage+NL rotor, cause the outer loop current to be in phase with nested loops in the same nest of the cage+NL rotor. It can be observed that the outer loop peak current is less than the middle loop peak current. This provides further understanding of why the torque contribution of the cage+NL rotor outer loop is lower than the middle loop contribution.

3.3.5 Effect of the number of stator slots and rotor loops in a nest

CC models are used to examine the effects of the number of nest loops on torque capabilities and ripple. As stated earlier, three loops per nest were initially selected for the BDFM rotors. Each rotor slot is assumed to be equidistant to adjacent slots. The torque produced at generating unity power factor in BDFMs designed for 160L frames with similar specifications given in Table D.2, but different number of rotor loops, are illustrated in Figure 3.22(a). The torque

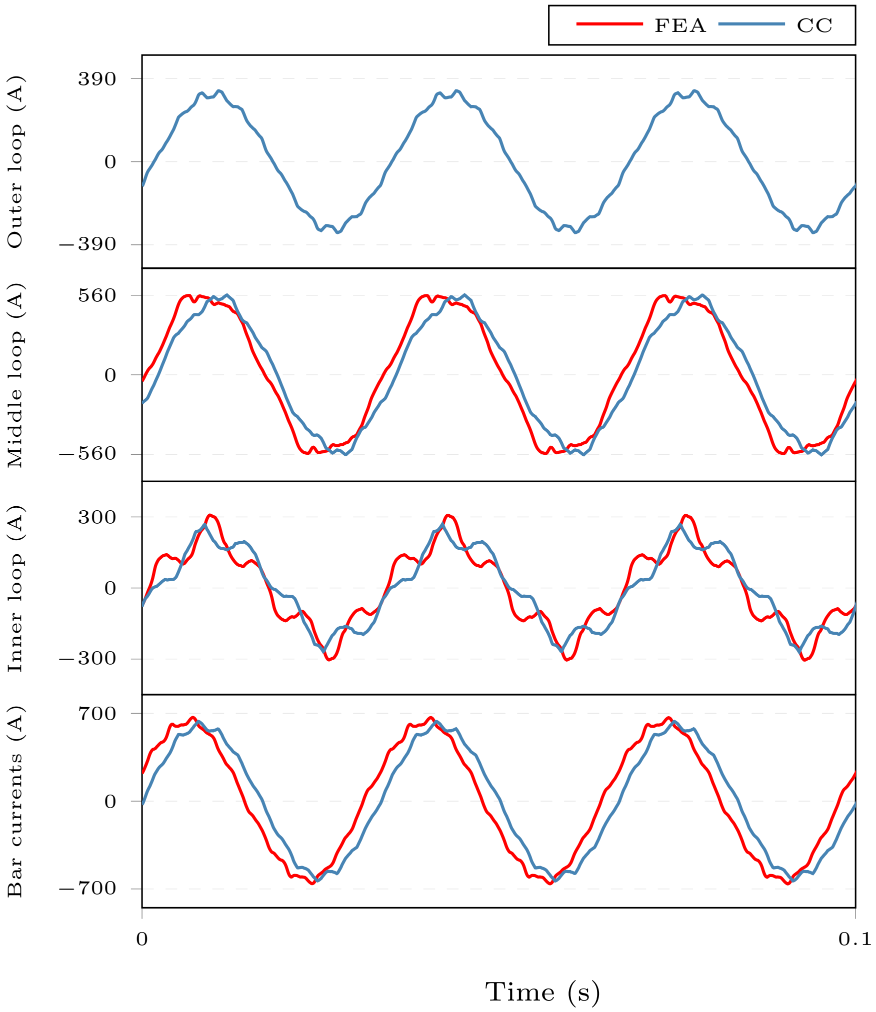

Figure 3.21: *Rotor loop currents of BDFM with the cage+NL rotor at generating unity power factor.*

ripple produced in the machines is also illustrated in Figure 3.22(b).

It should be noted that the large number of loops may not always be practical depending on the machine rating/framesize. The highest torque for the BDFM with the NL rotor is obtained at 3 loops, and four loops for the BDFM with the cage+NL rotor, after which the torque reduces progressively with increasing loops.

There is a general decrease in torque ripple with increases in loops for both BDFMs with the different rotors. However, it is observed that there are spikes in torque ripple for every loops per nest number which is a multiple of three.

A different pole pair combination ($p_1 = 2$, $p_2 = 4$) is used to compare the initial combination. To achieve some fairness in comparison, similar stator slot numbers are used. 72 stator slots is the smallest possible number of stator slots that can work with both pole pair combinations.

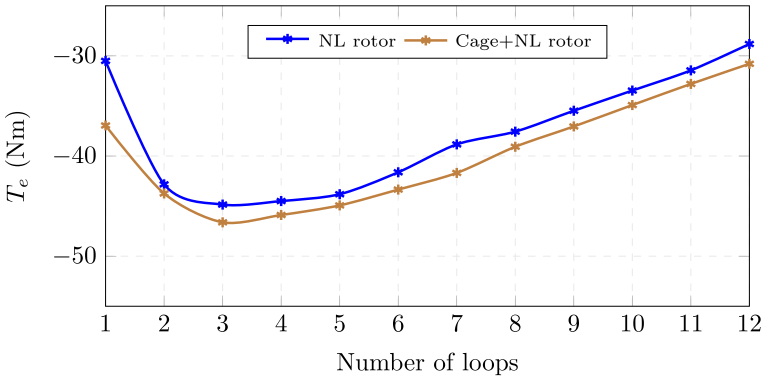

(a)

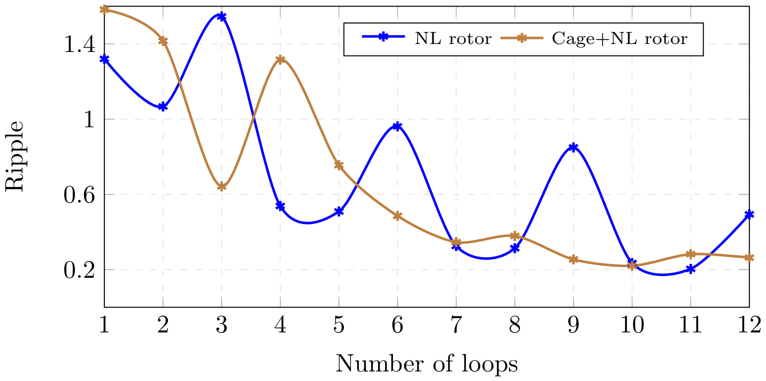

(b)

Figure 3.22: *Effect of rotor loops on (a) Torque (b) Torque ripple.*

The generating unity power factor torques of BDFMs with the different pole pair combinations having different number of loops are illustrated in Figure 3.23(a), while the torque ripple produced in the BDFMs are illustrated in Figure 3.23(b).

For the p_1 = 2 and p_2 = 3 combination, the 72 stator slots models have a similar torque production and ripple pattern with the 36 slots models. However, the 72 slots models achieve considerably less torque ripple than the 36 slots models.

The p_1 =2 and p_2 = 4 pole pair combination achieve greater torque than the p_1 = 2 and p_2 = 3 combination, which is expected as they have lower speeds for the same power rating. However, the p_1 = 2 and p_2 = 4 models have considerably higher torque ripple than their p_1 = 2 and p_2 = 3 counterparts. The p_1 = 2 and p_2 = 4 BDFM with an NL rotor has spikes in torque ripple for every loops per nest number which is a multiple of three also. For both pole pair combinations, the BDFMs with the cage+NL rotors also have the highest torque.

The illustrated increase of rotor loops and consequent effects indicate a relatively greater flexibility with BDFM rotor design as compared to DFIG rotors which have very specific numbers of slots based on the DFIG PW poles. Also considering the natural speeds of the two pole pair

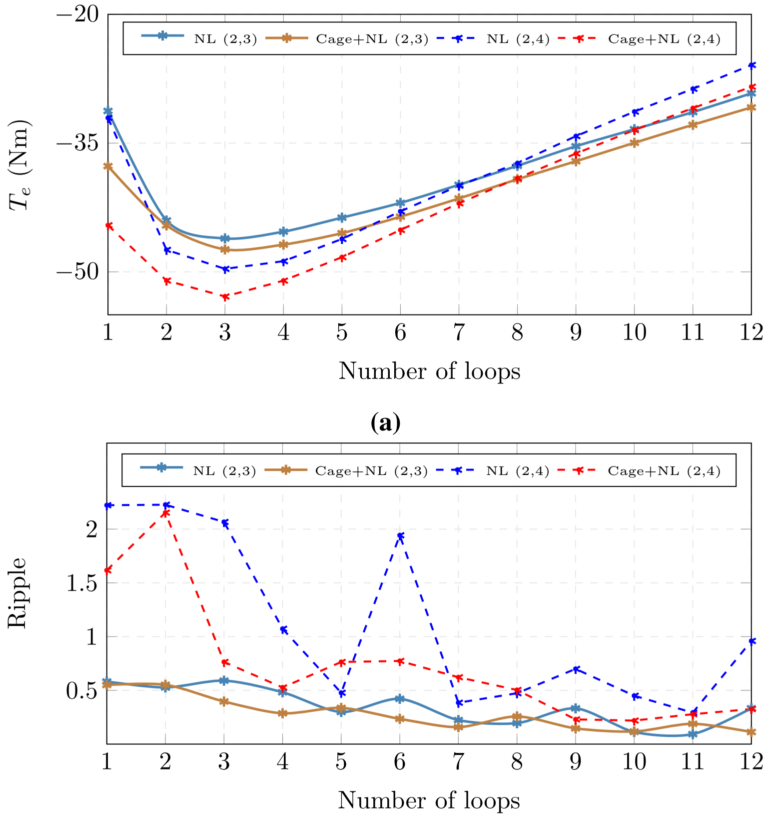

(a)

(b)

Figure 3.23: *Effect of rotor loops in BDFMs with 72 stator slots on (a) Torque (b) Torque ripple.*

combinations used, higher stator slot numbers would have been required for DFIGs based on the number of poles required for the desired speeds.

3.4 Summary

CC models of BDFMs with NL and cage+NL rotors have been developed using the WFT, and the processes involved in the synchronous doubly fed mode have been illustrated. A revision of magnetizing inductance calculations using the WFT was given. The CC models mean torques at different load angles closely matched the FEA models mean torques. The CC models were also used to provide insight on the difference in torque magnitude and ripple between the BDFMs with NL and cage+NL rotors. Insight about the rotor currents in the NL and cage+NL rotors were also presented.

Chapter 4

Power output evaluation of BDFM designs

In this chapter, it is illustrated how evaluating BDFM designs without proper mode and power factor considerations can lead to inaccurate performance estimations. Since BDFMs are considered as alternatives to DFIGs, a comparison of different DFIG topologies is first reviewed, after which BDFM designs are examined. Finite element analysis (FEA) models of the selected machines (DFIGs and BDFMs) are simulated as grid connected machines in the synchronous mode.

Significant variations of power output with grid side power factor of these machines are highlighted, denoting the need for more nuanced evaluation of the power density of these machines, especially when considering grid code requirements. Parts of this chapter are from the presented conference paper of Olubamiwa and Gule (2020) [88].

4.1 Introduction

Typical DFIG design methodologies are derivatives of the Squirrel Cage Induction Machine (SCIM) design methodologies. Similar sizing and winding parameter equations are used for SCIMs and DFIGs, as seen in for SCIMs and wound rotor IMs in [16]; for wound rotor induction generators and/or DFIGs in [15]. Influences of [15, 16] are seen in DFIG design literature like [89–92]. However, SCIMs are predominantly used as motors, for which torque and efficiency are paramount for performance evaluations. The power factor of SCIMs is not controlled, and they absorb reactive power from the grid. In typical performance data of manufactured SCIMs, there are performance evaluations at full load, three quarter load and half load conditions. Some manufacturers further list the power factors at these loads like in [93], with the power factor being highest at full load.

Asynchronous (in SCIMs) and synchronous (in DFIGs) operations are significantly different. Although the power factor in DFIGs can be controlled, power output at the same excitation magnitudes varies for different power factors. Wind turbines are typically required by grid codes to generate power within 0.95 lagging to 0.95 leading power factor [87]. Constraining DFIGs to this power factor range can lead to derating, as rated torque values may occur outside the power factor limits at rated excitation. For wind turbine applications, BDFMs are operated in synchronous doubly fed modes similar to DFIGs. Consequently, similar issues regarding DFIG performance evaluations and grid code requirements apply to BDFMs.

Different evaluation parameters have been used for BDFMs in literature, and a few are outlined as follows. In [55], BDFMs with different pole pair combinations are compared in terms of their torque capabilities, efficiency and torque ripple. BDFMs are evaluated at their maximum torque operating points for the optimizations in [57, 58, 60]. For the optimization in [76], a constraint of 0.75 power factor is placed on the PW. However, this power factor is much lower than required in wind turbines. In [23], 3.2 MW BDFM based wind turbine drivetrains are compared with other drivetrains based on DFIGs and permanent magnet generators of the same power. Efficiency and cost were major factors in the comparisons. A BDFM design procedure which is derived from a simplified equivalent circuit, and useful for considering multiple design variables, is described in [47]. A BDFM is then designed for a 180 IM frame, and simulated with FEA to verify the design methodology. The FEA flux density at full generating load torque matches closely with expected design values.

In this chapter, a case is made for evaluating BDFM designs at the PW side unity power factor in the synchronous doubly fed generating mode. The performances in asynchronous and synchronous doubly fed modes of the DFIGs designed in [94] are initially compared. The differences between synchronous doubly fed motoring and generating performances are also illustrated. Since BDFMs operate similarly to DFIGs, it is reckoned appropriate, that the performances of DFIGs in synchronous doubly fed operations be first demonstrated. Details of the designs compared are provided in [94], and this is one of the reasons for their selection. Furthermore, since two DFIG topologies are compared, they are used to provide a framework for BDFM and DFIG comparisons.

Three BDFM designs at different power ratings with varied pole pair combinations, are used to illustrate the performances of BDFMs in synchronous doubly fed operations. The differences between doubly fed motoring and generating performances of BDFMs are also underscored. Measured results from a 160L frame 2/3 BDFM are used to validate the recommended design evaluation methodology.

Table 4.1: *Dimensions and specifications of Machines 1 & 2*

Parameters	**Machines**	
	1	**2**
Topology	Conv. DFIG	RDFIG
Stator slots	36	24
Rotor slots	24	36
Grid phase voltage (V)	127	
Grid frequency (Hz)	60	
Primary current (A)	16.95	
Control current (A)	73.8	
Stack length (mm)	116	
Inner stator diameter (mm)	136	136.6
Outer stator diameter (mm)	222	197
Shaft diameter (mm)	75	54
Stator turns per slot	14	4
Rotor turns per slot	4	14

4.2 DFIG topology design evaluation

The stator/power windings of conventional DFIGs are connected directly to the grid, and the rotor/control windings are connected to power converters. A novel DFIG topology is presented in [94, 95], with the DFIG rotor windings connected directly to the grid as the power winding (PW), and the stator windings are connected to partially rated back-to-back power converters as the control winding (CW). It is proposed that this topology coined as the rotor-tied DFIG (RDFIG), can lead to improvements in efficiency and power density in comparison to conventional DFIGs.

In [94], a 5 kW conventional doubly fed induction machine (DFIM) called **Machine 1** in this chapter, and a 5 kW rotor-tied DFIM called **Machine 2** in this chapter, are compared in terms of their power density. The rated torques of both machines are similar, and therefore have similar power output. In spite of this, the rotor tied machine is shown to have a smaller mass and therefore higher power density. The rotor-tied machines also has a higher efficiency. However, these machines were simulated and experimentally evaluated in the asynchronous in the motoring operating mode (with short-circuited CWs). The authors do not evaluate the power factor of either machine.

4.2.1 DFIG simulations

The dimensions and specifications of **Machines 1 & 2** are given in Table 4.1. **Machines 1 & 2** have identical number of turns for their PWs and CWs respectively, and are both rated as 5

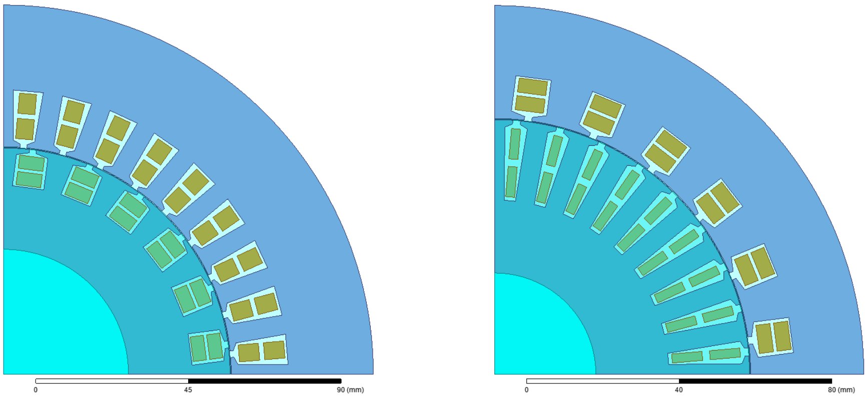

(a) **(b)**

Figure 4.1: *Simulated DFIG FEA models (a)* ***Machine 1*** *(DFIG), (b)* ***Machine 2*** *(RDFIG).*

kW machines. For the simulations in this chapter, the slot dimensions are based on conductor information given in [94]. Also, a fill factor of 0.4 is chosen to the round wires used in the PWs of the DFIGs, while 0.7 fill factor is used for the CW square conductors.

The FEA models of both machines are developed in ANSYS EDT ®, and are illustrated in Figure 4.1. For asynchronous tests, the CWs are shortcircuited, while (rated grid) voltage excitations are applied to the PWs. The load torque of 26.526 Nm and moments of inertia given in [94], are applied to both machine models. Changing the polarity of the load torque enables switching between asynchronous motoring and generating modes.

For synchronous mode simulations, the PWs are excited with voltage excitations at the grid voltage and frequency, while the CWs are excited with current excitations at ”load angles” relative to the grid voltage (PW voltage). It should be noted that for RDFIGs, the direction of rotation is in reverse compared to conventional DFIGs [96]. The two machines are simulated using the M400-50A steel lamination.

The simulation results considered are the torque developed in the machines, output power, power factor, and efficiency. ANSYS EDT® provides the transient electromagnetic torque (T_e) developed for each simulation, and an average over a time period at steady state is used. The calculations for the output power, power factor and efficiency of the machines are detailed in Appendix A [1].

A parametric analysis is run for each machine at rated CW excitation and varying CW current load angles. The parametric variations of the load angles are conducted to investigate the machine performances in motoring and generating modes. A maximum slip of -0.35 is used for both DFIGs.

---

[1] The method of power factor and efficiency calculations in [88] was modified in this dissertation for accuracy.

Table 4.2: *Asynchronous mode performances of Machines 1 & 2*

Parameters		Motoring [97]	Motoring	Generating
Conv. DFIG	Power factor	-	0.795	0.69
	Speed (rpm)	1760.4	1735.8	1858
	Output power (kW)	4.89	4.8	-4.58
	Torque (Nm)	26.52	26.42	-26.46
	Efficiency (%)	92.26	89.8	89
Rotor-tied DFIG	Power factor	-	0.885	0.83
	Speed (rpm)	1752.42	1735.5	1856
	Torque (Nm)	26.54	26.42	-26.54
	Output power (kW)	4.87	4.8	-4.72
	Efficiency (%)	92.51	91.1	91.4

4.2.2 DFIG Simulation results

FEA results of the machines at selected asynchronous motoring and generating operating points are presented in Table 4.2. The motoring results given in [97] are also listed in Table 4.2. The power output from FEA simulations are similar to those given in [97], however slightly lower efficiencies compared to values in [97] are obtained. The power factor of the RDFIG is higher than that of the conventional DFIG at both motoring and generating operating points. Also, the power factors of both machines are higher in the motoring mode compared to the generating mode. Furthermore, the efficiencies of the RDFIG are higher than that of the conventional DFIGs at all operating points, as implied in [97].

The torque (T_e) developed and power factors for synchronous doubly fed operations, at varying CW current load angles, are illustrated in Figures 4.2 and 4.3 for **Machines 1 & 2** respectively. The positive torque region represents operations in the motoring mode, while the negative torque regions represent generating operations. The light blue and blue dots are the maximum torques and torques at PW side unity power factor respectively for motoring operations, while the brown and red dots are the maximum torques and torques at PW side unity power factor respectively for generating operations. The light blue and blue triangles are the power factors at maximum torque and PW side unity power factor points respectively for motoring operations, while the brown and red triangles are the power factors at maximum torque and PW side unity power factor points respectively for generating operations.

Results at selected doubly fed motoring operating points of **Machines 1 & 2** are given in Table 4.3, while results at selected doubly fed generating operating points are given in Table 4.4. It can be observed for both machines, that the discrepancy between the maximum torque and unity power factor points, is smaller for motoring operations than for generating operations.

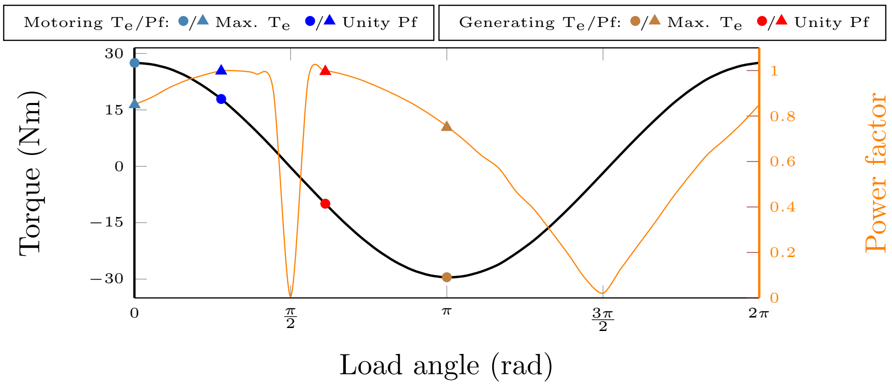

Figure 4.2: *FEA model torque and power factor of* ***Machine 1*** *(DFIG in [94]) at different load angles.*

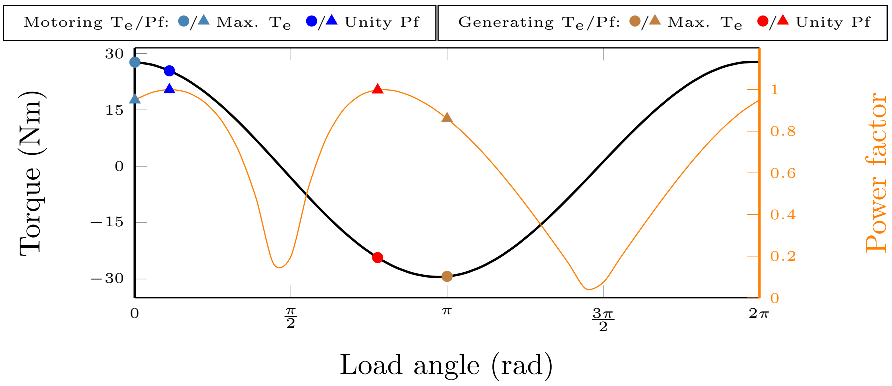

Figure 4.3: *FEA model torque and power factor of* ***Machine 2*** *(RDFIG in [94]) at different load angles.*

Table 4.3: *Synchronous motoring mode performances of Machines 1 & 2*

Parameters		Unity Pf	Max Torque
Conv. DFIG	Power factor	0.998	0.85
	Speed (rpm)	2430	2430
	Output power (kW)	4.56	7
	Torque (Nm)	17.9	27.5
	Efficiency (%)	94.2	94.2
Rotor-tied DFIG	Power factor	0.999	0.95
	Speed (rpm)	2430	2430
	Torque (Nm)	23.59	27.75
	Output power (kW)	6.47	7.06
	Efficiency (%)	95.4	95.1

Table 4.4: *Generating performance of Machines 1 & 2*

Parameters		Unity Pf	Max Torque
Conv. DFIG	Power factor	0.996	0.76
	Speed (rpm)	2430	2430
	Torque (Nm)	-9.95	-29.5
	Output power (kW)	-2.29	-7
	Efficiency (%)	90.3	93.4
Rotor-tied DFIG	Power factor	0.998	0.92
	Speed (rpm)	2430	2430
	Torque (Nm)	-24.3	-29.3
	Output power (kW)	-5.88	-7.09
	Efficiency (%)	95.1	94.8

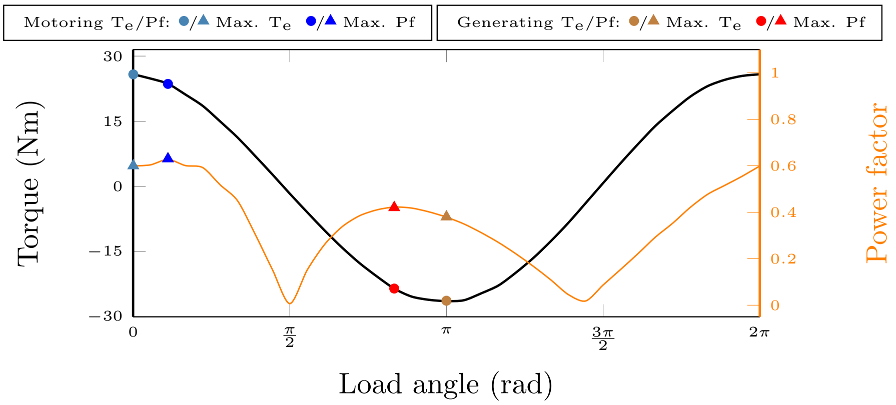

Figure 4.4: *FEA model torque and power factor of optimized* ***Machine 2*** *(RDFIG in [97]) at different load angles.*

Similar to the asynchronous operation results, the power factors for both machines at peak motoring torque are higher than at peak generating torque. The efficiencies at the selected motoring points are also higher than the corresponding generating points. **Machine 2** (RDFIG) has higher efficiency than **Machine 1** (conventional DFIG) at all the selected operating points.

Solely based on **Machines 1 & 2**, RDFIGs appear to be a significantly better performing topology compared to conventional DFIGs. This is seemingly bolstered with considerations of power factor. However, this may not necessarily be the case, as if the slot dimensions given in [97] are used, **Machine 2's** performance is significantly degraded.

In [97], a shape optimization to increase the power density of **Machine 2** is implemented. For the FEA simulations in [97], the RDFIG PW's are connected to a 3-phase diode bridge, with a

Table 4.5: *BDFM design dimensions and specifications*

Parameters	Symbol	Unit	Machine 3	Machine 4	Machine 5
Grid frequency	F	Hz	50		
Base power	P_t	kW	5.5	75	250
PW pole pairs	p_1	-	2		4
CW pole pairs	p_2	-	3	4	6
Rated slip	-	-	0.35	0.36	0.5
Grid phase voltage	V_1	V	230	400	690
Airgap flux density	B_{sum}	T	0.57	0.9	0.7
Electric loading	$\bar{J}$	kA/m	29	30.2	46
Stack aspect ratio	λ	-	1.2	1.1	1.5
Stack length	L	mm	192	374	801
Inner stator diameter	D_{si}	mm	161	340	534
Outer stator diameter	D_{so}	mm	272	550	697
Stator slots	n_s	-	36	72	72
PW turns per slot	N_{s_1}	-	46	7	8
CW turns per slot	N_{s_2}	-	69	17	25

load resistor and capacitor. The torque per weight of the optimized design is about 4.2% more than **Machine 2**.

The synchronous doubly fed torque at varying CW current load angle of the optimized design of **Machine 2** in [97], is illustrated in Figure 4.4. The peak torque at doubly fed generating operations is reduced for the optimized design. Also, the efficiencies and power factors at different CW current load angles are severely compromised. Therefore, the optimized design is less suitable for wind turbine operations. This is less apparent based on the design evaluation method employed in [97], but is obvious when the design is simulated for doubly fed operations with PW side power factors considerations.

4.2.3 BDFM design evaluation

Three different BDFM designs (**Machines 3, 4 & 5** in this chapter) are used to illustrate the performances of BDFMs operating in the synchronous doubly fed mode. Details of these machines are given in Table 4.5. Power ratings of 5.5, 75 and 250 kW are considered. Also, three different pole pair combinations (2/3, 2/4, 4/6) are used. These designs are also simulated at varying CW current load angles at stated rated slip and CW excitation values.

Relatively moderate B_{sum} values are used for the 5.5 and 250 kW designs, while a high value is used for the 75 kW design. The $\bar{J}$ values of the 5.5 and 250 kW designs are relatively

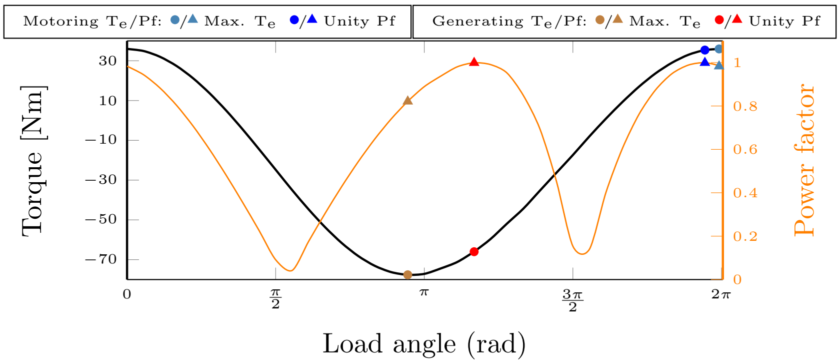

Figure 4.5: *FEA model torque and power factor at different load angles of 5.5 kW BDFM*

Table 4.6: *Generating performance of Machine 3*

Parameters	Symbol	Unity Pf	Max Torque
Torque	Nm	-66	-77.6
Power factor	-	0.999	0.82
Total Power (P_t)	kW	4.75	5.49
Efficiency	%	84.8	83.4

high, while that of the 75 kW design is moderate. These (high) values are used to briefly demonstrate their impact on BDFM performances. Further investigations into suitable electric and magnetic loadings across different power ratings are conducted in chapter 6.

The torques and power factors at different CW current load angles of **Machine 3** is illustrated in Figure 4.5, while the doubly fed generating performances at unity power factor and peak torque are detailed Table 4.6. The torques and power factors at different load angles are illustrated for **Machine 4** in Figure 4.6, with generating details given in Table 4.7; Figure 4.7 and Table 4.8 are for **Machine 5**. The plot markers used for the DFIG plots are identical for the BDFM plots.

Similar to the DFIGs, the 3 BDFM peak torques are closer to their torques at unity power factor in the motoring mode, than in the generating mode. The peak generating torques of all 3 BDFMs occur at power factors outside typical grid code regulations. The efficiencies of the machines at peak torque and unity power factor also vary, with the efficiencies at unity power factor being slightly higher.

As expected, the BDFM designs with lower power factors at their peak torques had greater reduction in torque/power at unity power factor. The power generated at unity power factor is about 86.5 % of the peak power for **Machine 3**, 74.5 % for **Machine 4**, and 89.3 % for **Machine 5**.

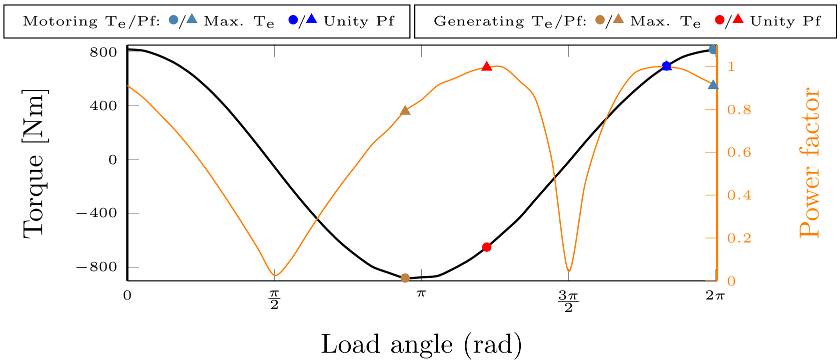

Figure 4.6: *FEA model torque and power factor at different load angles of 75 kW BDFM*

Table 4.7: *Generating performance of Machine 4*

Parameters	Symbol	Unity Pf	Max Torque
Torque	Nm	-649	-879
Power factor	-	0.996	0.79
Total Power (P_t)	kW	47.3	63.5
Efficiency	%	92.9	92

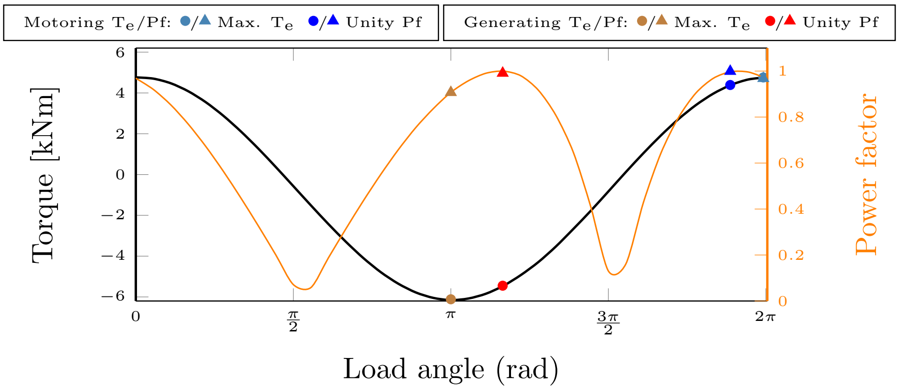

Figure 4.7: *FEA model torque and power factor at different load angles of 250 kW BDFM*

Table 4.8: *Generating performance of Machine 5*

Parameters	Symbol	Unity Pf	Max Torque
Torque	kNm	-5.45	-6.16
Power factor	-	0.999	0.91
Total Power (P_t)	kW	211.6	237
Efficiency	%	90.8	90

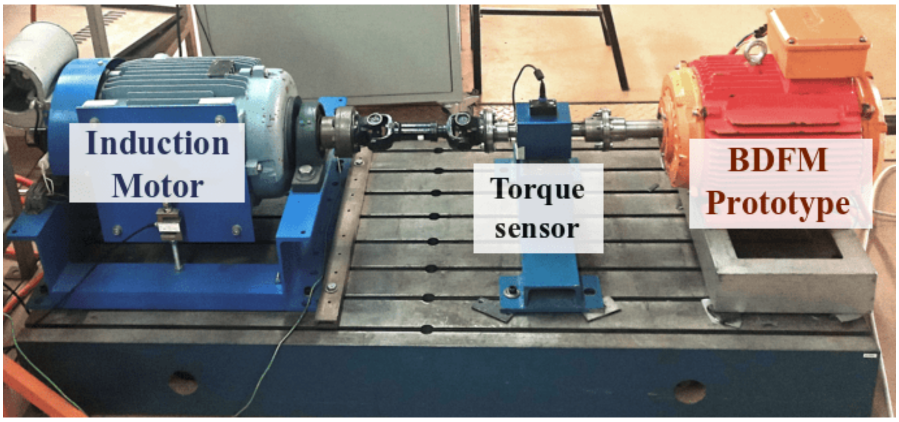

Figure 4.8: *160L frame BDFM test setup*

Machine 3 is a small BDFM, and the efficiency at such power ratings is typically low. This is however compounded by the relatively high electric loading. The peak generating power of **Machine 4** is far off the 75 kW target, and the design has the widest percentage difference between the peak generating torque and torque at unity power factor. The magnetic loading of **Machine 4** is relatively high, and this is a significant factor for the low torque at unity power factor. The electric loading of **Machine 4** is moderate, thus its efficiency is higher than **Machine 5**. It is also worth noting that the high aspect ratio and electric loading are jointly responsible for the low efficiency of **Machine 5**.

4.3 Experimental measurements

A 2/3 BDFM prototype built for a 160L induction machine frame is tested at different operating regions. Details of the prototype construction and test setup (shown in Figure 4.8) are given in Appendix C. The prototype is rated 4.5 kW at PW side unity power factor for -0.35 slip. Based on FEA simulations, the maximum PW power attained at rated CW excitation, is about 3.2 kW.

Running tests similar to earlier FEA simulations where the ”load angle” is varied is not practical, as physically unstable regions are also simulated [12, 98]. Also, control systems are not necessarily designed to work that way. As a result, the tests are carried out in the synchronous doubly fed generating mode at selected power levels and power factors. Furthermore, the tests are conducted at the prototype natural speed of 600 rpm.

A vector control approach using cascaded PI controllers is employed. CW current control is initialized in the first cascade, from which the PW current control is achieved in the next cascade. From the PW current control, a cascade for power control is derived allowing for the power factor control to be performed. Further details are given in Appendix C.2.

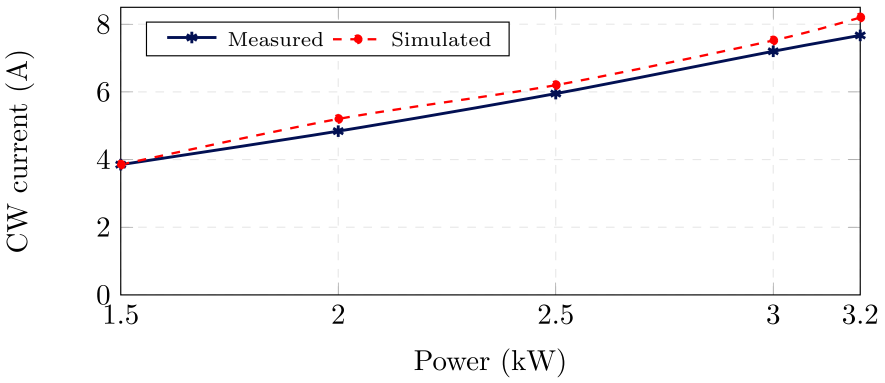

Figure 4.9: *Measured and FEA CW currents for different power levels at unity power factor*

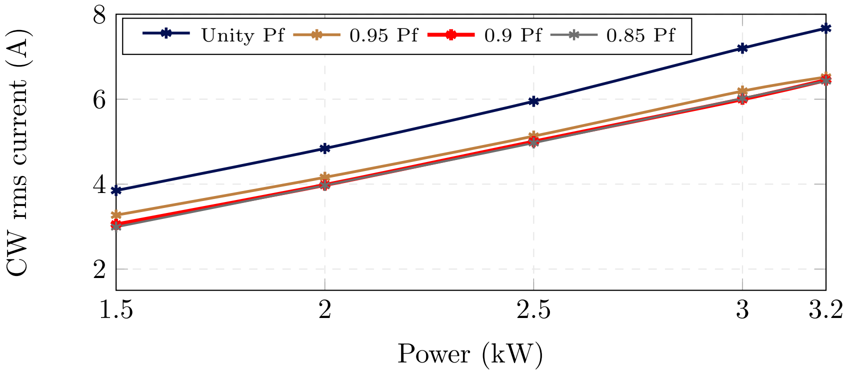

Figure 4.10: *Measured CW currents for different power levels and power factors*

The prototype is tested at 5 different power levels from 1.5 - 3.2 kW. The measured CW currents, and the simulated FEA currents, at unity power factor for these different power levels, are illustrated in Figure 4.9. As observed, the FEA and measured CW currents are similar at the different power levels. As expected, higher power requires higher CW excitation.

Testing at different power levels/power factor is also conducted, and the measured CW currents at these power levels/power factors are shown in Figure 4.10. It can be observed that the CW currents are significantly higher for unity power factor, signifying the higher demand in excitation to achieve unity power factor.

The FEA and measured efficiency of the tests conducted at unity power factor are illustrated in Figure 4.11. For both measured and FEA tests, the efficiency is lower at higher powers, contrasting with asynchronous motoring efficiencies which are higher at full load. There is a noticeable difference in the measured and FEA efficiencies for all power levels. There are a number of factors that are responsible for this. Mechanical losses are not accounted for in the FEA simulations, and these are significant due to vibrations in the prototype, which increase with loading. Also, the PWM currents from the power converters cause additional losses due to their harmonics, and these are not accounted for in the FEA simulations.

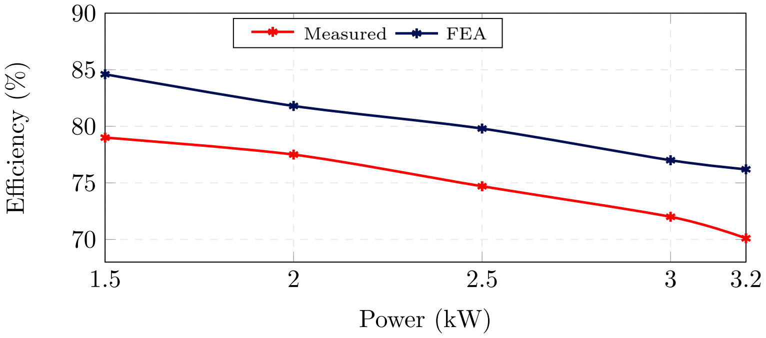

Figure 4.11: *Measured and FEA prototype efficiency for different power levels at unity power factor*

4.4 Discussion on BDFM power evaluation

Doubly fed machines have been shown to yield different performances for (singly fed) asynchronous and (doubly fed) synchronous operations. Performances of BDFMs in the synchronous doubly fed motoring and generating modes have also been shown to differ significantly. The differences between the peak torque, and the torque at unity power factor, are not identical for operations in the doubly fed motoring and generating modes. Furthermore, for synchronous doubly fed generating operations, BDFM peak torque based on rated CW current often occurs outside of operable wind turbine grid code power factor requirements.

Simulating BDFMs in synchronous doubly fed modes to illustrate the torque at varying CW current load angles is not necessarily unique to this paper. Different illustrations of the changes in torque at varying ”load angles” are seen in [10, 98, 99] for BDFMs, and [40] for synchronous operations of cascade machines. Stable and unstable operating torque regions in BDFMs are also illustrated in [98]. What is unique in this paper, is the illustration of the change in power factor at varying CW current load angles. Also, to the authors' knowledge, the use of voltage excitation for the PW of BDFMs in simulations is uncommon [2].

The rationale behind using a voltage excitation for the PW is to get a more accurate estimate of the machine performance, based on a given CW excitation. Using a rated PW current excitation somewhat assumes that the PW current remains constant, despite the changing power factor. However, in reality, the PW current changes with power factor, and higher CW excitation would be required to keep the current constant at higher power factors.

The experimental measurements have demonstrated that running a BDFM at unity power factor, requires significantly higher excitation than running at even 0.95 lagging power factor for the same active power output. The peak torque power factor of a design at rated CW current can be considerably lower than operable values in wind turbines. Such under-performing designs would require additional/over-excitation to achieve unity power factor at desired power

---

[2] The author uses a similar style of PW excitation in [63]

ratings. Increased excitation would have significant implications on converter ratings and overall system cost. Considering that such under-performing designs may be significantly saturated [45], more losses would be incurred from additional excitation. The losses and additional cost of excitation can at times be disproportionate to the power being generated.

Peak torque and accompanying power factor may have poor correlation with torques at operable power factors. Also, the variations in torque and efficiency with respect to power factor can vary wildly with each design. Therefore, a conclusive relationship between the peak torque and the torque at another power factor is difficult to determine, similar for efficiency. To a large extent, the combination of input variables such as flux densities, aspect ratios, and electric loadings, determine BDFM output parameter values. These output parameters have correlations, but deviations are not uncommon. Therefore, specific and detailed output parameters of BDFMs are required for reliable and practical BDFM design evaluation.

In [45], BDFM converter ratings optimization are discussed to avoid derating, while achieving grid (power factor) requirements for wind turbines. It should be noted that derating would be higher if the power factor at the rated generating torque is farther away from the unity power factor. It is also highlighted in [45], that the most demanding operating condition of a BDFM occurs when generating at rated real power while supplying reactive power to the grid (0.95 leading power factor). This leading power factor point is used as the optimization point for the converters. In [49], it is noted that the 250 kW BDFM tested in [45] required significant over-excitation to operate within grid code requirements. The rotor leakage is identified as a significant factor contributing to the need for over-excitation.

4.5 Conclusion

Considering previous sections, [45] and [49], a solid argument can be made for evaluating BDFM designs at the doubly fed generating mode with power factor considerations. This is to give an accurate context of performance. Simulating BDFMs at specific leading power factor values as suggested in [45] is a little more complicated than at unity power factor. Over-excitation will be needed for more designs to achieve 0.95 leading power factor than unity power factor. Unity power factor is also at the mid-point of operable power factor conditions in wind turbines, it is therefore proposed that BDFMs be simulated at PW side unity power factor for design and comparison purposes.

It is worth noting that power factor considerations are also not common for DFIG design evaluation in literature. However, DFIGs are less prone to the effects of saturation, and have lower leakages compared to BDFMs [52], thus more attention is needed in evaluating BDFM designs. It is also proposed that power density comparisons between BDFM and DFIG designs be conducted at the stipulated conditions.

Chapter 5

A design and optimization approach for BDFMs

In this chapter, a methodical approach to the BDFM design is presented. A way to select suitable rotor topology per application is discussed. Insights on the BDFM design optimization with regards to power density and efficiency are given. Also, an optimized design for the 160L frame BDFM prototype used in this study is discussed. Parts of this chapter are based on the presented conference paper of Olubamiwa and Gule (2020) [100].

5.1 Introduction

A detailed BDFM design process is presented in section 5.2 of this chapter. A simplified calculation of the BDFM D^2l design coefficient is presented with the geometric and winding design. In section 2.3.2, it was noted that the NL and cage+NL rotors are the preferred BDFM rotors, and these are the rotors considered for the design process. It is illustrated how the decision between NL and cage+NL rotors may sometimes transcend the disparity between p_1 and p_2 criteria as suggested in [19]. As a result, a case by case approach is advocated for rotor selection. The CC models discussed in chapter 3 are used to rapidly determine a suitable (NL or cage+NL) rotor topology based on the BDFM torque output and torque ripple.

There is a lack of information about specific values of the stack length ratio, electric loading and airgap flux density to use in BDFM designs. As such, the selection of suitable values for improved power density and efficiency using an optimization process, is illustrated. A variant of the non-dominated sorting genetic algorithm (NSGA-II) is used with a response surface approximation (RSA) for the optimization process. The RSA is developed from FEA evaluations of design samples.

A 5.5 kW BDFM design using the proposed process is first presented in section 5.3. In the design process, the thought process behind the selection of a suitable rotor topology is discussed. An optimization process to maximize the power density and efficiency of the 5.5 kW BDFM is also implemented.

In the course of this study, a BDFM prototype was constructed. The design of this prototype was partially based on the results in [100]. An empty 160L IM frame was used for the prototype, which placed restrictions on the volume and length. Also, at the time of construction, there was also only one copper bar size available for purchase at the current ratings required. Machining down bigger sized bars into custom sizes proved costly. All these restrictions necessitated fixed values for the outer stator diameter, machine stack length and rotor slot sizes. The closest values to the optimal input variables in [100], for which the frame requirements could be met, were chosen for the prototype.

The design process presented in this chapter has since been further developed from what was presented in [100]. Consequently, an alternative optimized BDFM design for a 160L frame, estimated around 5.5 kW with similar design restrictions, is investigated in section 5.4. It is recognized that the 5.5 kW power rating used for both design examples in this chapter, is much smaller than the power ratings required for typical wind turbine applications. However, a MW rated machine is impractical and too costly at this stage. It also is reckoned that key points of the design process presented are relevant for much bigger machines, and this is illustrated in chapter 6.

5.2 Proposed BDFM design

The proposed BDFM design process is comprised of two intertwined processes: the geometric and winding design process, and the power density optimization process. The geometric and winding design process is used for each design iteration in the optimization process. On the other hand, given the absence of specific values for the stack aspect ratio, electric and magnetic loadings in literature, practical values can be identified during an optimization process, and these values are used in the final geometric and winding design of the BDFM. These two processes are further discussed in the subsequent subsections. In cases where the necessary primary input variables are already determined, other parameters can be fine tuned with the optimization process. The determination of a suitable rotor topology is also discussed.

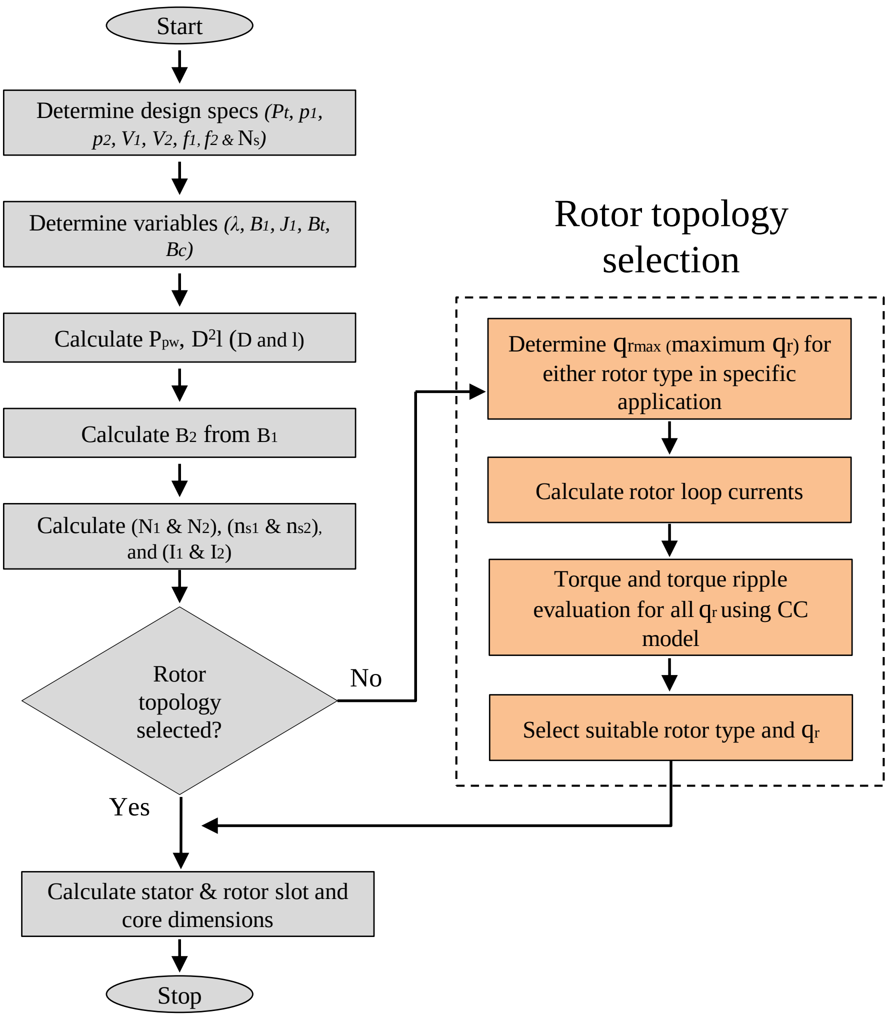

Figure 5.1: *Geometric and winding design process.*

5.2.1 BDFM geometric and winding design

The generalized BDFM geometric and winding design process is summarized in Figure 5.1. The process represents the steps that are taken during every design iteration. The output coefficient (D^2l) is first calculated, then stator winding parameters are obtained. The rotor topology is then determined[1], after which the slot and core dimensions are calculated.

The D^2l calculations, stator winding parameters and the rotor topology determination are further discussed in the following subsections. The stator slot dimension calculations are given in Appendix B.3. Considering NL and cage+NL rotors, the rotor bars used have rectangular

---

[1] ”Determination” here refers to either using already decided rotor design/topology or executing the rotor design process.

shapes, which generally determine the rotor slot dimensions. The core depths are calculated with (B.3.8).

5.2.1.1 The output coefficient (D^2l) calculation

The design specifications such as the rated power ($\mathrm{P_t}$), PW pole pairs (p_1), CW pole pairs (p_2), desired rated mechanical speed (ω_m), grid voltage (V_1), grid frequency (f_1), maximum CW voltage and frequency (V_2 & f_2) are first delineated, and they largely remain constant. Values for the design variables stack length ratio (λ), PW flux density (B_1), PW electric loading (J_1), peak teeth and core flux densities (B_t & B_c) are then designated. These design specification and variables are combined to calculate the BDFM D^2l design coefficient using

$$D^2l = \frac{p_1 P_{pw}}{\pi^2 f_1 J_1 B_1}, \tag{5.2.1}$$

where, D is the mean airgap diameter, l is the stack length, P_{pw} is the maximum PW power. The derivation of this simplified D^2l calculation from the robust calculation in [47] is shown in Appendix B.1. The individual values of D and l are obtained using the stack length ratio (λ), which is given as

$$\lambda = \frac{l}{D}. \tag{5.2.2}$$

Determining values for B_1, J_1 & λ is discussed in section 5.2.2.

5.2.1.2 Stator winding parameters

With the PW flux density (B_1) already determined for the D^2l coefficient calculation, the CW flux density (B_2) can be calculated using (B.1.9). Using (B.2.4), the PW and CW number of turns per phase (N_1 & N_2 respectively) are calculated based on the rated voltages of these windings. The winding turns per stator slots (n_{s_1} & n_{s_2}) are then calculated from the number of turns per phase using (B.2.5). It should be noted that n_{s_1} & n_{s_2} are integers, so calculated N_1 & N_2 may need slight adjustments to ensure integer values for n_{s_1} & n_{s_2}. Also, if double layers are used for the windings, even numbers are needed for n_{s_1} & n_{s_2}. After n_{s_1} & n_{s_2} are calculated, the PW and CW currents (I_1 & I_2) can be derived using (B.2.6) & (B.2.7).

5.2.1.3 Rotor topology determination

The rotor determination process, as illustrated in Figure 5.1, is not necessarily an iterative process. Instead all possible topology options are considered, and the most suitable topology is selected. The NL and cage+NL rotors contain $p_1 + p_2$ nests, which typically contain more than one loop. As discussed in section 2.3.2, this is to allow for improved copper distribution in the rotor, and reduced space harmonics [10, 47]. The number of rotor slots in an NL rotor ($N_{r_{nl}}$) is calculated as

$$N_{r_{nl}} = 2q_r(p_1 + p_2), \tag{5.2.3}$$

where, q_r is the number of rotor loops in a nest. Meanwhile, the number of rotor slots in a cage+NL rotor ($N_{r_{cg}}$) is calculated as

$$N_{r_{cg}} = (p_1 + p_2)(2q_r - 1). \tag{5.2.4}$$

Final/optimized values of N_s, D, l, N_1 & N_2 are not necessary for the rotor parameter determination, as baseline values are adequate to determine a suitable rotor topology. Final values of p_1 and p_2 are however necessary for the rotor design process, while only significant changes to $\mathrm{P_t}$ require a new rotor design. Higher power ratings lead to bigger machines, which can accommodate more rotor loops per nest (q_r).

A practical maximum number of loops in a nest ($q_{r_{max}}$) is initially determined with regards to mechanical constraints and saturation concerns. The BDFM CC model presented in chapter 3 is used to evaluate the torque (T_e) and torque ripple produced. All $q_r \leq q_{r_{max}}$ for either rotor type are evaluated. Using FEA at this stage can be time wasting, and the CC model enables a rapid determination of T_e and torque ripple with all the changes to the rotor topology. The most suitable rotor topology in terms of high torque and low ripple is then selected. These factors are used because they are indicative of the machine power density and harmonic content [2].

Since the rotor topology remains fixed after determination, the CC model is also used to determine the currents in the rotor bars/loops. It was illustrated in Figures 3.20 and 3.21, how the CC models closely estimate the rotor loop/bar currents compared to FEA models. These current values are used to calculate the conductor sizes in the rotors.

5.2.2 Design Optimization

The optimization process is used to maximize power density and efficiency. A flow chart of the process is illustrated in Figure 5.2. The primary input variables proposed for this optimization are the stack aspect ratio (λ), the PW flux density (B_1), and the PW electric loading (J_1). However, other variables such as the teeth and core flux densities (B_t & B_c), the CW maximum voltage (V_2), and geometric parameters like the stack length (l), stator inner diameter (D_{si}), slot widths etc., can be considered.

Although maximizing the power density is one of the objectives, the total power generated ($\mathrm{P_t}$) is also very important. $\mathrm{P_t}$ is used as a constraint, as designs can have high power densities, but their total power at unity power factor is considerably less than the desired $\mathrm{P_t}$. To identify the optimal $\mathrm{P_t}$ regions, different optimizations with $\mathrm{P_t}$ range constraints can be executed.

---

[2] Examples of rotor topologies selections are given in Appendix D

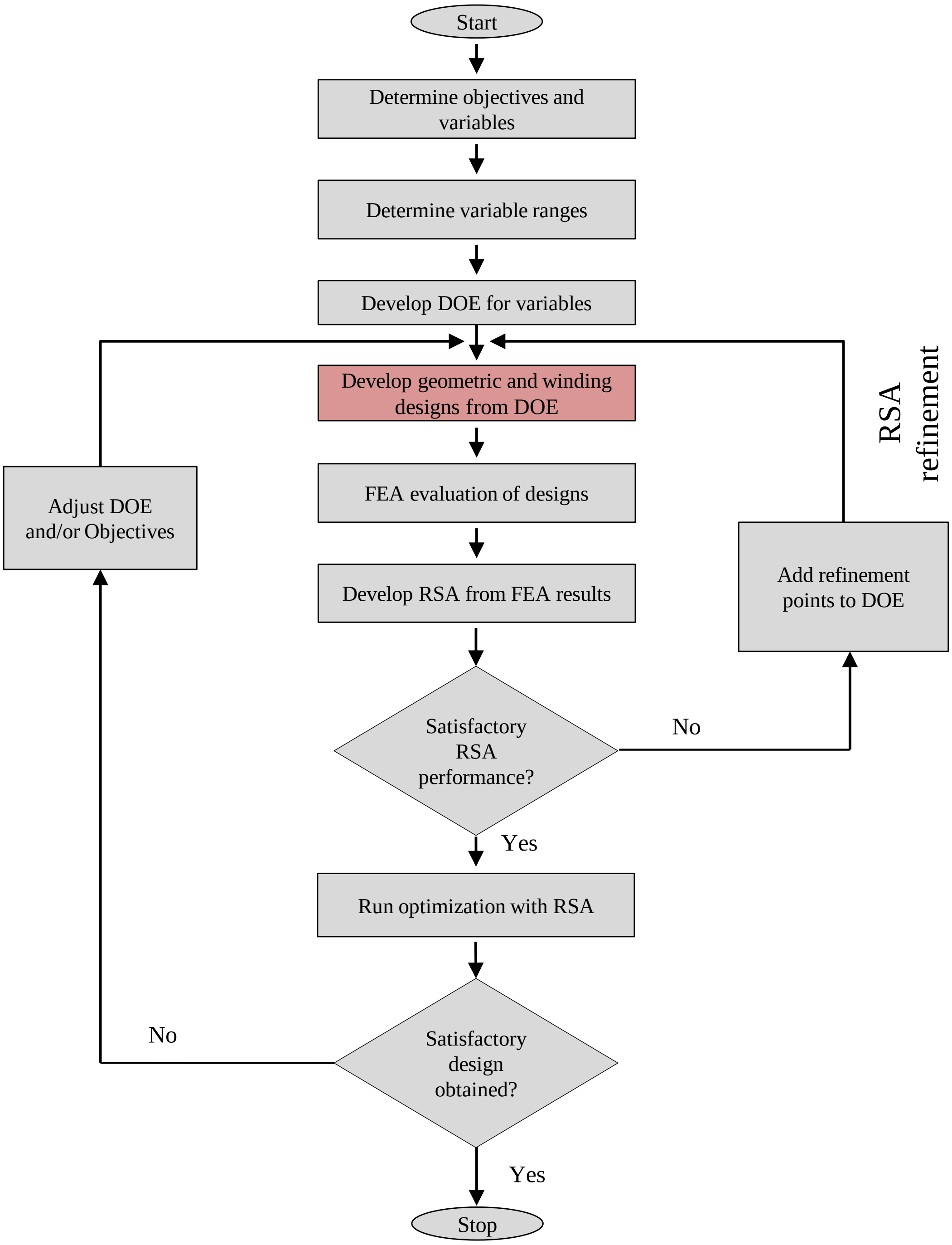

Figure 5.2: *Optimization process.*

A variant of the NSGA-II is used for optimization in this research. NSGA-II is a robust algorithm for multi-objective optimization, and it does not tend to converge in local optima. The optimal Pareto front provided by the NSGA-II also helps to make informed compromises between the multiple objectives. However, running an NSGA-II based optimization directly with time stepped FEA models takes a prohibitive amount of time. For this reason, a response surface approximation (RSA), developed from time stepped transient FEA simulations of design samples, is used alongside the NSGA-II.

The design of experiments (DOE) is conducted using the optimal Latin hypercube sampling (LHS) method, and the Kriging model is used to develop the RSA. Kriging is a commonly used RSA technique [101], and its usage in electrical machine design is seen in [97, 102, 103] to mention a few examples. There are other RSA techniques that can be used, some which are listed in [101]. However, the Kriging method is used here because of its high response quality and fitting of higher order variations of output parameters [104]. After the RSA is developed, an evaluation of the RSA response quality such as the goodness of fit is recommended. Kriging interpolates all the DOE points so the goodness of fit appears perfect if one is considering the DOE points. However verification points which are not included in the DOE can be used to test the RSA. If the RSA performance is unsatisfactory, more design points can be added to refine the RSA.

For this research, FEA of the BDFM design samples is conducted using ANSYS electronic desktop (ANSYS EDT), while the variable sampling (DOE), RSA development, and the NSGA-II optimization are executed using ANSYS Workbench. MATLAB is used to calculate machine geometric parameters based on the DOE samples provided from Workbench. Matlab is used due to the ease of data manipulation, and the geometric parameters of the designs developed from the DOE are stored in a file.

The PWs of the FEA models are excited by voltage excitations, while the CWs are excited by current excitations with a ”load angle” relative to the PW voltages. External circuits in ANSYS EDT are used for the rotor windings. The FEA is conducted at the rated maximum speed of the BDFM, with the $\mathrm{P_t}$ and efficiency calculated using equations in Appendix A.

A python script is used to manage the FEA simulations of the designs developed from the DOEs. With the python script, it is ensured that only FEA values at unity power factor are used. This is implemented by evaluating the power factor of each FEA run, and adjusting the load angle if the model output power is not at unity power factor. The reasons for testing at unity power factor conditions have been discussed extensively in chapter 4. The python script is also used to calculate the efficiency and power density of each design. Designs with considerable saturation may fail to achieve unity power factor at the rated excitation, and a penalty is attached to such designs at their highest power factor, such that they always have

Table 5.1: *Initial specifications of 5.5kW BDFM*

Parameters	Unit	Value
Grid phase voltage (V_1)	V	230
Grid frequency (f_1)	Hz	50
PW pole pair (p_1)	-	2
CW pole pair (p_2)	-	3
CW max frequency (f_2)	Hz	17.5
Stator slots number (N_s)	-	36
Stack length ratio (λ)	-	1.2
PW electric loading (J_1)	kA/m	13
PW airgap flux density (B_1)	T	0.255
Teeth flux density (B_t)	T	1.4
Core flux density (B_c)	T	1.5
Shaft diameter	mm	60

lower P_t, efficiency and power density than designs that can be run at unity power factor.

5.3 Design of a 5.5 kW BDFM

The described design and optimization processes are used to design a 5.5 kW BDFM. The specifications and initial variables used in the design of the 5.5 kW BDFM are listed in Table 5.1. Considering the selected pole pair combination, the first possible number of slots for full pitch windings is 36 slots. This number provides reasonable coil distribution for both stator windings. The next possible number is 72, which is not typical for 5.5 kW machines.

While suitable values for the electric and magnetic loadings for conventional induction machines are commonly outlined in available machine design literature, information about appropriate values for BDFMs is lacking. The initial choice of B_1 leads to a maximum airgap flux (B_{sum}) of 0.57 T. This conservative B_{sum} value is used because of the tendency of BDFMs to saturate more than other induction machines [12].

5.3.1 Rotor topology determination

The machine specifications in Table 5.1 are used for initial designs with NL and cage+NL rotors. For this design, $q_{r_{max}}$ would practically not be more than 4. Although higher q_r helps with better copper distribution and reduction of harmonics, q_r is generally lower for smaller machines due to rotor teeth saturation concerns. Also, N_r is typically close to N_s in available BDFM literature. However, for illustrative purposes, $q_{r_{max}}$ is taken to be 6.

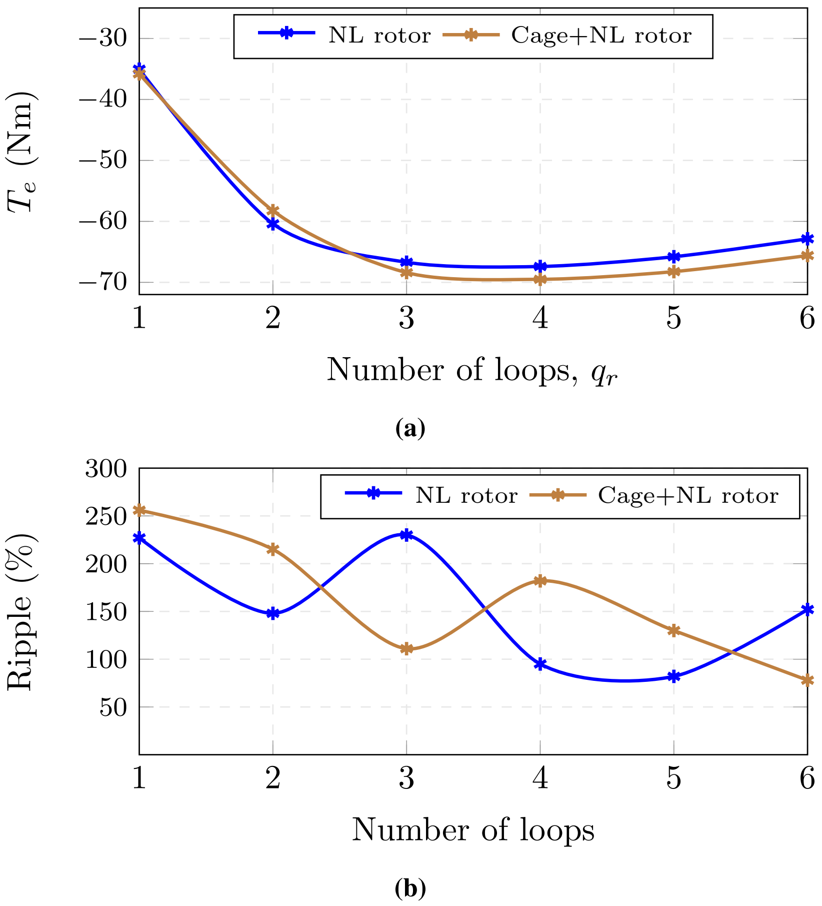

Figure 5.3: *(a) Generated torque for different rotor types with increasing loops, (b) Torque ripple for different rotor types with increasing loops.*

Using CC models, the mean generated torques at PW unity power factor for different q_r values for either rotor type are estimated and illustrated in Figure 5.3(a), while the evaluated torque ripples are illustrated in Figure 5.3(b). It should be noted that the CC model has a tendency to overestimate the torque ripple, however the response to changes in loop numbers is proportionally similar to FEA models as demonstrated in section 3.3.3.

The torque values for both rotor types in Figure 5.3(a) are similar, The generated torque is highest around $q_r = 3$ for both rotor types, with the cage+NL rotor having slightly larger torque. Furthermore, it can be observed from Figure 5.3(b), that the difference between the torque ripple of the NL rotor with $q_r = 4$ and the cage+NL rotor with $q_r = 3$ is not large. Also, the cage+NL rotor with $q_r = 3$ has a potentially simpler construction. Although the torque ripple produced by the selected rotor is still high for a practical BDFM, it is due to the harmonic rich nature of BDFMs, and can be reduced by skewing the rotor.

Table 5.2: *Initial and Pareto parameter ranges*

Variable		Unit	Initial DOE	Initial Paretos at P_t constraints (kW)		
				4.8 - 5.1	5 - 5.3	5.2 - 5.5
Input	λ	-	0.5 - 1.1	0.5 - 0.83	0.5 - 0.8	0.53 - 0.77
	B_1	T	0.13 - 0.33	0.246 - 0.33	0.26 - 0.32	0.26 - 0.3
	J_1	kA/m	8 - 15	8 - 14.4	8.1 - 13.1	8 - 12.8
Output	P_t	kW	2.34 - 5.68	4.8 - 5.1	5 - 5.27	5.2 - 5.32
	Ef	%	80.7 - 88.95	85.7 - 88.9	86.4 - 88.9	86.4 - 88.6
	PD	kW/m^3	231.7 - 524.9	381.2 - 521	388.7 - 520.2	396 - 520

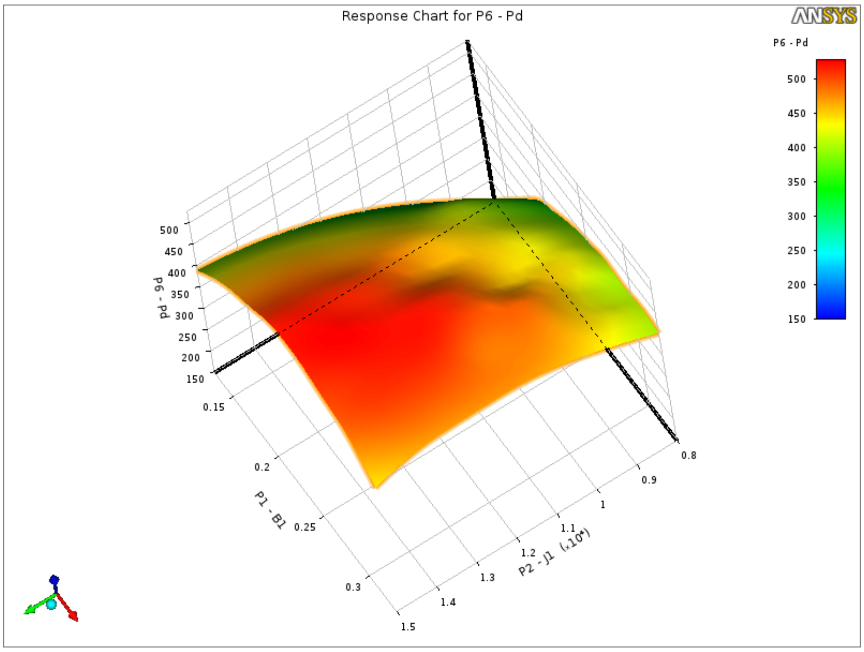

Figure 5.4: *Response surface plot.*

5.3.2 Optimization results

The RSA is developed from a DOE with 350 design points. The input and output parameter ranges of the design points are given in Table 5.2. It should be noted that the upper bounds of B_1 and J_1 in the DOE, lead to maximum airgap flux density (B_{sum}), and total electric loadings ($\bar{J}$) of 0.723 T and 26.7 kA/m respectively. An instance of the power density response to changes in B_1 and J_1 at an aspect ratio of 0.5, is illustrated in Figure 5.4.

20 extra design points are used as verification points for the RSA. The normalized predicted vs observed curve for these verification points is illustrated in Figure 5.5. As seen in the figure, the RSA predictions are close to the actual values. To give an idea of the deviation of predicted

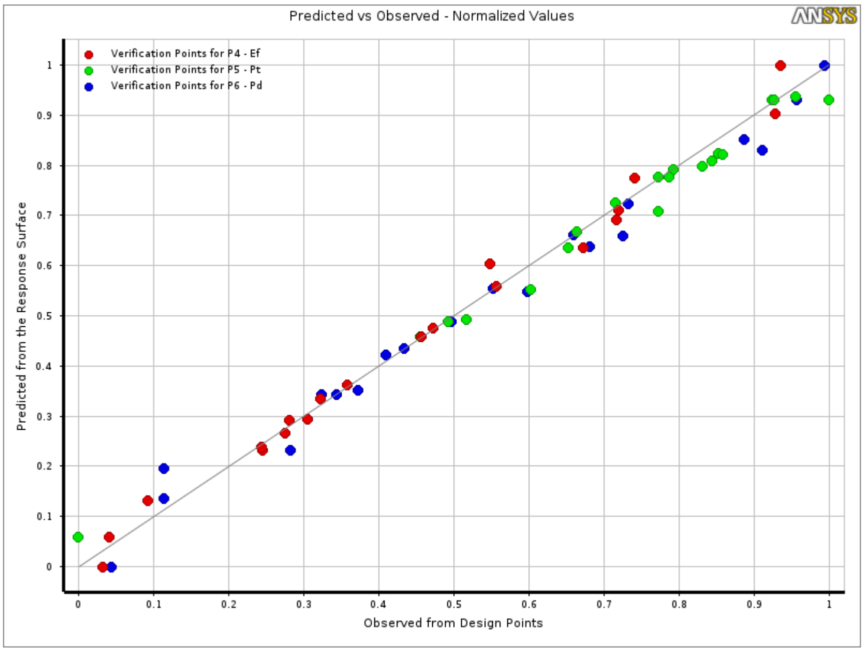

Figure 5.5: *Response surface plot.*

with respect to observed values, the top red dot (over the line) is from a design estimated by the RSA to produce 88.5 % efficiency, and it actually produces 88.3 %.

Considering the complete DOE in Table 5.2, the lower P_t bound in the DOE is far from the desired 5.5 kW rating [3]. Saturation, especially from the rotor teeth, is identified as the major factor for this. NL or cage+NL rotors have uneven current distributions, thus rotor teeth around the bigger loops are more susceptible to saturation. Also, smaller rotor diameters lead to narrower teeth, notably around the lower regions of the rotor slot. Saturation in these parts contribute significantly to the total machine saturation.

Optimizations are executed at 3 overlapping P_t constraint ranges; 4.8 - 5.1, 5 - 5.3, 5.2 - 5.5 kW. The overlapping ranges are used to contain the slight deviations from the RSA outputs, while 4.8 kW is selected to be the lowest acceptable P_t at unity power factor. The input and output parameter ranges of the Pareto fronts of these optimizations are also given in Table 5.2, and the Pareto fronts are illustrated in Figure 5.6. The input variables for the design points in the three Pareto fronts are similar, but a gradual narrowing of their ranges is observed with increasing P_t.

From the optimizations, the P_t bounds fall within a narrow B_1 range; the λ range is also narrowed for higher power. However, saturation influenced by the desired (5.5 kW) P_t, plays a part in the λ range for higher P_t. Higher desired P_t lead to generally bigger rotor diameters, which afford wider rotor slot teeth at higher λ values, and thus avoid saturation.

---

[3] P_t is obtained at generating PW unity power factor

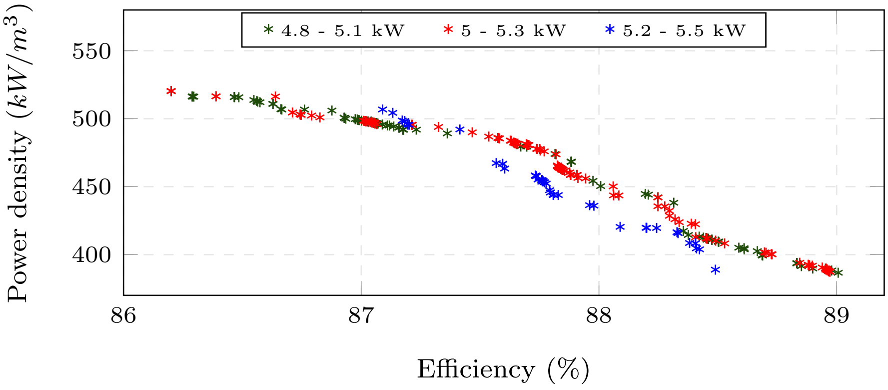

Figure 5.6: *Pareto fronts of optimizations with different* $\mathrm{P_t}$ *range constraints.*

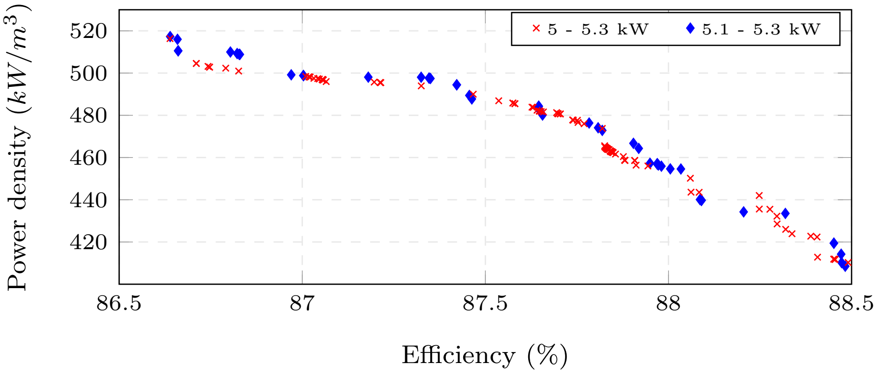

Figure 5.7: *Pareto front of optimization with 5.1 - 5.3 kW* $\mathrm{P_t}$ *constraint.*

Both saturation and electric loadings are factors for the efficiency of different designs. Saturation increases the core losses, also the magnetizing current is increased and less power is generated. Higher electric loading leads to more copper losses. Designs with high power density typically generate high $\mathrm{P_t}$ at unity power factor. How much the magnetic and electric loadings can be raised while avoiding saturation, determines the power density. The relationship between BDFM electric and magnetic loading is complicated [47], and this is where the optimization process comes in handy.

From Figure 5.6, there is not much difference in the curves of the first 2 Pareto fronts. Also, the actual $\mathrm{P_t}$ range from the 5.2 - 5.5 kW Pareto front is from 5.2 - 5.32 kW as indicated in Table 5.2. The 5.2 - 5.5 kW constraint is modified to 5.1 - 5.3 kW and the Pareto front from this optimization is compared with the 5 - 5.3 kW optimization in Figure 5.7. It can be observed that there is little difference between the two optimizations, thus 5.1 - 5.3 kW is identified as the optimal $\mathrm{P_t}$ range for the 5.5 kW design. Unless extreme power density or efficiency values are desired, a design point with efficiency between 87.5 - 88 % can be selected for the final design.

Table 5.3: *Details of initial designs*

Input Parameters	Unit	Optimal [100]	Prototype
B_1	T	0.245	0.23
J_1	kA/m	11.8	13
λ	-	0.6	1.2

Design parameters	Unit	Optimal [100]	Prototype
Inner stator diameter (D_{si})	mm	212	166
Stack length (l)	mm	127	200
Outer stator diameter (D_{so})	mm	303	260
Active volume	m^3	0.010214	0.010623

Output parameters	Unit	Optimal (FEA)	Prototype (FEA)
Efficiency (η)	%	86.4	86.5
Power ($\mathrm{P_t}$)	kW	5.4	4.7
Power density (PD)	kW/m^3	528	442

5.4 Optimization of a 160L frame BDFM

As stated in the introduction of this chapter, a BDFM prototype was constructed with modifications applied to the 5.5 kW BDFM designed in [100]. A comparison of the optimal design in [100], and the prototype design is given in Table 5.3. The input parameters of the optimal design in [100], were modified to the closest values that could produce a design fitting a 160L frame. Both designs have similar active volumes, but to compensate for the lower headroom constraint from the frame, the prototype design has a longer stack length.

The prototype design has a noticeable drop in $\mathrm{P_t}$, and the power density, and this is mostly linked to the value of λ used for the design. It should also be noted that the method of calculating the total power output and efficiency of BDFMs in this dissertation (as outlined in Appendix A) is different from that in [100]. The method of calculating the power output and efficiency in [100] is detailed in [88].

5.4.1 Optimization details

The fixed specifications of the 160L BDFM are listed in Table 5.4. With the same p_1/p_2 combination being used, the stator and rotor slot numbers are retained as in [100] and section 5.3. The cage+NL rotor is also the preferred rotor type. Based on the measurements of the 160L frame, the maximum stack length and outer stator diameter are chosen. As already stated

Table 5.4: *Fixed specifications of 160L frame BDFM*

Geometric Parameters	Unit	Value
Grid phase voltage (V_1)	V	230
Grid frequency (f_1)	Hz	50
PW pole pair (p_1)	-	2
CW pole pair (p_2)	-	3
Stator slots number (N_s)	-	36
Rotor slots number (N_r)	-	25
CW max frequency (f_2)	Hz	17.5
Stack length (l)	mm	200
Stator outer rotor (D_{so})	mm	260
Core flux density (B_c)	T	1.5
Shaft diameter	mm	60
Rotor upper/lower slot width ($b_{r_{1,2}}$)	mm	8
Rotor slot height (h_r)	mm	22
Stator current density (J_s)	A/mm^2	6

in the chapter introduction, only one size of copper bars was available at 20 mm x 6.3 mm. Additional 2 mm in the rotor slot height and widths is considered to provide space for the bar insulations.

With the stack length fixed, the aspect ratio (λ) is not very useful as an input variable. Instead the stator inner diameter (D_{si}) is selected as input variable, with a practical range identified. With D_{si} already decided, the use of J_1 is also somewhat redundant as an input variable. B_1 however is retained as an input variable, as it is used to calculate the number of winding turns. A third variable, the teeth flux density (B_t) is added to the optimization process. The power generated at PW side unity power factor and efficiency are used as output parameters for this optimization. Power density is directly a derivative of the total power because of the fixed 160 L frame volume.

A DOE with 150 points is used to develop the RSA used in this optimization. Less design points are used relative to section 5.3.2, because of the limited design search space allowed by the design constraints. Factoring the stator outer diameter (D_{so}) restrictions imposed by the frame size, parallel teeth may be unattainable for certain DOE points [4]. As a result the slot design is relaxed from necessarily having parallel stator teeth. Instead, limits are placed on the minimum core depth (h_c), and upper stator slot width (b_{s_2}) [5].

---

[4] All the designs in the DOE of section 5.3.2 have parallel stator teeth from the same B_t

[5] see Section B.3 for slot and core dimension calculations

Table 5.5: *Optimization summary of 160L BDFM*

Variable		**Unit**	**Prototype design**	**Optimal design**	
			(FEA)	RSA	FEA
Input	B_1	T	0.23	0.26	
	D_{si}	mm	166	168.8	
	B_t	T	1.4	1.78	
Output (unity Pf)	P_t	kW	4.7	5.2	5.12
	Ef	%	86.5	87	87.17
	PD	kW/m^3	405.9	483	483

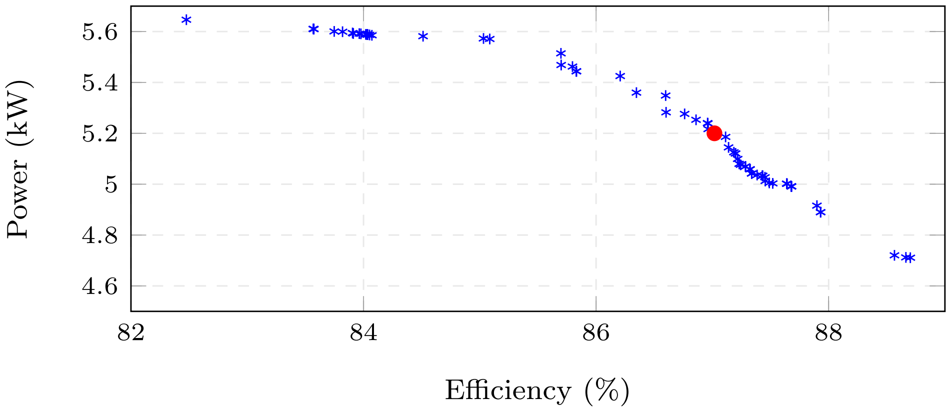

Figure 5.8: *Pareto front of 160L BDFM optimization.*

A simple iterative process is used in the geometric calculations of such designs with unattainable parallel teeth, with alternating reductions in the slot height and core depth. For starters, minimum upper slot teeth width and core depth are chosen. The difference between the selected minimum teeth width and the calculated teeth width is divided in to 3, and is incrementally added to the stator upper slot width, with the stator slot height (h_s) then recalculated. After each increase in b_{s_2} and recalculation of h_s, D_{so} is recalculated. If D_{so} is still higher than the frame restriction, the core depth (h_c) based on the selected B_c is also incrementally reduced. In the case of (h_c), the difference in the calculated (h_c) and the minimum (h_c) is divided into 4 parts.

5.4.2 160L BDFM Optimization results

The optimization Pareto front illustrating the trade-off between power and efficiency is illustrated in Figure 5.8. A design point is selected as indicated by the red dot in Figure 5.8. Details about the selected design are given in Table 5.5. The BDFM design performances in Table

5.5 are all obtained at generating PW unity power factor. All the outputs are increased in the optimized design relative to the prototype model, with the more significant increases observed with $\mathrm{P_t}$ and the power density.

The inner stator diameter (D_{si}) of the prototype design and the optimized design are similar in magnitude, while B_1 and B_t of the optimized design are significantly higher than in the prototype design. This indicates that the machine volume was underutilized with the prototype design. It can also be observed that the RSA results from the optimization process closely matches with the FEA verification, with the largest deviation stemming from $\mathrm{P_t}$, with about 80 W difference.

5.5 Summary

A sequential design and optimization process of BDFMs has been presented. Critical design stages have been highlighted, with relevant equations provided. The formula for the calculation of the BDFM D^2l output coefficient in [47] is simplified using mainly PW parameters. It is worth noting that there are no established specific/standard values for the total electric and magnetic loadings in available BDFM design literature. As such, there is no added complexity in the design process by replacing the total loadings with the PW loadings in the D^2l formula.

A method to select appropriate rotor topologies using BDFM CC models has been illustrated. The decision between an NL rotor and a cage+NL rotor may not always be as straight-forward as the disparity between p_1 and p_2. The power rating and number of loops per nest (q_r) also play a big role. This is illustrated in section 5.3.1, by the choice of the cage+NL rotor with $q_r = 3$ as a suitable rotor for a 5.5 kW BDFM with p_1/p_2 = 2/3. The CC model provides a quick and flexible way to determine the suitable rotor per specific application.

The power density and efficiency optimization of BDFMs using the NSGA-II has been illustrated. The NSGA-II is used with RSAs to reduce optimization time. An initial set of $\mathrm{P_t}$ ranges are used to identify optimal output regions. The input variables of these regions are also identified in the process. For final optimization, the $\mathrm{P_t}$ ranges are then narrowed and final design are chosen based on prioritized performances.

Two optimization instances have been considered. The first is an unconstrained 5.5 kW BDFM, while the volume of the other design is constrained to a 160L IM frame. The use of RSAs has been shown to provide a computationally efficient method for optimizing BDFMs at reasonable accuracy.

Chapter 6

Power density comparison between BDFMs and DFIGs

There are available BDFM literature that discuss the power density of BDFMs with different pole pair combinations. There have also been power density comparisons between BDFMs and DFIGs. These literature have provided useful information highlighting suitable pole pair combinations and the lower power density of BDFMs with respect to DFIGs. In this chapter, the evaluation approach introduced in chapter 4, is used for power density comparisons of BDFMs and DFIGs at different power levels. Optimizations as discussed in chapter 5 are used to produce BDFM and DFIG designs for comparisons. Pole pair combinations used for the BDFM topologies are also compared for their relative performances.

6.1 Introduction

The appeal of BDFMs as alternatives to DFIGs stems from the absence of slip ring and brush assemblies, and the consequent improved reliability. The use of similar sized control systems, and the better low voltage ride through capabilities of BDFMs are also significant factors. However, as analysed in [22], BDFMs suffer about a quarter reduction in power ratings compared to similarly sized DFIGs. To further exacerbate the power density discrepancy, the analysed BDFMs in [23] have substantially more than a quarter increase in mass when compared with DFIGs of similar power and operating speed.

In chapter 4, it has been demonstrated how proper consideration of generating synchronous doubly fed operations and power factor lead to improved BDFM evaluations. In this chapter, the methodology for evaluating BDFM models from chapter 4 is employed for comparisons of BDFMs and DFIGs at different power levels. The primary objective in this chapter is not to display a better basis for BDFM and DFIG comparison. There is an overarching focus on efficiency and capital expenditure of the machines being compared in [23]. In this chapter, the pattern of power density (PD) disparities between BDFMs and DFIGs is investigated across different power levels and BDFM pole pair combinations. The relative performances of selected BDFM pole pair combinations are observed and insight into the (magnetic and electric) loading patterns of BDFMs at different power levels is provided

In [23], the optimization variables are geometric machine variables such as the stator inner (r_{si}), stack length (l), rotor slot size etc. In this chapter, the optimization variables for BDFMs, similar to chapter 5, are the PW flux density (B_1), PW electric loading (J_1), and the stack aspect ratio (λ). The optimization variables for DFIGs are the maximum airgap flux density (B_g), total electric loading ($\bar{J}$), and λ. The BDFM maximum airgap flux density (B_{sum}) and total electric loading ($\bar{J}$), based on the selected B_1 and J_1 [1], are also specified to provide a bit of loading comparison between the BDFMs and DFIGs. Nonetheless, it should be noted that the BDFM B_{sum} and $\bar{J}$ function slightly different from DFIG B_g and $\bar{J}$, as expounded in [22, 47].

The BDFMs are designed using the processes discussed in chapter 5. It is recognized that flux densities, electric loadings and aspect ratios are directly involved in the calculations of the r_{si} and l. Nevertheless, critical PW & CW parameters like number of turns and currents, are calculated using assigned flux densities. These (PW & CW) parameters appear to be fixed in [23].

Three popularly used BDFM pole pair combinations in available literature (p_1/p_2 = 2/3, 2/4, 4/6) are considered at different stages for the comparisons. The power levels considered are 5.5 kW, 75 kW, 250 kW and 5.3 MW. The design in chapter 5 is rated at 5.5 kW, thus the comparisons are started at this rating. The 250 kW BDFM in [24] is the largest reported BDFM built to date, therefore this power rating is also considered. 75 kW is taken as a reasonable power rating between 5.5 and 250 kW. BARD offshore I wind farm is a 400 MW wind farm, and its turbines use DFIGs. The DFIGs used are rated around 5.3 MW at a maximum speed of about 1212 rpm [105–107]. As a result, 5.3 MW is selected as the highest power rating for BDFM and DFIG comparisons in this chapter.

6.2 Specifications of compared machines

An outline of the design specifications for each investigated power rating is given in Table 6.1. The selected pole pair combinations of the BDFMs are given alongside the DFIG with

---

[1] see equations B.1.6 - B.1.9

Table 6.1: *Outline of compared topologies*

Power	Type	Pole pairs	Stator slots	Rotor slots	Grid voltage (V_1)
5.5 kW	BDFM	2/3	36	30	230
	BDFM	2/4	48	36	
	DFIG	5	90	60	
	DFIG	6	108	72	
75 kW	BDFM	2/4	48	36	230
	BDFM	4/6	72	80	
	DFIG	6	108	72	
	DFIG	10	180	120	
250 kW	BDFM	2/4	72	60	400
	BDFM	4/6	72	80	
	DFIG	6	108	72	
	DFIG	10	180	120	
5.3 MW	BDFM	2/4	72	60	690
	BDFM	4/6	72	80	
	DFIG	6	108	72	
	DFIG	10	180	120	

corresponding speed. All the BDFMs and DFIGs are designed and simulated at a maximum slip of 0.35 and a grid frequency of 50 Hz. The $p_1/p_2 = 2/3$ combination is only used for the 5.5 kW power rating, as the subsequent power ratings are reasonably large with potentially more pronounced effects of unbalanced magnetic pull. The PW voltage used for the 5.3 MW topologies is based on voltage stated in [107] for the Bard 5.0 offshore generators.

The isolated loops (IL) rotor as described in [14] [2] is used for the models in this chapter. IL rotors are used because they can be modelled without the use of an external circuit in Ansys EDT, which is required for NL or cage+NL rotors. This reduces computation time. Also, there is symmetry with the models of some pole pair combinations, and this enables the possibility of reduced models, which also significantly reduces computation time. Furthermore, IL rotors have similar advantages to NL rotors, and arguments can be made for their suitability in certain BDFM applications (see Appendix D).

6.3 Machine topology comparisons

The optimizations in this chapter are not conducted to obtain singular candidate designs at each power level of either machine type. Instead, the objective is to illustrate the ceiling of machine performances at different power levels. As such, Pareto fronts are used to illustrate performance. Similar to chapter 5, the optimization objectives are to maximize efficiency (Ef)

---

[2] See sections 2.2.4 & 2.3.2

Table 6.2: *Topology DOE details at 5.5 kW*

Variable		Unit	5.5 kW DOEs			
			BDFM 2/3	BDFM 2/4	DFIG 5p_1	DFIG 6p_1
Input	B_{sum}/B_g (B_1)	T	0.33 - 0.67 (0.15 - 0.3)	0.29 - 0.68 (0.12 - 0.28)	0.4 - 0.65	
	$\bar{J}$ (J_1)	kA/m	15.6 - 33.4 (7 - 15)	17 - 29 (7 - 12)	12 - 22	
	λ	-	0.5 - 1			
Output	P_t	kW	0.9 - 5.1	2.25 - 4.75	3.48 - 5.13	1.9 - 5
	Ef	%	61.8 - 89.5	81.5 - 88	90.5 - 93.4	89.8 - 93.3
	PD	kW/m^3	90.4 - 453.8	195.4 - 378.9	306.3 - 696.5	155.9 - 557.7

and power density (PD) at generating PW unity power factor, with a constraint placed on the total power (P_t) generated [3].

Based on the use of Pareto fronts to illustrate the performance of BDFM and DFIG topologies, the PD and efficiency comparisons become somewhat subjective. As a result, upper and lower ends of the DFIG Pareto fronts are compared individually with the Pareto front upper and lower ends of the BDFMs with corresponding speeds.

6.3.1 Topology comparisons at 5.5 kW

Details of the DOEs for the different 5.5 kW machine topologies are given in Table 6.2. Similar aspect ratios are used for all topologies, as the range is reckoned to encompass the high performing designs of the different topologies. Lower B_1 and J_1 are used for the 2/4 BDFM because of the slower speed. However, the higher difference between p_1 and p_2 for the 2/4 topology compared to the 2/3 topology, reduces the difference in the BDFM total loadings. From Table 6.2, it can be seen that the 2/4 BDFM has the lowest ceiling for P_t at unity power factor; the efficiency of the 2/4 topology is also the lowest.

The optimal Pareto fronts of the different topologies at 5.5 kW are illustrated in Figure 6.1. The details of these Pareto fronts are also given in Table 6.3. Expectedly, the DFIGs outperform the BDFMs at corresponding rated speeds. The DFIGs candidates have considerably higher efficiencies and PDs than their BDFM counterparts. Predictably, the machines with higher rated speeds have higher PDs than similar machine types with lower rated speeds. It can be observed from Table 6.3, that the Pareto candidates of the selected topologies at 5.5 kW generally have a low stack aspect ratio.

---

[3] The power generated and efficiency are calculated according to Appendix A.

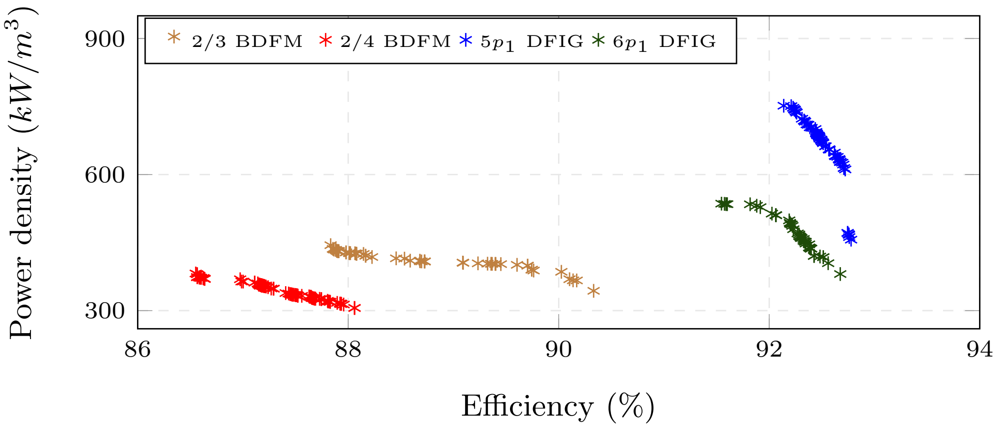

Figure 6.1: *Pareto fronts of topologies compared at 5.5 kW.*

Table 6.3: *Topology Pareto front details at 5.5 kW*

Variable		**Unit**	**5.5 kW Pareto fronts**			
			BDFM 2/3	BDFM 2/4	DFIG $5p_1$	DFIG $6p_1$
Input	B_{sum}/B_g (B_1)	T	0.53 - 0.71 (0.24 - 0.32)	0.6 - 0.68 (0.25 - 0.28)	0.546 - 0.64	0.525 - 0.54
	$\bar{J}$ (J_1)	kA/m	18.7 - 25.1 (8.4 - 11.3)	16.9 - 24.1 (7 - 10)	14.68 - 23	16.8 - 21.86
	λ	-	0.5 - 0.68	0.5 - 0.54	≈ 0.5	0.5 - 0.55
Output	P_t	kW	4.6 - 4.77	4.3 - 4.5	4.6 - 4.77	4.55 - 4.74
	Ef	%	87.6 - 90.3	86.5 - 88.1	92.2 - 92.8	91.6 - 92.4
	PD	kW/m^3	385.6 - 444.3	304.2 - 381.9	471.2 - 750.9	442 - 535.4

The P_t values for the candidate designs of the Pareto fronts for all topologies are significantly less than 5.5 kW. The 2/4 BDFM topology design candidates register the lowest P_t values at unity power factor. The disparity in PD between the $5p_1$ DFIGs and the 2/3 BDFMs is more pronounced at the lower efficiency/higher PD regions of the Pareto fronts, compared to the $6p_1$ and 2/4 BDFM. However, the 2/3 BDFM topology has a significantly higher efficiency ceiling than the 2/4 BDFM topology.

6.3.1.1 5.5 kW Pareto fronts: BDFMs - higher power density DFIGs

The PD of the upper end [4] of the 2/3 BDFM Pareto front is 59 % of the upper end of the $5p_1$ DFIG Pareto front with about 4.6% lower efficiency than the DFIG. The lower PD end[5] of the

---

[4] Higher power density (PD) or lower efficiency end.

[5] Lower power density or higher efficiency end.

2/3 BDFM Pareto front is about 51 % of the upper end of the $5p_1$ DFIG Pareto front, with about 2.5% decrease in efficiency.

The upper end PD of the 2/4 BDFM Pareto front is about 71% of the upper end of the $6p_1$ Pareto front with a decrease of about 5.1% decrease in efficiency. Also, the lower end PD of the 2/4 BDFM Pareto front is around 57% of the upper end PD of the $6p_1$ Pareto front, alongside a drop of 3.5% in efficiency.

6.3.1.2 5.5 kW Pareto fronts: BDFMs - lower power density DFIGs

The upper PD end of the 2/3 BDFM Pareto front is about 74% of the lower PD end of the $5p_1$ Pareto front[6], with about 5% decrease in efficiency. The lower PD end of the 2/3 BDFM Pareto front is about 64% of the lower PD end of the $5p_1$ Pareto front, with about 2.5% decrease in efficiency.

Meanwhile, the upper PD end of the 2/4 BDFM Pareto front is about 86% of the lower PD end of the $6p_1$ Pareto front, and the drop in efficiency is at about 5.9%. The lower end PD of the 2/4 BDFM Pareto front is approximately 69% of the lower end PD of the $6p_1$ Pareto front, with an accompanying 4.3% reduction in efficiency.

6.3.2 Topology comparisons at 75 kW

Details of the DOEs for the different 75 kW machine topologies are given in Table 6.4. As earlier stated, the 2/3 BDFM topology is not considered for the 75 kW power rating, because of the effects of unbalanced magnetic pull. The 4/6 BDFM topology which is a multiple of the 2/3 topology is considered alongside the $10p_1$ DFIG instead. The magnetic and electric loading ranges are increased for this power rating compared to 5.5 kW, as the machines are bigger with less threat of saturation. The stack aspect ratio ranges are also increased. Lower values of B_1, J_1 and λ are used for the 4/6 BDFM topology because of the significantly lower rated speed. In addition, higher values of λ are used for the DFIG topologies, as DFIGs have less risk of saturation compared to BDFMs.

Like the compared 5.5 kW topologies, the topologies with higher rated speed have significantly higher PD. Although the $6p_1$ DFIG topology has a higher recorded efficiency compared to the $10p_1$ topology, the 4/6 BDFM topology has a marginally peak recorded efficiency compared to the 2/4 BDFM topology. It can also be observed that the highest recorded $\mathrm{P_t}$ for the 2/4 topology is considerably lower than the 75 kW mark, with the other topologies having recorded $\mathrm{P_t}$ values significantly higher than 75 kW.

---

[6] The design point around 600 kW/m^3 on the $5p_1$ Pareto front is used, because it has about the same efficiency as the points with power density less than 600 kW/m^3.

Table 6.4: *Topology DOE details at 75 kW*

Variable		Unit	75 kW DOEs			
			BDFM 2/4	BDFM 4/6	DFIG $6p_1$	DFIG $10p_1$
Input	B_{sum}/B_g (B_1)	T	0.43 - 0.87 (0.18 - 0.36)	0.33 - 0.78 (0.15 - 0.35)	0.4 - 0.8	0.4 - 0.75
	$\bar{J}$ J_1	kA/m	19.3 - 48.3 (8 - 20)	17.8 - 40 (8 - 18)	15 - 30	15 - 28
	λ	-	0.7 - 1.4	0.7 - 1.3	0.9 - 1.6	0.8 - 1.5
Output	P_t	kW	43.2 - 67.8	59.8 - 79.3	51.7 - 82.6	47 - 77.2
	Ef	%	87.7 - 93.9	86.4 - 94.2	93.8 - 96.4	91.2 - 95.5
	PD	kW/m^3	356.5 - 665.8	218.8 - 511.8	406.7 - 1147	247 - 619

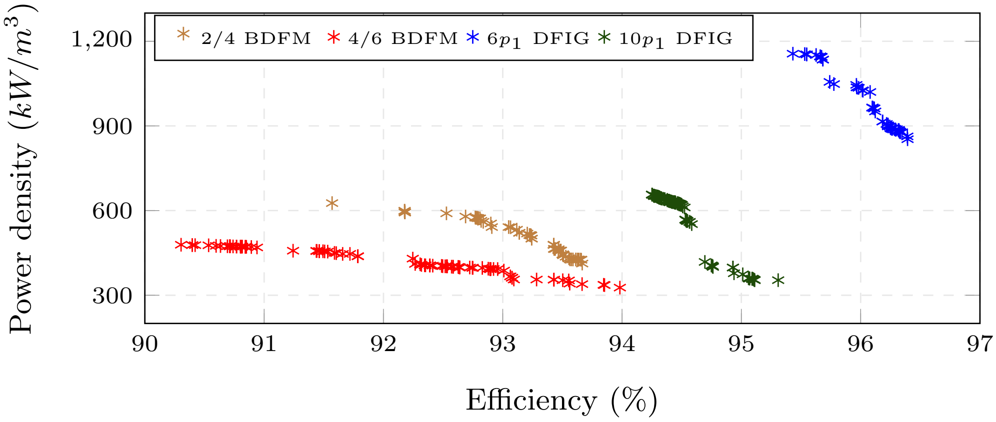

Figure 6.2: *Pareto fronts of topologies compared at 75 kW.*

The Pareto fronts of the different topologies at 75 kW are illustrated in Figure 6.2, while the details of these Pareto fronts are given in Table 6.5. The lower regions of stack aspect ratio ranges are once again favourable for candidate designs for all topologies. The Pareto designs for the DFIG topologies have higher magnetic and electric loadings compared to the 5.5 kW counterparts. On the other hand, the magnetic loadings of the 2/4 BDFM Pareto front designs are not too far off from the 5.5 kW BDFM designs, howbeit with higher electric loading.

6.3.2.1 75 kW Pareto fronts: BDFMs - higher power density DFIGs

The upper end PD of the 2/4 BDFM Pareto front is about 54% of the upper end of the $6p_1$ DFIG Pareto front with about 4.1% decrease in efficiency. The lower end PD of the 2/4 BDFM Pareto front is around 39% of the upper end PD of the $6p_1$ DFIG Pareto front, with a drop of 1.8% in efficiency.

Table 6.5: *Topology Pareto front details at 75 kW*

Variable		Unit	75 kW Pareto fronts			
			BDFM 2/4	BDFM 4/6	DFIG $6p_1$	DFIG $10p_1$
Input	B_{sum}/B_g (B_1)	T	0.58 - 0.77 (0.24 - 0.32)	0.65 - 0.74 (0.29 - 0.34)	0.69 - 0.77	0.6 - 0.74
	$\bar{J}$ (J_1)	kA/m	21.2 - 38.6 (8.8 - 16)	20 - 33.4 (9 - 15)	21.4 - 30	15.6 - 28
	λ	-	0.7 - 1.1	0.7 - 0.8	0.9 - 0.98	0.8 - 1
Output	P_t	kW	63 - 64.1	70 - 71.2	75 - 78	67 - 71
	Ef	%	91.3 - 93.6	90.3 - 94	95.4 - 96.4	94.3 - 95.3
	PD	kW/m^3	452 - 627.4	327 - 479	850 - 1156	352 - 657

The higher PD end of the 4/6 BDFM Pareto front gets up to about 73% of the $10p_1$ DFIG Pareto front upper extreme, with about 4% less efficiency. It can be seen that there is relatively minimal PD variation on the 4/6 BDFM Pareto front. A design point around 92.2% on the 4/6 BDFM Pareto front is about 65% of the upper end PD of the $10p_1$ DFIG Pareto front, with only about 2.1% reduction in efficiency. On the other hand, the lower PD end of the 4/6 BDFM is about 50% of the upper PD end of the $10p_1$ Pareto front, with only about 0.3% efficiency deficit.

6.3.2.2 75 kW Pareto fronts: BDFMs - lower power density DFIGs

The upper PD end of the 2/4 BDFM Pareto front is about 74% of the lower PD end of the $6p_1$ DFIG Pareto front, and the drop in efficiency is at about 5.1%. The lower end PD of the 2/4 BDFM Pareto front is approximately 53% of the lower end PD of the $6p_1$ DFIG Pareto front, with an accompanying 2.8% reduction in efficiency.

The higher PD boundary of the 4/6 BDFM is about 146% of the lowest PD on the $10p_1$ DFIG Pareto front, with about 5% reduction in efficiency. The earlier considered PD point on the 4/6 BDFM Pareto front is about 122% of the lowest PD point on the $10p_1$ DFIG Pareto front, and has about 3.1% reduction in efficiency. The lowest PD point on the 4/6 BDFM measures up to about 93% of the lowest PD point on the $10p_1$ Pareto front, with only about 1.3% reduction in efficiency.

6.3.3 Topology comparisons at 250 kW

Details of the topologies investigated at 250 kW are given in Table 6.6. The magnetic and electric loadings are increased for all topologies, from what was used for the 75 kW designs. All topologies except the 2/4 BDFM topology register designs which generate up to 250 kW

Table 6.6: *Topology DOE details at 250 kW*

Variable		**Unit**	**250 kW DOEs**			
			BDFM 2/4	BDFM 4/6	DFIG $6p_1$	DFIG $10p_1$
Input	B_{sum}/B_g (B_1)	T	0.48 - 0.96 (0.2 - 0.4)	0.44 - 0.89 (0.2 - 0.4)	0.6 - 0.95	
	$\bar{J}$ (J_1)	kA/m	24 - 60 (10 - 25)	22.2 - 55.6 (10 - 25)	20 - 50	
	λ	-	1 - 1.6			
Output	P_t	kW	38.6 - 234.7	126 - 252.5	151 - 273	111.8 - 260.7
	Ef	%	55.8 - 94.5	85- 95	57.9 - 96.7	73.6 - 95.8
	PD	kW/m^3	212 - 914.4	330.5 - 731	620.6 - 2070	509 - 1253

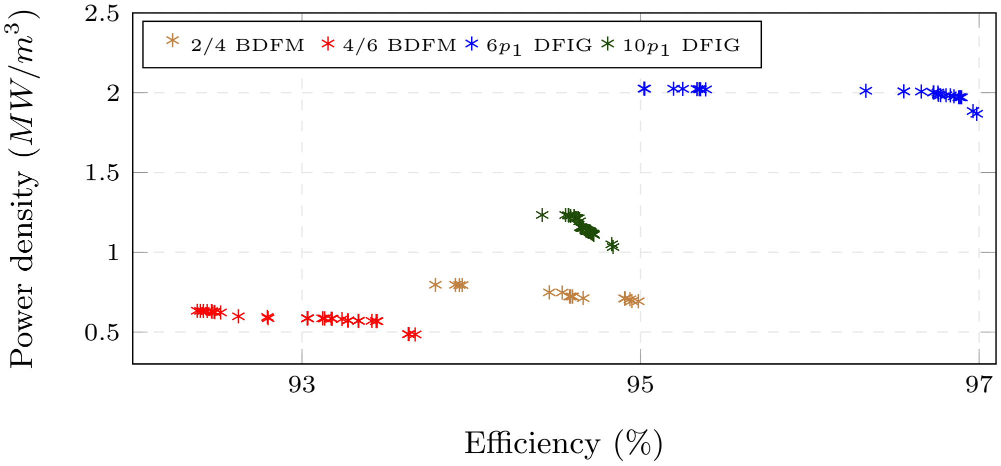

Figure 6.3: *Pareto fronts of topologies compared at 250 kW.*

at PW unity power factor, with the $6p_1$ DFIG topology having designs with P_t as high as 270 kW. The highest P_t recorded for the 2/4 BDFM topology is about 235 kW, which is well off the desired 250 kW rating. The 4/6 BDFM once again registers a marginally higher peak efficiency value than the 2/4 topology. This is in contrast with the DFIG topologies, with the $6p_1$ DFIG's highest efficiency being significantly higher than the slower $10p_1$ DFIG's highest efficiency.

The Pareto fronts of the topologies investigated at 250 kW are illustrated in Figure 6.3, with the details of these Pareto fronts given in Table 6.7. By casual inspection, it is clear that the DFIG topologies have a wider margin of difference in PD compared to the BDFM topologies; the Pareto fronts of the 2/4 & 4/6 BDFM topologies have narrow PD variations. The aspect ratios of the designs in the topology Pareto fronts at 250 kW, are moderately higher than those of the 75 kW designs.

Table 6.7: *Topology Pareto fronts at 250 kW*

Variable		Unit	250 kW Pareto fronts			
			BDFM 2/4	BDFM 4/6	DFIG $6p_1$	DFIG $10p_1$
Input	B_{sum}/B_g (B_1)	T	0.64 - 0.72 (0.264 - 0.3)	0.73 - 0.87 (0.33 - 0.39)	0.66 - 0.78	0.68 - 0.73
	$\bar{J}$ (J_1)	kA/m	26.8 - 32.3 (11.1 - 13.4)	23.4 - 33 (10.5 - 14.8)	35.9 - 50	39.4 - 48.4
	λ	-	1 - 1.4	1 - 1.4	1.1 -1.4	≈ 1
Output	$\mathrm{P_t}$	kW	220 - 226	220 - 226	255 - 269	250 - 252
	Ef	%	93.8 - 95	92.4 - 93.7	95 - 97	94.4 - 94.8
	PD	kW/m^3	692.6 - 796.2	485 - 633	1870 - 2025	1032 - 1234

6.3.3.1 250 kW Pareto fronts: BDFMs relative to the higher power density DFIGs

The upper end PD of the 2/4 BDFM Pareto front is about 39% of the upper end of the $6p_1$ DFIG Pareto front, with a decrease of about 1.2% in efficiency. The lower PD end of the 2/4 BDFM Pareto front is about 37% of the upper PD end of the $6p_1$ DFIG Pareto front, with identical efficiency.

The highest PD point for the 4/6 BDFM Pareto front is about 51% of the highest $10p_1$ PD, with a decrease in efficiency of about 2%. The lowest PD point on the 4/6 BDFM is approximately 39% of the highest PD on the $10p_1$ DFIG, and has about 0.7% less efficiency.

6.3.3.2 250 kW Pareto fronts: BDFMs relative to the lower power density DFIGs

The upper PD end of the 2/4 BDFM Pareto front is about 42.6% of the lower PD end of the $6p_1$ DFIG Pareto front, and the drop in efficiency is about 3.2%. The lower end PD of the 2/4 BDFM Pareto front is approximately 37% of the lower end PD of the $6p_1$ DFIG Pareto front, with an accompanying 2% reduction in efficiency.

The highest PD point of the 4/6 BDFM Pareto front is about 61.3% of the lowest PD point on the $10p_1$ Pareto front, with about 2.4% less efficiency. The lowest PD point on the 4/6 BDFM Pareto front is about 47% of the lowest PD point of the $10p_1$ Pareto front, with a 1.1% reduction in efficiency.

6.3.4 Topology comparisons at 5.3 MW

The DOE details of the BDFM and DFIG topologies considered at 5.3 MW are given in Table 6.8. The magnetic and electric loadings of the topologies are increased relative to the previous

Table 6.8: *Topology DOE details at 5.3 MW*

Variable		Unit	5.3 MW DOEs			
			BDFM 2/4	BDFM 4/6	DFIG 6p_1	DFIG 10p_1
Input	B_{sum}/B_g	T	0.48 - 1.09	0.44 - 1	0.7 - 1.4	
	(B_1)		0.2 - 0.45			
	$\bar{J}$	kA/m	24.1 - 84.5	22.2 - 77.9	30 - 70	
	(J_1)		10 - 35			
	λ	-	1 - 1.8		1 - 2.2	
Output	P_t	MW	2.05 - 5.06	3.72 - 5.27	4.02 - 5.86	3.56 - 5.9
	Ef	%	74.5 - 97	88.4 - 97.4	97.6 - 98.6	95.7 - 97.8
	PD	MW/m^3	0.58 - 1.94	0.36 - 1.42	1.54 - 3.74	0.99 - 2.56

(250 kW) power rating. Identical B_1 and J_1 ranges are used for the BDFMs, likewise, identical B_g and $\bar{J}$ ranges are used for the DFIG topologies.

Both DFIG topologies register designs with P_t values $\geq$ 5.3 MW at PW unity power factor. On the other hand, the highest recorded power for the 2/4 BDFM is 5.02 MW, while that of

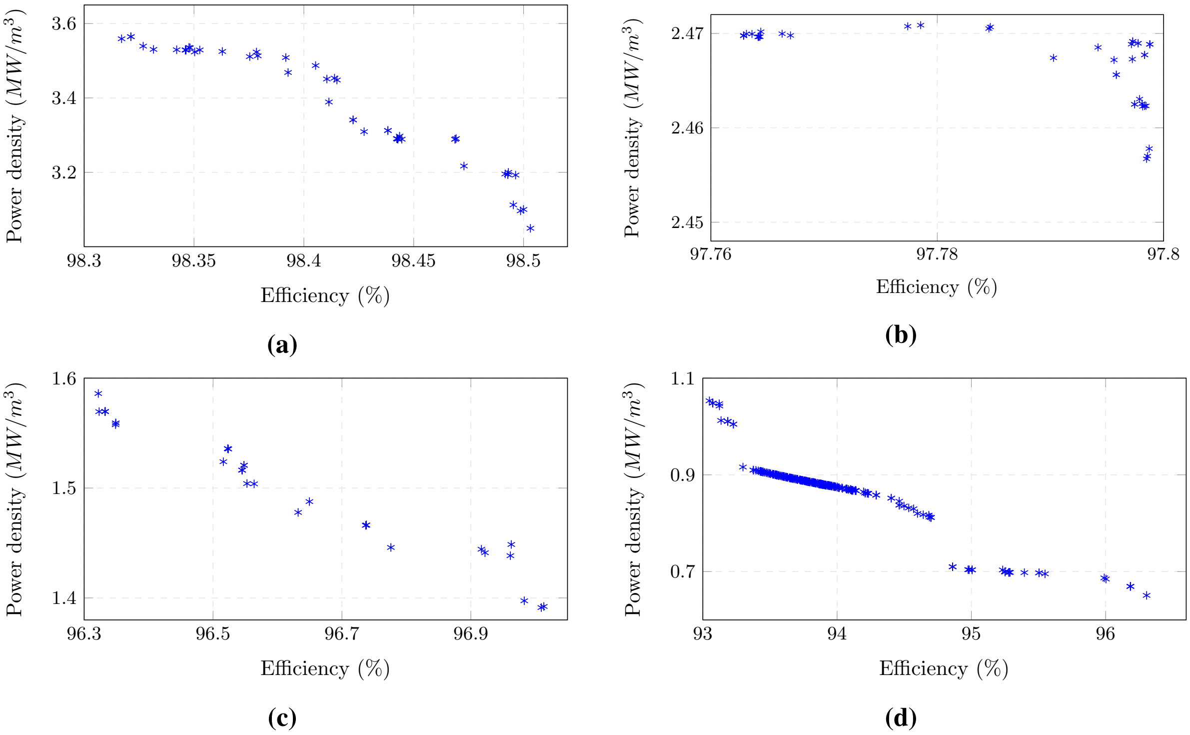

(a) **(b)** **(c)** **(d)**

Figure 6.4: *PD vs Ef Pareto fronts at 5.3 MW (a) 6 p_1 DFIG, (b) 10 p_1 DFIG, (c) 2/4 BDFM, (d) 4/6 BDFM.*

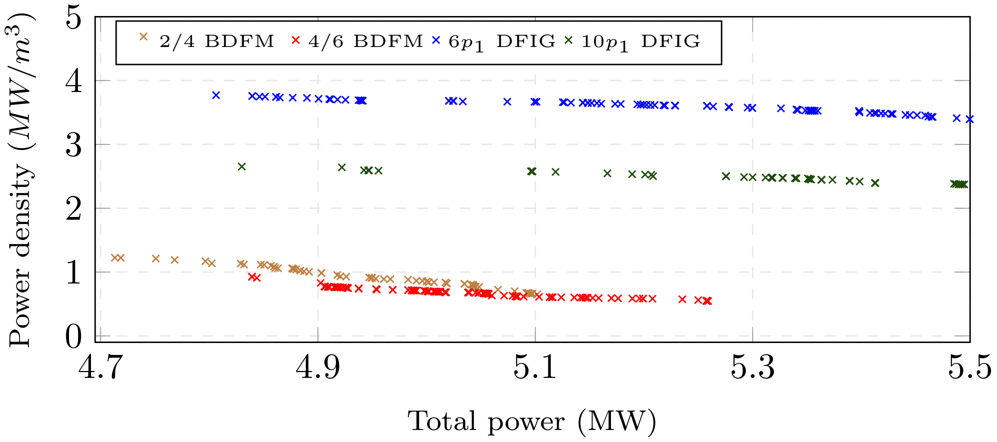

Figure 6.5: *PD vs* P_t *Pareto fronts of topologies at 5.3 MW.*

the 4/6 BDFM is 5.27 MW. The highest efficiency from the 4/6 DOE is about 0.4 % higher than that listed in the 2/4 DOE. Meanwhile, the $6p_1$ DFIG topology DOE has its highest listed design efficiency at about 0.8 % higher than that of the $10P_1$ DFIG DOE.

The Ef vs PD Pareto fronts of the topologies investigated at 5.3 MW are illustrated in Figure 6.4. The efficiency ranges in the Ef vs PD Pareto fronts for the DFIGs are very narrow, and placing all the Pareto fronts together would provide little information for comparison. This is why separate Pareto front plots are illustrated for the topologies at 5.3 MW. It is worth noting that the P_t range for the Pareto front of the 2/4 BDFM topology in Figure 6.4(c) is between 4.5 - 4.67 MW, while that of the 4/6 BDFM topology in Figure 6.4(d) mostly is around 5 - 5.05 MW.

A different set of Pareto fronts illustrating the trade-offs between the P_t and PD of the topologies is given in Figure 6.5. Constraints of $P_t \geq 4.7$ MW and efficiency $\geq 95\%$, are set for all the topologies, and details of the Pareto fronts are given in Table 6.9. The $6p_1$ DFIG topology has higher PD than the $10p_1$ DFIG topology at all P_t values, and the difference in P_t between the DFIG topologies remains fairly constant. On the other hand, the 2/4 BDFM topology has only a slightly higher PD than the 4/6 BDFM topology till 5.1 MW, at which point the PDs of both topologies are identical. It can also be observed from table 6.9, that the efficiency range of the $6p_1$ DFIG topology is higher than that of the $10p_1$ DFIG topology. Meanwhile, the 4/6 BDFM topology actually has design points with higher efficiency than any of the 2/4 BDFM design points.

Table 6.9: *Topology Pareto front details at 5.3 MW*

Variable		Unit	5.3 MW Pareto fronts			
			BDFM 2/4	BDFM 4/6	DFIG $6p_1$	DFIG $10p_1$
Input	B_{sum}/B_g (B_1)	T	0.53 - 0.68 (0.22 - 0.28)	0.53 - 0.97 (0.22 - 0.4)	0.89 - 1.2	0.99 - 1.4
	$\bar{J}$ (J_1)	kA/m	25 - 50.7 (10.3 - 21)	30.2 - 45.9 (12.5 - 19)	66.6 - 69	61 - 70
	λ	-	1.64 - 1.8	1.5 - 1.8	1.4 - 2	1 - 1.1
Output	P_t	MW	4.71 - 5.1	4.84 - 5.27	4.8 - 5.5	4.8 - 5.5
	Ef	%	95 - 95.7	95 - 96.6	98.3 - 98.4	97.6 - 97.8
	PD	MW/m^3	0.65 - 1.22	0.55 - 0.93	3.4 - 3.77	2.37 - 2.65

6.4 Conclusion

As already demonstrated in chapter 4, BDFM power density (PD) at PW unity power factor is significantly lower than the PD at generating maximum torque. The trade-off between efficiency and PD produces different contexts of power density comparisons between BDFMs and DFIGs. These contexts are discussed for investigated BDFM and DFIG topologies at different power ratings in this chapter.

Power generated (P_t) at PW unity power factor is also considered, and it has significant implications in selecting suitable pole pair combinations for BDFMs. The 2/4 BDFM topology seems to have greater reduction in P_t (and consequently PD) at PW unity power factor, compared to 4/6 BDFMs. Also, it is difficult to achieve the desired P_t at unity power factor for the 2/4 BDFM topology using current BDFM sizing calculations. With similar values for B_1, J_1 and λ, the 4/6 BDFM topology apparently generates higher P_t at PW unity power factor compared to the 2/4 topology. It appears that some compensation in sizing is required for the 2/4 topology.

The 4/6 BDFM topology which is at a significantly lower rated speed has comparable PD around the desired P_t for the investigated 5.3 MW designs. The 4/6 BDFM topology is also able to achieve similar efficiency values with the 2/4 BDFM topology, especially at MW ratings.

The increase in electric and magnetic loadings at higher power is less in BDFMs compared to DFIGs, and this requires further investigation. This is identified as an additional significant factor in the discrepancy in PD between BDFMs and DFIGs at MW ratings.

Chapter 7

Conclusions and recommendations

Aspects of BDFM design have been investigated and detailed in this dissertation. In this chapter, unique contributions of this study are first outlined. Conclusions and recommendations drawn from the study are then discussed, after which future research directions are given.

7.1 Study contributions

The contributions of this study are listed below

- The design development of BDFMs to date has been presented according to a topical layout. The history of BDFMs is traced back to the quest for reliable variable speed motors at the turn of the 19th century. This is used to provide perspective on the contemporary designs of BDFMs. A summary of critical aspects of BDFM design is then given, with relevant literature listed for would be BDFM designers.
- A coupled circuit model of BDFMs developed during this study is presented. The winding function theory is used to calculate the different BDFM (self and mutual) winding inductances. A quick evaluation of the relative torque performances of different rotor topologies per specific BDFM application can be conducted using the model. Interactions between BDFM rotor and stator windings are illustrated based on their mutual inductances, and this is used to assess relative levels of torque ripple in BDFMs. Furthermore, torque contributions of each loop in a BDFM rotor nest can be investigated using the model, which is useful in BDFM rotor design. The model is also used to provide a computationally cheap method for estimating rotor currents for rotor design purposes.

- A systematic approach to BDFM design evaluation is presented. The design evaluation takes proper considerations of operational mode and grid code requirements of BDFMs in wind turbines. It is also demonstrated how evaluating BDFM designs in other modes aside the synchronous doubly fed generating mode potentially leads to inaccurate performance evaluations.

- A BDFM design methodology has been presented. The present standard BDFM airgap sizing calculation is first simplified. The aforementioned coupled circuit model is used to select appropriate rotor topology, and estimate the rotor loop currents. An optimization process using the non-dominated sorting genetic algorithm (NSGA-II) is presented.

  Although using NSGA-II with FEA machine models is not novel, the optimization process in this study uses a response surface approximation from FEA results with NSGA-II. Also, for the optimization process, designs are evaluated at PW unity power factor in the synchronous doubly fed generating mode. This optimization approach is unique to this study.

- The investigation of pole pair combinations at different power levels introduces fresh insight in determining relatively better performing combinations. Also, a robust attempt at identifying suitable electric and magnetic loadings of BDFMs at different power ratings is conducted. Furthermore, the power densities of BDFMs compared with DFIGs at different power levels are delineated.

7.2 Conclusions and recommendations

Important conclusions and ensuing recommendations from this study are outlined as follows

- Rotor loop spans relative to stator winding pole pitches are significant factors contributing to the nature of torque ripple produced in BDFMs. This can be somewhat previewed by the waveform over one complete revolution of the mutual inductances between the rotor loops and the stator windings. The closer the waveform is to a sinusoid, the less ripple that rotor loop contributes.

  It is already known that loop spans dictate the torque contribution of rotor loops, thus a bigger loop with high ripple has larger effects on the total ripple produced in the BDFM. This is particularly true for NL rotors, as all the loops are in phase, and the loops combine directly to produce torque or torque ripple. For the cage+NL rotor, the cage is out of phase with the nested loops, and there is a more complex interaction.

- There are substantial disparities in performances of doubly fed machines in asynchronous and synchronous doubly fed modes. Also, motoring mode performances are significantly different from generating mode performances. Furthermore, it has been illustrated that the power factor of BDFMs at maximum synchronous generating mode torque, based on a particular CW excitation, is typically outside grid code required power factors.

As a result, to give an accurate context of performance, it is recommended that evaluations of BDFM designs be conducted in the doubly fed generating mode. Unity power factor is at the mid-point of operable power factor conditions in wind turbines, it is therefore proposed that BDFMs be simulated at PW unity power factor for design and comparison purposes. It is recognized that power factor considerations are not common in DFIG design evaluation in literature. However, DFIGs are less prone to the effects of saturation compared to BDFMs; BDFMs also have considerably high rotor leakage inductances. As a result, more attention is needed in evaluating BDFM designs.

- When power density optimizations are conducted at PW unity power factor in the synchronous doubly fed generating mode, many designs being evaluated may have their total power generated falling short of desired power rating. However, these designs may have high power densities and efficiencies. Trade-offs considering power density, power rating and efficiencies are therefore recommended, instead of just considering power density and efficiency.

- Response surface approximations (RSAs) developed from FEA results of BDFM designs can be effectively coupled with optimization algorithms for power density optimizations. Reasonably accurate results are obtainable from this optimization approach, with greatly reduced computational time compared to direct FEA optimizations. Nevertheless, attention should be given to the goodness of fit for the developed RSA.

- If designs evaluations are recommended to be conducted in the synchronous generating doubly fed mode, at PW unity power factor, then topology comparisons should also be conducted under this conditions. If not constrained to a specific operating speed, a robust approach to selecting a suitable BDFM pole pair combination, is to compare the performance of each combination with DFIGs at corresponding speeds. The disparity between the DFIGs and BDFMs provide useful insight into the better performing BDFM pole pair combination.

- Simulation results in this study suggest that the increase in electric and magnetic loading permissible for BDFMs with increasing power rating is lower than that of DFIGs. As such, the disparity in power density between DFIGs and BDFMs seemingly increases with rising power ratings. However, the efficiency disparity between BDFMs and DFIGs does not really change with increasing power ratings, with BDFMs having slightly less efficiency, due to the added winding.

- From simulation results, and considering the evaluation conditions used in this study, the 4/6 pole pair combination for BDFMs has better performance than the 2/4 combinations when compared with DFIGs of corresponding speeds across different power levels. The power density disparity between the $10p_1$ DFIGs and the 4/6 BDFMs is significantly less than that between $6p_1$ DFIGs and 2/4 BDFMs. Similar peak efficiency values to the 2/4 topology are achievable with the 4/6 topology, despite the significant difference in speed. Also, the 2/4 topology consistently failed to achieve the desired power rating at PW unity power factor, suggesting higher risk of derating with the 2/4 topology, for operations at unity power factor.

7.3 Future research directions

A lot of research work is still needed for the design development of BDFMs. The disparity between DFIGs and BDFMs power density at MW levels is quite high, and there are investigations towards lowering this disparity that can still be conducted. Methods for increasing the electric and magnetic loadings without compromising performance at grid code required operations can be prioritized. A few aspects that can be further examined include

- The consideration of pole pair combinations other than the 2/4 and 4/6 combinations. In [49] and [55], viable pole pair combinations are suggested and compared. These combinations can be evaluated using FEA and similar evaluation methods suggested in this study.
- The usage of higher pole numbers on the PW can be revisited in terms of loading limits and relative B_1 to B_2 ratios. The rotor frequency will also be lower, and the benefits can be explored further.
- BDFMs have an asynchronous torque contribution which changes with slip. This means that the difference in power density between BDFMs and DFIGs can be potentially adjusted at higher slips. This has implications on the converter sizing, but the benefits may outweigh the costs.
- Suitable winding voltages at MW ratings, and the implications on electric and magnetic loading limits can be investigated.

For power density comparisons, the size of slip rings and brushes in DFIGs can be factored in as suggested in [22]. The coupled circuit model presented in this study can be further improved with more accurate analysis of BDFM rotor leakages. Saturation factors can also be applied to the model for considerations of non-linearity.

References

[1] REN21, *Renewables 2020 Global Status Report*, Paris: REN21 Secretariat, 2020.

[2] ——, *Renewables 2005 Global Status Report*, Washington, DC: Worldwatch Institute, 2005.

[3] GWEC, "Global wind report 2021," Brussels, Belgium, Tech. Rep., March 2021.

[4] H. Polinder, J. A. Ferreira, B. B. Jensen, A. B. Abrahamsen, K. Atallah, and R. a. McMahon, "Trends in Wind Turbine Generator Systems," *IEEE Journal of Emerging and Selected Topics in Power Electronics*, vol. 1, no. 3, pp. 174–185, 2013.

[5] S. Muller, M. Deicke, and R. W. De Doncker, "Doubly fed induction generator systems for wind turbines," *IEEE Industry Applications Magazine*, vol. 8, no. 3, pp. 26–33, May 2002.

[6] W. Cao, Y. Xie, and Z. Tan, "Wind Turbine Generator Technologies," in *Advances in Wind Power*, R. Carriveau, Ed. IntechOpen, November 2012. [Online]. Available: https://www.intechopen.com/books/advances-in-wind-power/wind-turbine-generator-technologies

[7] J. Carroll, A. McDonald, and D. McMillan, "Reliability comparison of wind turbines with DFIG and PMG drive trains," *IEEE Transactions on Energy Conversion*, vol. 30, no. 2, pp. 663–670, June 2015.

[8] J. Carroll, A. McDonald, I. Dinwoodie, D. McMillan, M. Revie, and I. Lazakis, "Availability, operation and maintenance costs of offshore wind turbines with different drive train configurations," *Wind Energy*, vol. 20, no. 2, pp. 361–378, 2017. [Online]. Available: https://onlinelibrary.wiley.com/doi/abs/10.1002/we.2011

[9] R. Mcmahon, P. Tavner, E. Abdi, P. Malliband, and D. Barker, "Characterising brushless doubly fed machine rotors," *IET Electric Power Applications*, vol. 7, no. 7, pp. 535–543, Aug 2013.

[10] X. Wang, D. Liu, H. Polinder, D. Lahaye, and J. A. Ferreira, "Comparison of nested-loop rotors in brushless doubly-fed induction machines," in *2016 19th International Conference on Electrical Machines and Systems (ICEMS)*, Nov 2016, pp. 1–6.

[11] H. Liu and L. Xu, "Design and performance analysis of a doubly excited brushless machine for wind power generator application," in *The 2nd International Symposium on Power Electronics for Distributed Generation Systems*, June 2010, pp. 597–601.

[12] T. D. Strous, H. Polinder, and J. A. Ferreira, “Brushless doubly-fed induction machines for wind turbines: developments and research challenges,” *IET Electric Power Applications*, vol. 11, no. 6, pp. 991–1000, 2017.

[13] P. C. Roberts, “A study of brushless doubly-fed (induction) machines,” Ph.D. dissertation, University of Cambridge, September 2004.

[14] M. S. Boger, “Aspects of brushless doubly-fed induction machines,” Ph.D. dissertation, University of Cambridge, August 1997.

[15] I. Boldea, *Variable Speed Generators*. Boca Raton, FL, USA: Taylor & Francis, 2006.

[16] I. Boldea and S. Nasar, *The Induction Machines Design Handbook*, 2nd ed., ser. Electric Power Engineering Series. Boca Raton, FL, USA: Taylor & Francis, 2009.

[17] H. A. Toliyat and G. B. Kliman, *Handbook of Electric Motors*, 2nd ed. Boca Raton, FL, USA: CRC Press, 2004.

[18] J. Pyrhönen, T. Jokinen, and V. Hrabovcová, *Design of Rotating Electrical Machines*, 2nd ed. Chichester, U.K.: John Wiley & Sons, Ltd, 2014.

[19] A. Oraee, E. Abdi, S. Abdi, R. McMahon, and P. J. Tavner, “Effects of rotor winding structure on the BDFM equivalent circuit parameters,” *IEEE Transactions on Energy Conversion*, vol. 30, no. 4, pp. 1660–1669, Dec 2015.

[20] T. G. Logan, R. A. McMahon, P. J. Tavner, and S. Tohidi, “A comparison of cage and nested-loop BDFM rotors,” in *6th IET International Conference on Power Electronics, Machines and Drives (PEMD 2012)*, March 2012, pp. 1–6.

[21] S. Abdi, A. Grace, E. Abdi, and R. McMahon, “A new optimized rotor design for brushless doubly fed machines,” in *2017 20th International Conference on Electrical Machines and Systems (ICEMS)*, Aug 2017, pp. 1–6.

[22] R. A. McMahon, P. C. Roberts, X. Wang, and P. J. Tavner, “Performance of BDFM as generator and motor,” *IEE Proceedings - Electric Power Applications*, vol. 153, no. 2, pp. 289–299, March 2006.

[23] T. D. Strous, U. Shipurkar, H. Polinder, and J. A. Ferreira, “Comparing the brushless DFIM to other generator systems for wind turbine drive-trains,” *Journal of Physics: Conference Series*, vol. 753, no. 11, p. 112014, 2016. [Online]. Available: http://stacks.iop.org/1742-6596/753/i=11/a=112014

[24] E. Abdi, R. Mcmahon, P. Malliband, S. Shao, M. E. Mathekga, P. Tavner, S. Abdi, A. Oraee, T. Long, and M. Tatlow, “Performance analysis and testing of a 250 kw medium-speed brushless doubly-fed induction generator,” *IET Renewable Power Generation*, vol. 7, no. 6, pp. 631–638, Nov 2013.

[25] E. Abdi, M. R. Tatlow, R. A. McMahon, and P. Tavner, “Design and performance analysis of a 6 mw medium-speed brushless DFIG,” in *2nd IET Renewable Power Generation Conference (RPG 2013)*, Beijing, China, Sept 2013, pp. 1–4.

[26] H. Gorginpour, H. Oraee, and R. A. McMahon, “Electromagnetic-thermal design optimization of the brushless doubly fed induction generator,” *IEEE Transactions on Industrial Electronics*, vol. 61, no. 4, pp. 1710–1721, April 2014.

[27] F. Zhang, S. Yu, H. Wang, Y. Wang, and D. Wang, “Overview of research and development status of brushless doubly-fed machine system,” *Chinese Journal of Electrical Engineering*, vol. 2, no. 2, pp. 1–13, 2016.

[28] P. Han, M. Cheng, S. Ademi, and M. G. Jovanovic, “Brushless doubly-fed machines: Opportunities and challenges,” *Chinese Journal of Electrical Engineering*, vol. 4, no. 2, pp. 1–17, June 2018.

[29] L. Bell, “Some facts about polyphase motors,” *Transactions of the American Institute of Electrical Engineers*, vol. XI, pp. 559–569, 1894.

[30] A. D. Adams, “Motor speed regulation,” *Transactions of the American Institute of Electrical Engineers*, vol. XVI, pp. 443–445, 1899.

[31] C. F. Scott, “Variable speed motor control,” *Transactions of the American Institute of Electrical Engineers*, vol. XX, pp. 111–114, 1902.

[32] H. W. Leonard, “Volts vs. ohms; speed regulation of electric motors,” *Transactions of the American Institute of Electrical Engineers*, vol. XIII, pp. 373–386, 1896.

[33] L. J. Hunt, “The ”cascade” induction motor,” *Journal of the Institution of Electrical Engineers*, vol. 52, no. 230, pp. 406–426, March 1914.

[34] Siemens Brothers & Co. Ltd and F. Lydall, “Improvements in polyphase induction motors,” British Patent 16 839, July, 1902.

[35] L. J. Hunt, “A new type of induction motor,” *Electrical Engineers, Journal of the Institution of*, vol. 39, no. 186, pp. 648–667, September 1907.

[36] C. P. Steinmetz, “Operating alternating motors,” Patent US 587 340 A, Aug. 3, 1897, US Patent 587,340. [Online]. Available: https://www.google.com/patents/US587340

[37] F. Creedy, “Some developments in multi-speed cascade induction motors,” *Electrical Engineers, Journal of the Institution of*, vol. 59, no. 301, pp. 511–532, May 1921.

[38] A. R. W. Broadway and L. Burbridge, “Self-cascaded machine: a low-speed motor or high-frequency brushless alternator,” *Electrical Engineers, Proceedings of the Institution of*, vol. 117, no. 7, pp. 1277–1290, July 1970.

[39] B. H. Smith, "Theory and performance of a twin stator induction machine," *IEEE Transactions on Power Apparatus and Systems*, vol. PAS-85, no. 2, pp. 123–131, Feb 1966.

[40] ——, "Synchronous behavior of doubly fed twin stator induction machine," *IEEE Transactions on Power Apparatus and Systems*, vol. PAS-86, no. 10, pp. 1227–1236, Oct 1967.

[41] A. K. Wallace, R. Spee, and H. K. Lauw, "Dynamic modeling of brushless doubly-fed machines," in *Conference Record of the IEEE Industry Applications Society Annual Meeting,*, San Diego, CA, USA, Oct 1989, pp. 329–334 vol.1.

[42] C. S. Brune, R. Spee, and A. K. Wallace, "Experimental evaluation of a variable-speed, doubly-fed wind-power generation system," *IEEE Transactions on Industry Applications*, vol. 30, no. 3, pp. 648–655, May 1994.

[43] T. Logan, J. Warrington, S. Shao, and R. McMahon, "Practical deployment of the brushless doubly-fed machine in a medium scale wind turbine," in *2009 International Conference on Power Electronics and Drive Systems (PEDS)*, Nov 2009, pp. 470–475.

[44] P. Rochelle, R. Spee, and A. K. Wallace, "The effect of stator winding configuration on the performance of brushless doubly-fed machines in adjustable speed drives," in *Conference Record of the 1990 IEEE Industry Applications Society Annual Meeting*, Seattle, WA, USA, Oct 1990, pp. 331–337 vol.1.

[45] A. Oraee, E. Abdi, and R. A. McMahon, "Converter rating optimisation for a brushless doubly fed induction generator," *IET Renewable Power Generation*, vol. 9, no. 4, pp. 360–367, 2015.

[46] R. A. McMahon, E. Abdi, P. D. Malliband, S. Shao, M. E. Mathekga, and P. J. Tavner, "Design and testing of a 250 kw medium-speed brushless dfig," in *6th IET International Conference on Power Electronics, Machines and Drives (PEMD 2012)*, March 2012, pp. 1–6.

[47] R. A. McMahon, M. E. Mathekga, X. Wang, and M. R. Tatlow, "Design considerations for the brushless doubly-fed (induction) machine," *IET Electric Power Applications*, vol. 10, no. 5, pp. 394–402, 2016.

[48] F. Rüncos, R. Carlson, N. Sadowski, and P. Kuo-Peng, "Performance analysis of a doubly fed twin stator cage induction generator," in *Recent Developments of Electrical Drives*. Dordrecht: Springer Netherlands, 2006, pp. 361–373.

[49] A. Oraee, R. McMahon, E. Abdi, S. Abdi, and S. Ademi, "Influence of pole-pair combinations on the characteristics of the brushless doubly fed induction generator," *IEEE Transactions on Energy Conversion*, pp. 1–1, 2020.

[50] P. C. Roberts, T. Long, R. A. Mcmahon, S. Shao, E. Abdi, and J. M. Maciejowski, "Dynamic modelling of the brushless doubly fed machine," *IET Electric Power Applications*, vol. 7, no. 7, pp. 544–556, Aug 2013.

[51] A. Kusko and C. B. Somuah, “Speed control of a single-frame cascade induction motor with slip-power pump back,” *IEEE Transactions on Industry Applications*, vol. IA-14, no. 2, pp. 97–105, March 1978.

[52] H. Gorginpour, H. Oraee, and E. Abdi, “Calculation of core and stray load losses in brushless doubly fed induction generators,” *IEEE Transactions on Industrial Electronics*, vol. 61, no. 7, pp. 3167–3177, July 2014.

[53] F. Chapman, “The production of noise and vibration by certain squirrel-cage induction motors,” *Journal of the Institution of Electrical Engineers*, vol. 61, pp. 39–48(9), December 1922. [Online]. Available: https://digital-library.theiet.org/content/journals/10.1049/jiee-1.1922.0108

[54] S. Abdi, E. Abdi, and R. McMahon, “A study of unbalanced magnetic pull in brushless doubly fed machines,” *IEEE Transactions on Energy Conversion*, vol. 30, no. 3, pp. 1218–1227, 2015.

[55] N. H. van der Blij, T. D. Strous, X. Wang, and H. Polinder, “A novel analytical approach and finite element modelling of a BDFIM,” in *2014 International Conference on Electrical Machines (ICEM)*, Sept 2014, pp. 346–352.

[56] E. Abdi, A. Oraee, S. Abdi, and R. A. McMahon, “Design of the brushless DFIG for optimal inverter rating,” in *7th IET International Conference on Power Electronics, Machines and Drives (PEMD 2014)*, April 2014, pp. 1–6.

[57] T. D. Strous, X. Wang, H. Polinder, and J. A. B. Ferreira, “Finite element based multi-objective optimization of a brushless doubly-fed induction machine,” in *2015 IEEE International Electric Machines Drives Conference (IEMDC)*, May 2015, pp. 1689–1694.

[58] X. Wang, H. Polinder, D. Lahaye, and J. A. Ferreira, “FE based multi-objective optimization of a 3.2 MW brushless doubly-fed induction machine,” in *2017 IEEE Workshop on Electrical Machines Design, Control and Diagnosis (WEMDCD)*, April 2017, pp. 89–94.

[59] T. D. Strous, X. Wang, H. Polinder, and J. A. Ferreira, “Evaluating harmonic distortions in brushless doubly fed induction machines,” *IEEE Transactions on Magnetics*, vol. 53, no. 1, pp. 1–10, Jan 2017.

[60] X. Wang, T. D. Strous, D. Lahaye, H. Polinder, and J. A. Ferreira, “Modeling and optimization of brushless doubly-fed induction machines using computationally efficient finite-element analysis,” *IEEE Transactions on Industry Applications*, vol. 52, no. 6, pp. 4525–4534, Nov 2016.

[61] F. Xiong and X. Wang, “Design of a low-harmonic-content wound rotor for the brushless doubly fed generator,” *IEEE Transactions on Energy Conversion*, vol. 29, no. 1, pp. 158–168, March 2014.

[62] A. Wallace, P. Rochelle, and R. Spee, “Rotor modeling and development for brushless doubly-fed machines,” *Electric Machines & Power Systems*, vol. 23, no. 6, pp. 703–715, 1995.

[63] O. I. Olubamiwa, N. Gule, and M. J. Kamper, "Coupled circuit analysis of the brushless doubly fed machine using the winding function theory," *IET Electric Power Applications*, vol. 14, pp. 1558–1569(11), September 2020. [Online]. Available: https://digital-library.theiet.org/content/journals/10.1049/iet-epa.2019.0915

[64] S. Abdi, E. Abdi, A. Oraee, and R. McMahon, "Optimization of magnetic circuit for brushless doubly fed machines," *IEEE Transactions on Energy Conversion*, vol. 30, no. 4, pp. 1611–1620, Dec 2015.

[65] S. Abdi, E. Abdi, A. Oraee, and R. A. McMahon, "Investigation of magnetic wedge effects in large-scale bdfms," in *2nd IET Renewable Power Generation Conference (RPG 2013)*, 2013, pp. 1–4.

[66] T. Logan, R. Mcmahon, and K. Seffen, "Noise and vibration in brushless doubly fed machine and brushless doubly fed reluctance machine," *IET Electric Power Applications*, vol. 8, no. 2, pp. 50–59, February 2014.

[67] T. D. Strous, X. Wang, H. Polinder, and J. A. B. Ferreira, "Brushless doubly-fed induction machines: Torque ripple," in *2015 IEEE International Electric Machines Drives Conference (IEMDC)*, 2015, pp. 1145–1151.

[68] J. Chen and W. Zhang, "Harmonics in brushless doubly fed induction generator for torque ripple analysis and modeling," *IEEE Transactions on Magnetics*, vol. 50, no. 11, pp. 1–4, 2014.

[69] H. Gorginpour, B. Jandaghi, A. Oraee, M. A. Saket, M. Ahmadian, and H. Oraee, "Reduction of the torque ripple in brushless doubly-fed machine," in *Proceedings of the 2011 3rd International Youth Conference on Energetics (IYCE)*, 2011, pp. 1–7.

[70] X. Wang, T. D. Strous, D. Lahaye, H. Polinder, and J. A. Ferreira, "Effects of rotor skew on the performance of brushless doubly-fed induction machine," in *2015 IEEE International Electric Machines Drives Conference (IEMDC)*, 2015, pp. 260–265.

[71] P. C. Roberts, R. A. McMahon, P. J. Tavner, J. M. Maciejowski, and T. J. Flack, "Equivalent circuit for the brushless doubly fed machine (bdfm) including parameter estimation and experimental verification," *IEE Proceedings - Electric Power Applications*, vol. 152, no. 4, pp. 933–942, July 2005.

[72] Y.-H. Chang, Y.-T. Li, I.-H. Lin, and M.-F. Hsieh, "A design approach integrating the magnetic circuit and electric circuit models for bdfim," in *2014 17th International Conference on Electrical Machines and Systems (ICEMS)*, 2014, pp. 1685–1690.

[73] M. F. Hsieh, I. H. Lin, Y. C. Hsu, and R. A. McMahon, "Design of brushless doubly-fed machines based on magnetic circuit modeling," *IEEE Transactions on Magnetics*, vol. 48, no. 11, pp. 3017–3020, Nov 2012.

[74] H. Gorginpour, H. Oraee, and R. A. McMahon, “A novel modeling approach for design studies of brushless doubly fed induction generator based on magnetic equivalent circuit,” *IEEE Transactions on Energy Conversion*, vol. 28, no. 4, pp. 902–912, Dec 2013.

[75] X. Wang, P. C. Roberts, and R. A. McMahon, “Optimisation of BDFM stator design using an equivalent circuit model and a search method,” in *The 3rd IET International Conference on Power Electronics, Machines and Drives, 2006. PEMD 2006*, April 2006, pp. 606–610.

[76] X. Wang, R. A. McMahon, and P. J. Tavner, “Design of the brushless doubly-fed (induction) machine,” in *2007 IEEE International Electric Machines Drives Conference*, vol. 2, May 2007, pp. 1508–1513.

[77] X. Wang, T. D. Strous, D. Lahaye, H. Polinder, and J. A. Ferreira, “Finite element modeling of brushless doubly-fed induction machine based on magneto-static simulation,” in *2015 IEEE International Electric Machines Drives Conference (IEMDC)*, May 2015, pp. 315–321.

[78] S. Umans, A. Fitzgerald, and C. Kingsley, *Electric Machinery: Seventh Edition*. New York, USA: McGraw-Hill Higher Education, 2013.

[79] R. Spee, A. K. Wallace, and H. K. Lauw, “Performance simulation of brushless doubly-fed adjustable speed drives,” in *Conference Record of the IEEE Industry Applications Society Annual Meeting,*, vol. 1, San Diego, CA, USA, Oct 1989, pp. 738–743.

[80] A. R. Munoz and T. A. Lipo, “Dual stator winding induction machine drive,” *IEEE Transactions on Industry Applications*, vol. 36, no. 5, pp. 1369–1379, Sep 2000.

[81] Z. Wu and O. Ojo, “Coupled-circuit-model simulation and airgap-field calculation of a dual-stator-winding induction machine,” *IEE Proceedings - Electric Power Applications*, vol. 153, no. 3, pp. 387–400, May 2006.

[82] T. A. Lipo, *Analysis of Synchronous Machines*. Boca Raton, FL, USA: CRC Press, 2012.

[83] H. A. Toliyat, T. A. Lipo, and J. C. White, “Analysis of a concentrated winding induction machine for adjustable speed drive applications. i. motor analysis,” *IEEE Transactions on Energy Conversion*, vol. 6, no. 4, pp. 679–683, Dec 1991.

[84] H. A. Toliyat and T. A. Lipo, “Transient analysis of cage induction machines under stator, rotor bar and end ring faults,” *IEEE Transactions on Energy Conversion*, vol. 10, no. 2, pp. 241–247, Jun 1995.

[85] N. Gule and M. J. Kamper, “Evaluation of rotor bar and end ring current waveform of brush dc equivalent controlled multiphase cage rotor induction machine,” in *2012 XXth International Conference on Electrical Machines*, Marseille, France, Sep. 2012, pp. 946–952.

[86] H. Gorginpour, H. Oraee, and R. McMahon, “Performance description of brushless doubly-fed induction machine in its asynchronous and variable speed synchronous modes,” *Journal of Electromagnetic Analysis and Applications*, vol. 3, no. 12, pp. 490–511, 2011.

[87] M. Tsili and S. Papathanassiou, “A review of grid code technical requirements for wind farms,” *IET Renewable Power Generation*, vol. 3, no. 3, pp. 308–332, Sep. 2009.

[88] O. I. Olubamiwa and N. Gule, “Prioritizing power factor in power density assessments of doubly fed induction generator alternatives,” in *2020 International Symposium on Power Electronics, Electrical Drives, Automation and Motion (SPEEDAM)*, 2020, pp. 47–52.

[89] A. Izanlo, S. E. Abdollahi, and S. A. Gholamian, “A new method for design and optimization of DFIG for wind power applications,” *Electric Power Components and Systems*, vol. 48, no. 14-15, pp. 1523–1536, 2020. [Online]. Available: https://doi.org/10.1080/15325008.2020.1856231

[90] H. Li and Z. Chen, “Design optimization and evaluation of different wind generator systems,” in *2008 International Conference on Electrical Machines and Systems*, 2008, pp. 2396–2401.

[91] H. Dehnavifard, M. A. Khan, and P. S. Barendse, “Development of a 5-kw scaled prototype of a 2.5 mw doubly-fed induction generator,” *IEEE Transactions on Industry Applications*, vol. 52, no. 6, pp. 4688–4698, Nov 2016.

[92] O. I. Olubamiwa and N. Gule, “The optimal design and autonomous testing of a rotor-tied DFIG,” in *2017 IEEE AFRICON*, Sept 2017, pp. 1378–1383.

[93] Zest Weg group. (2019, October) Electric motor price list. [Online]. Available: https://www.zestweg.com/assets/documents/product-categories/electric-motors/low-voltage-motors/Electric-Motor-Price-List-October-2019.pdf

[94] Y.-M. You, T. A. Lipo, and B.-I. Kwon, “Design and Analysis of a Novel Grid-Connected to Rotor Type Doubly Fed Induction Machine,” *IEEE Transactions on Magnetics*, vol. 48, no. 2, pp. 919–922, 2012.

[95] ——, “A Novel Grid-connected to Rotor Type Doubly Fed Induction Generator for Wind Turbine Systems,” in *8th International Conference on Power Electronics - ECCE Asia*, The Shilla Jeju, 2011, pp. 646–653.

[96] O. I. Olubamiwa and N. Gule, “The steady state operation of a rotor-tied doubly fed induction generator,” in *SAUPEC 2017*, January 2017, pp. 595 – 600. [Online]. Available: www.researchgate.net/publication/315752765

[97] Y.-M. You, T. A. Lipo, and B.-I. Kwon, “Optimal Design of a Grid-Connected-to-Rotor Type Doubly Fed Induction Generator for Wind Turbine Systems,” *IEEE Transactions on Magnetics*, vol. 48, no. 11, pp. 3124–3127, 2012.

[98] T. D. Strous, X. Wang, H. Polinder, and J. A. B. Ferreira, “Brushless doubly fed induction machines: Magnetic field analysis,” *IEEE Transactions on Magnetics*, vol. 52, no. 11, pp. 1–10, Nov 2016.

[99] T. D. Strous, X. Wang, H. Polinder, and J. A. Ferreira, “Saturation in brushless doubly-fed induction machines,” in *8th IET International Conference on Power Electronics, Machines and Drives (PEMD 2016)*, April 2016, pp. 1–7.

[100] O. I. Olubamiwa and N. Gule, “Design and optimization of a cage + nested loops rotor bdfm,” in *2020 International Conference on Electrical Machines (ICEM)*, vol. 1, 2020, pp. 1868–1874.

[101] G. Bramerdorfer, J. A. Tapia, J. J. Pyrhönen, and A. Cavagnino, “Modern electrical machine design optimization: Techniques, trends, and best practices,” *IEEE Transactions on Industrial Electronics*, vol. 65, no. 10, pp. 7672–7684, 2018.

[102] Z. Tan, X. Song, W. Cao, Z. Liu, and Y. Tong, “DFIG Machine Design for Maximizing Power Output Based on Surrogate Optimization Algorithm,” *IEEE Transactions on Energy Conversion*, vol. 30, no. 3, pp. 1154–1162, 2015.

[103] J. Gong, F. Gillon, J. T. Canh, and Y. Xu, “Proposal of a kriging output space mapping technique for electromagnetic design optimization,” *IEEE Transactions on Magnetics*, vol. 53, no. 6, pp. 1–4, 2017.

[104] ANSYS, *ANSYS DesignXplorer User’s Guide*, ANSYS, 2019. [Online]. Available: https://ansyshelp.ansys.com/Views/Secured/corp/v193/wb_dx/dxbook.html

[105] K. Wiesen, J. Teubler, and H. Rohn, “Resource use of wind farms in the german north sea - the example of alpha ventus and bard offshore i,” *Resources*, vol. 2, no. 4, pp. 504–516, 2013. [Online]. Available: https://www.mdpi.com/2079-9276/2/4/504

[106] “BARD VM.” [Online]. Available: https://en.wind-turbine-models.com/turbines/6-bard-vm

[107] V. Yaramasu and B. Wu, *Control of DFIG WECS with Voltage Source Converters*. John Wiley & Sons, Ltd, 2017, ch. 12, pp. 403–436. [Online]. Available: https://onlinelibrary.wiley.com/doi/abs/10.1002/9781119082989.ch12

[108] S. Chapman, *Electric Machinery Fundamentals*, 5th ed., ser. McGraw-Hill Series in Electrical and Computer Engineering. McGraw-Hill Corp., New york, USA 2012.

[109] S. Williamson and M. S. Boger, “Impact of inter-bar currents on the performance of the brushless doubly fed motor,” *IEEE Transactions on Industry Applications*, vol. 35, no. 2, pp. 453–460, Mar 1999.

[110] J. Poza, E. Oyarbide, and D. Roye, “New vector control algorithm for brushless doubly-fed machines,” in *IEEE 2002 28th Annual Conference of the Industrial Electronics Society. IECON 02*, vol. 2, 2002, pp. 1138–1143 vol.2.

[111] T. Hutton and N. Gule, “Simplified vector control of a nested-loop rotor brush-less doubly fed induction motor,” in *2020 International Symposium on Power Electronics, Electrical Drives, Automation and Motion (SPEEDAM)*, 2020, pp. 53–58.

[112] O. I. Olubamiwa and N. Gule, “Rotor selection for brushless doubly fed machines using coupled circuit models,” in *Southern African Sustainable Energy Conference (SASEC 2021)*, 2021.

Appendices

Appendix A

Power and efficiency calculation from FEA simulations

These are the equations used in calculating the grid side power factor, total generating/motoring output power and efficiency from simulations. The output power and efficiency values are calculated at the rated maximum speed of the machines. This is because DFIGs/BDFMs operate at rated output power at these speeds.

A.1 Power factor calculations

In generating regions, the input (grid) voltages and current in the PW are transformed to the synchronous dq reference frame as given in [5]. The transformed voltages and currents are calculated as

$$V_d = \frac{2}{3}\left(V_a cos\theta + V_b cos(\theta - \frac{2\pi}{3}) + V_c cos(\theta + \frac{2\pi}{3})\right), \tag{A.1.1}$$

$$V_q = \frac{2}{3}\left(-V_a cos\theta - V_b cos(\theta - \frac{2\pi}{3}) - V_c cos(\theta + \frac{2\pi}{3})\right), \tag{A.1.2}$$

$$I_d = \frac{2}{3}\left(I_a cos\theta + I_b cos(\theta - \frac{2\pi}{3}) + I_c cos(\theta + \frac{2\pi}{3})\right), \tag{A.1.3}$$

$$I_q = \frac{2}{3}\left(-I_a cos\theta - I_b cos(\theta - \frac{2\pi}{3}) - I_c cos(\theta + \frac{2\pi}{3})\right), \tag{A.1.4}$$

where, $V_{a,b,c}$ are input (grid) PW voltages for phases a, b and c in a 3-phase winding, $I_{a,b,c}$ are currents in the phases, and $\theta = 2\pi f t$. The PW reactive power and real power (P_{pw} & Q_{pw}) are then calculated as

$$P_{pw} = \frac{3}{2}(V_d I_d + V_q I_q), \tag{A.1.5}$$

$$Q_{pw} = \frac{3}{2}(V_q I_d - V_d I_q). \tag{A.1.6}$$

The apparent power (S) is calculated as

$$S_{pw} = \sqrt{P_{pw}^2 + Q_{pw}^2}. \tag{A.1.7}$$

From (A.1.7), the grid side power factor (pf) is calculated as

$$pf = \frac{P_{pw}}{S_{pw}}. \tag{A.1.8}$$

A.2 Power and efficiency calculations

Neglecting mechanical losses, the total input power (P_{in}) from a wind turbine is calculated as

$$P_{in} = T_e * \omega_r, \tag{A.2.1}$$

where, T_e is the developed electromagnetic torque, and ω_r is the mechanical angular speed. The total generated output power (P_t) as calculated in [23, 108] is

$$P_t = P_{in} - Losses, \tag{A.2.2}$$

where, Losses includes the copper losses from the stator and rotor windings, and the core losses.

In motoring regions, the total output power (P_t) is calculated as

$$P_t = T_e * \omega_r. \tag{A.2.3}$$

The input power in the motoring region (P_{in}) is calculated as

$$P_{in} = P_t + Losses. \tag{A.2.4}$$

The total efficiency (Ef) in either generating or motoring mode is then calculated as

$$\mathrm{Ef}(\%) = \frac{P_t}{P_{in}} * 100. \tag{A.2.5}$$

Appendix B

BDFM Design

The simplification of the BDFM D^2L design coefficient calculation in [47] is outlined here. Equations for the stator and rotor winding parameters are also given.

B.1 The output coefficient (D^2l) calculation

The geometric design of electrical machines commonly starts with the calculation of the D^2l output coefficient. D is the mean airgap diameter, and l is the stack length of the machine. The D^2l for a BDFM can be calculated from a robust formula for the BDFM rated power (P_t) which was initially evaluated in [22], and further developed in [47].

The total BDFM power (P_t) generated at the rated speed (ω_m) can be defined in terms of the maximum PW and CW powers (P_{pw} & P_{cw} respectively) as

$$P_t = P_{pw} + P_{cw}. \tag{B.1.1}$$

ω_m can be calculated using the grid frequency (f_1), and the maximum CW frequency (f_2) as

$$\omega_m = \frac{|\omega_1| + |\omega_2|}{p_1 + p_2}, \tag{B.1.2}$$

where, $\omega_1 = 2\pi f_1$ and $\omega_2 = 2\pi f_2$. At a speed known as the BDFM natural speed (ω_n), where $f_2 = 0$, the total power (P_t) is equal to P_{pw}, because the CW neither absorbs nor generates power ($P_{cw} = 0$). The natural speed (ω_n) is given as

$$\omega_n = \frac{2\pi f_1}{p_1 + p_2}. \tag{B.1.3}$$

In [47], P_t at unity power factor is given as

$$P_t = \frac{\pi^2}{\sqrt{2}} \left(\frac{D}{2}\right)^2 l \omega_m \bar{B} \bar{J} \left(\frac{p_1 + p_2}{p_1(1 + (1/n_r))(1 + n_r(p_2/p_1))} \right), \tag{B.1.4}$$

where, $\bar{B}$ is the specific magnetic loading or average airgap flux density, $\bar{J}$ is the total electric loading in the machine, and n_r is the rotor turns ratio given as

$$n_r = \left(\frac{p_1}{p_2}\right)^{\frac{1}{2}}. \tag{B.1.5}$$

The electric loading of the PW (J_1), as calculated in [47] is given as

$$J_1 = \frac{\bar{J}}{1+(1/n_r)}. \tag{B.1.6}$$

$\bar{B}$ is the specific magnetic loading, and is calculated from the flux densities of the PW and CW denoted as B_1 and B_2 respectively. $\bar{B}$ is calculated in [47] as

$$\bar{B} = \frac{2\sqrt{2}}{\pi}B_{sum}, \tag{B.1.7}$$

$$B_{sum} = B_1 + B_2, \tag{B.1.8}$$

where, B_{sum} is the maximum BDFM airgap flux density, with the relationship between B_1 and B_2 further stated as

$$\frac{B_2}{B_1} = \frac{n_r p_2}{p_1}. \tag{B.1.9}$$

Substituting (B.1.6) - (B.1.9) into (B.1.4) gives,

$$P_t = \frac{\pi D^2 l \omega_m J_1 B_1 (p_1 + p_2)}{2p_1} \tag{B.1.10}$$

As mentioned earlier, at the natural speed (ω_n), P_t = P_{pw}. Therefore, the $D^2 l$ can be calculated at the ω_n using P_{pw} as

$$D^2 l = \frac{2P_{pw}}{\pi \omega_n J_1 B_1}\left(\frac{p_1}{p_1 + p_2}\right). \tag{B.1.11}$$

By substituting (B.1.3) into (B.1.11), we finally get

$$D^2 l = \frac{p_1 P_{pw}}{\pi^2 f_1 J_1 B_1} \tag{B.1.12}$$

The individual values of D and l can be determined from the stack length ratio (λ), which is given as

$$\lambda = \frac{l}{D} \tag{B.1.13}$$

B.2 Stator design

With D and l known, the stator windings parameters can be obtained. The number of stator slots (N_s) is first decided from the lowest common multiple (LCM) of p_1 and p_2 as follows

$$N_s = 2vm(LCM(p_1, p_2)), \quad v = 1, 2, 3....., \tag{B.2.1}$$

where, m is the number of phases in the machine which is typically three. The integer v is an arbitrary integer that is selected to ensure proper coil distribution in a bid to reduce harmonics. The selection of v particularly applies to the PW since it is to be connected to the grid.

With N_s determined, the PW and CW number of turns per phase (N_1 & N_2 respectively) can be calculated from peak PW flux density (B_1) and the peak CW flux density (B_2) respectively. Since a B_1 value is already selected before the calculation of D^2L, the CW peak flux density is calculated from (B.1.9).

The flux ϕ_i produced by winding i ($i = 1, 2$ for the PW and CW respectively) is calculated using its peak flux density B_i as

$$\phi_i = \alpha \tau_i L B_i, \tag{B.2.2}$$

where, α is the flux density shape factor depicting the level of saturation in the winding as given in [16]. The pole pitch (τ_i) for the winding i with p_i pole pairs is given as

$$\tau_i = \frac{\pi D}{2p_i}. \tag{B.2.3}$$

The number of turns per phase N_i in winding i is then calculated as

$$N_i = \frac{V_i}{4.44 k_{wi} f_i \phi_i}, \tag{B.2.4}$$

where, V_i is the voltage in that winding, k_{wi} is the winding factor, and f_i is the voltage frequency. The winding number of turns per slot (n_{s_i}) is calculated using

$$n_{s_i} = \frac{N_i}{p_i q_i}, \tag{B.2.5}$$

where, q_i is the number of slots per pole per phase for the winding.

The PW current I_1 is calculated as

$$I_1 = \frac{P_{pw}}{3V_1}, \tag{B.2.6}$$

while the CW current (I_2) is calculated in [47] as

$$I_2 = \frac{I_1 N_1}{n_r N_2}. \tag{B.2.7}$$

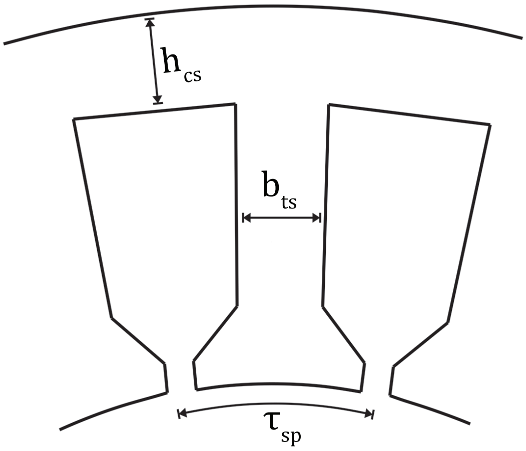

Figure B.1: *Stator slot pitch.*

B.3 Stator slot geometry

A trapezoidal shaped stator slot geometry is illustrated in Figures B.1 & B.2. In Figure B.1, the stator slot pitch and a parallel tooth are illustrated, while different sections/dimensions of the stator slot are illustrated in Figure B.2. The useful slot area (A_{su}) of a slot is calculated using a practically obtainable slot fill factor (k_{fill}) as

$$A_{su} = \frac{A_{pw} + A_{cw}}{4k_{fill}}, \tag{B.3.1}$$

where, A_{pw} & A_{cw} are the combined cross sectional areas of the wire turns of the PW and CW in a slot.

As given in [47], the stator teeth dimension (b_{ts}) is calculated as

$$b_{ts} = \frac{\sqrt{2}\pi D_{si} B_{sum}}{N_s \hat{B}_t}, \tag{B.3.2}$$

where, $\hat{B}_t$ is the peak desired flux density in the teeth. The stator lower slot width (b_{s_1}) is calculated as

$$b_{s_1} = \frac{\pi(D_{si} + 2h_{os} + 2h_w)}{n_s} - b_{ts}, \tag{B.3.3}$$

where, h_{os} is the stator slot opening height and h_w is the stator slot wedge height. Given the trapezoidal shape, the useful slot area can be calculated as:

$$A_{su} = h_s \frac{(b_{s_2} + b_{s_1})}{2}. \tag{B.3.4}$$

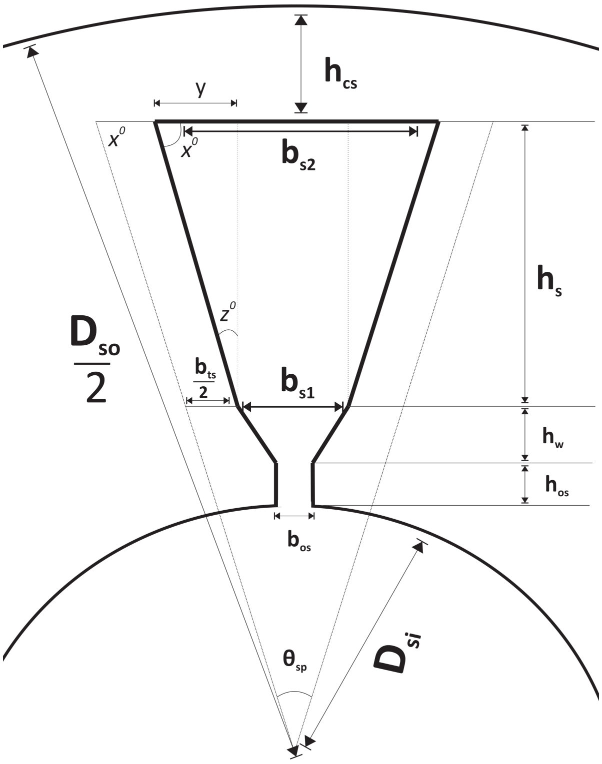

Figure B.2: *Stator slot geometry.*

From the stator slot geometry is illustrated in Figure B.2, the angle z^0 can be calculated from the stator slot pitch angle θ_{sp} as

$$\begin{aligned}\theta_{sp} &= \frac{2\pi}{n_s},\\ z^0 &= \frac{\theta_{sp}}{2} = \frac{\pi}{n_s}.\end{aligned} \tag{B.3.5}$$

The stator upper slot width (b_{s_2}) is calculated as:

$$b_{s_2} = \sqrt{4A_{su}\tan z^0 + b_{s_1}^2}. \tag{B.3.6}$$

The useful slot height, h_s, is then calculated using b_{s_2}, from equation (B.3.4):

$$h_s = \frac{2A_{su}}{b_{s_1} + b_{s_2}}. \tag{B.3.7}$$

The stator/rotor core height h_c is also determined in [47], and is given as

$$h_c = \frac{\sqrt{2}D_{si}}{2\hat{B}_c}\left(\frac{B_1}{p_1} + \frac{B_2}{p_2}\right), \tag{B.3.8}$$

where, $\hat{B_c}$ is the desired peak flux density in the core. It should be noted that the teeth and core dimension calculations are also applicable to the rotor.

Appendix C

Prototype construction

In this Appendix, the step by step construction of a 160L frame BDFM is discussed. The prototype specifications are partially based on the BDFM design process in [100]. A number of workarounds were needed to complete the prototype development, and these are detailed comprehensively alongside the test rig of the prototype. Mechanical drawings of the 160 L frame BDFM constructed are also given. Credit to Kenan Cloete for the Mechanical diagrams .

C.1 Prototyping process

The prototyping process was initiated with the decision to use a standard induction machine frame, instead of building a custom frame for the machine. Although a standard induction machine is not best suited for top heavy BDFMs, building a custom frame adds complications. An empty 160L frame (shown in Figure C.1) is used for the prototype frame, and the inner dimensions were used to limit the the outer stator diameter (D_{so}) and machine stack length (l).

The machine specifications of the prototype are given in Table C.1. As a result of the frame volume constraints, a stack length ratio (λ) of 1.2 is used for the prototype. The PW airgap flux density (B_1) is set at 0.23 T, while the PW electric loading (J_1) used is 13000 kA/m.

C.1.1 Stator construction

The stator lamination is illustrated in Figure C.2. BDFMs with NL rotors have a higher harmonic spectrum compared to conventional IMs [10]. Also, the super-positioning of two field components with different pole numbers results in more vibrations than in machines with single fields [66]. Although, the cage+NL rotor used is expected to reduce the torque ripple compared to the NL rotor, the torque ripple from FEA simulations is still too high. Thus, skewing is used to keep the prototype vibrations low. Based on the accessible methods of

Table C.1: *BDFM prototype specifications*

Parameters	Unit	Value
PW pole pair (p_1)	-	2
CW pole pair (p_2)	-	3
Grid phase voltage (V_1)	V	230
Grid frequency (f_1)	Hz	50
CW max frequency (f_2)	Hz	17.5
Stator slots number (N_s)	-	36
Rotor slots number (N_r)	-	25
PW turns per slot (N_{s_1})	-	47
CW turns per slot (N_{s_2})	-	71
Stack length (l)	mm	200
Outer Stator Diameter	mm	260
Shaft diameter	mm	60

Figure C.1: *Empty 160L frame.*

manufacturing, skewing a rotor with copper bars proved abortive. Therefore, the prototype stator was skewed by one stator slot pitch.

To stack the stator at a skewed angle, a PVC forma is used with a thin piece of metal inserted at the slot pitch angle across it. The metal piece thickness is about the stator slot opening width, and is used as a guide for the skew while stacking the stator laminations. A stacking factor of 97.5 % is achieved for the stator stack. The stator stack was then press fit into the empty frame. The stator is wound with the PW closer to the airgap. Pictures of the stator construction from stacking to winding are shown in Figure C.3.

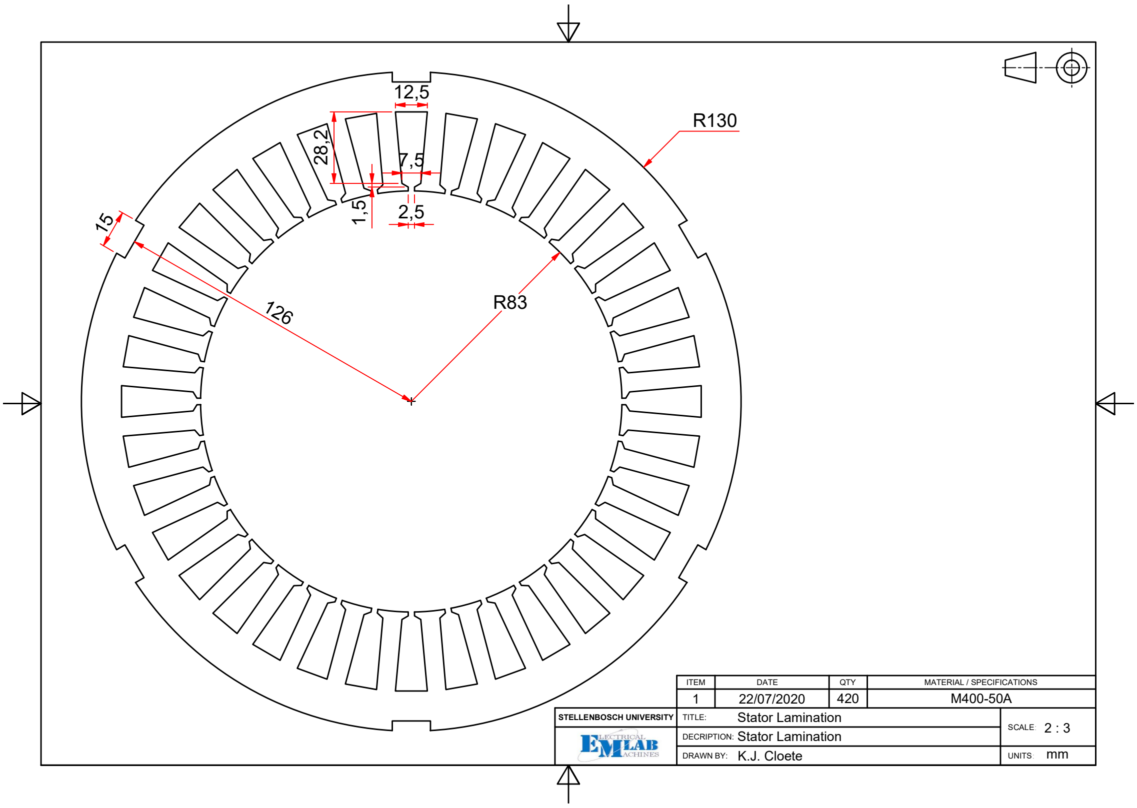

Figure C.2: *Stator Lamination*

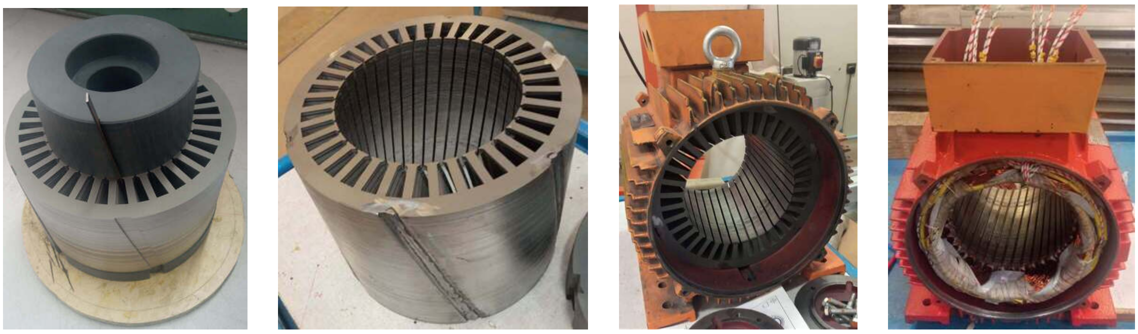

(a) (b) (c) (d)

Figure C.3: *Stator construction: (a) Half stacked laminations (b) Fully stacked laminations (c) Laminations pressed into 160L frame (d) Fully wound stator.*

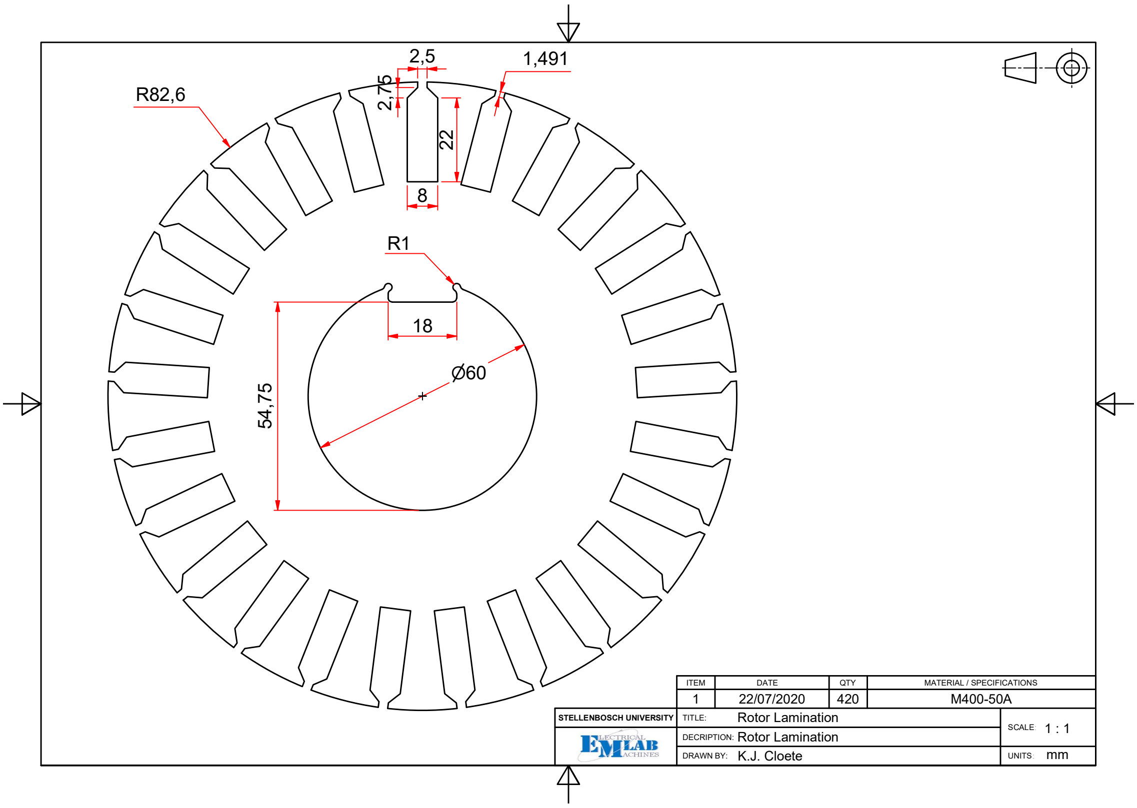

Figure C.4: *Rotor Lamination*

C.1.2 Rotor construction

The cage+NL rotor topology is used for the BDFM prototype. The rotor slots dimensions were based on readily available copper bars (20 x 6.3 mm cross section) that could carry the rotor currents. The rotor lamination is depicted in Figure C.4 with dimensions, while the rotor shaft is illustrated in Figure C.5. A keying feature is added to the rotor laminations to allow the laminations to slide through the keyway cut into the shaft. A stacking factor of 96.3 is achieved for the rotor. Photos of the rotor construction stages are shown in Figure C.6. The bars were insulated from the laminations to prevent rotor inter-bar currents as recommended in [109]. The endrings and loop end-connections are joined to the bars using silver soldering. Silver soldering is used to prevent the insulation from getting damaged. However, some parts of the insulations were burnt and had to be scraped off. It was discovered that the insulations could have been slid through after soldering/welding, as there was enough space in the rotor slots.

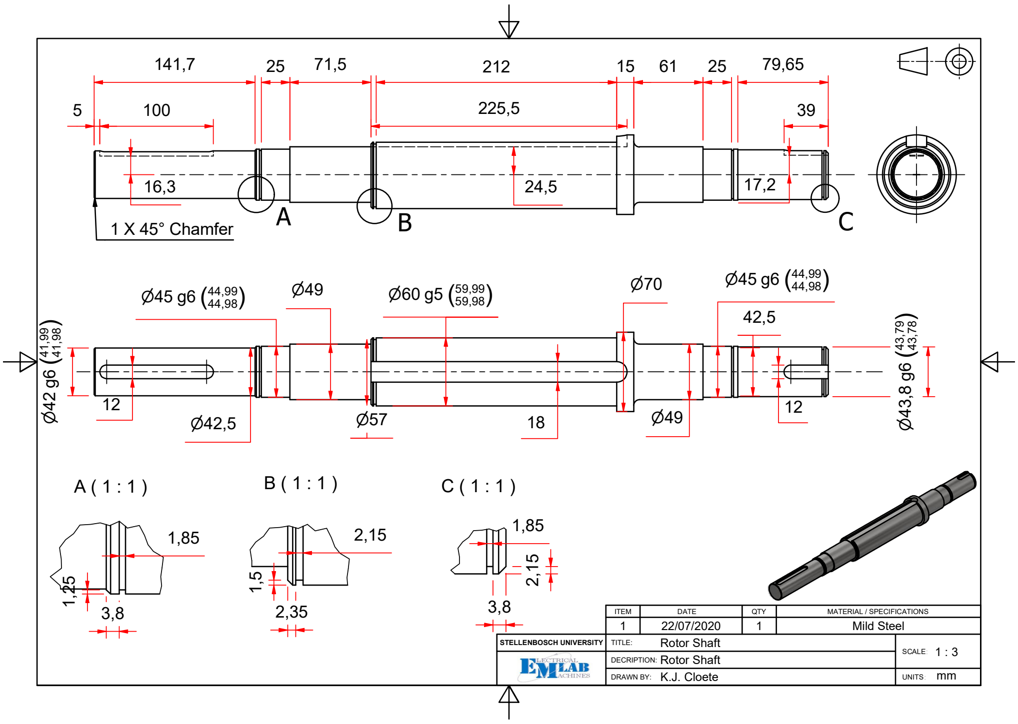

Figure C.5: *Rotor Shaft*

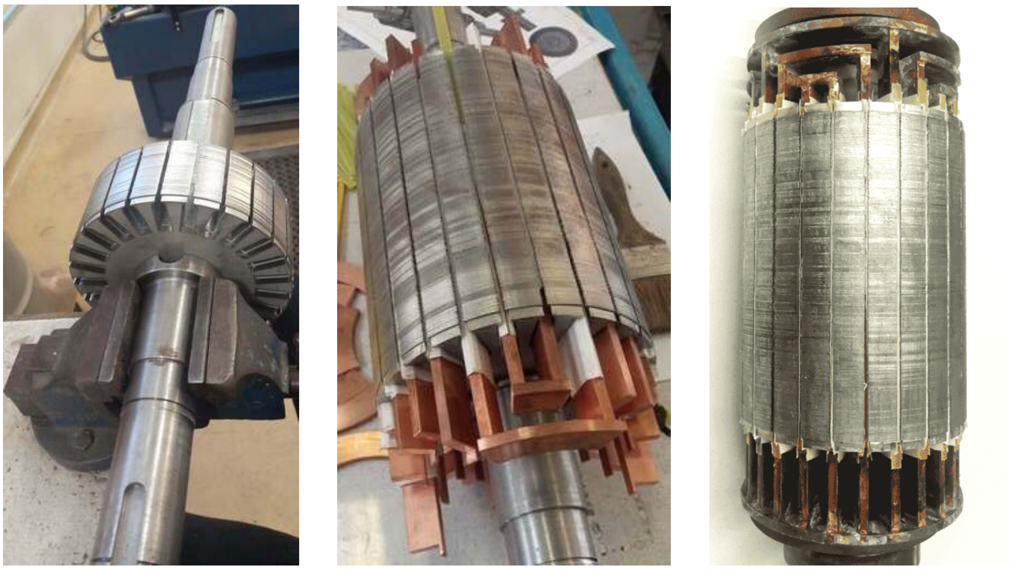
(a) (b) (c)

Figure C.6: *Rotor construction: (a) Half stacked rotor (b) Fully stacked rotor with some inserted bars (c) Completed rotor.*

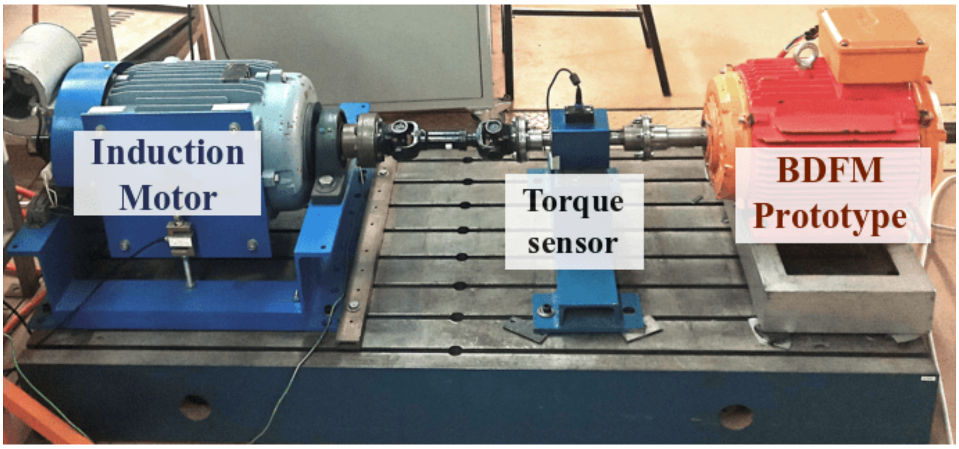

Figure C.7: *BDFM test setup*

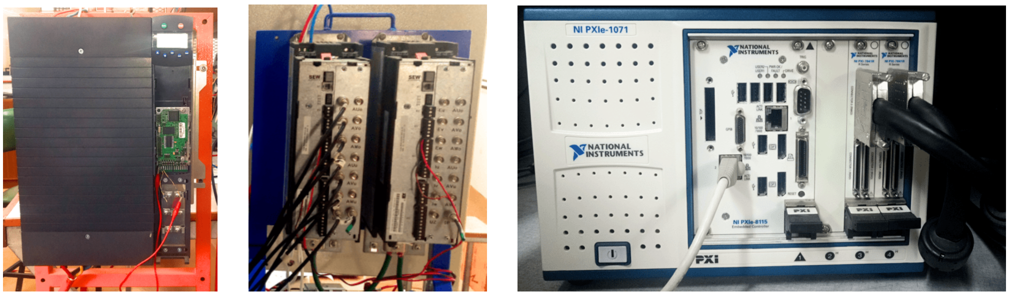

(a) **(b)** **(c)**

Figure C.8: *(a) Bonfiglioli Vectron ACT 401-33A frequency inverter (b) SEW Eurodrive MDX61B-00 inverters (c) National Instruments controller.*

C.2 Prototype test setup

The prototype test bed and equipment used in testing, are shown in Fig. C.8. The BDFM prototype is driven by a 22 kW (180 L) IM. A (Lorenz DR-3000) torque sensor is placed between the IM and the BDFM to determine the input mechanical power to the BDFM. The IM is powered with a Bonfiglioli Vectron ACT 401-33A frequency inverter shown in Fig. C.8(a). SEW Eurodrive MDX61B-00 inverters rated at 8.7 kVA, as shown in Fig. C.8(b), are used to supply controlled slip frequency currents to the BDFM CW. The slip frequency currents are controlled using a National Instruments controller. The controller has a NI PXIe-1071 chassis, with an embedded NI PXIe-8115 controller and two NI PXI-7841R I/O modules. The National Instruments controller is shown in Fig. C.8(c).

The PW currents are measured using LA55-P sensors, while the PW voltages are measured using LEM LV25-P sensors. The CW currents are measured from the filtered current outputs from the SEW Eurodrive inverters. The machine speed and position are obtained using a

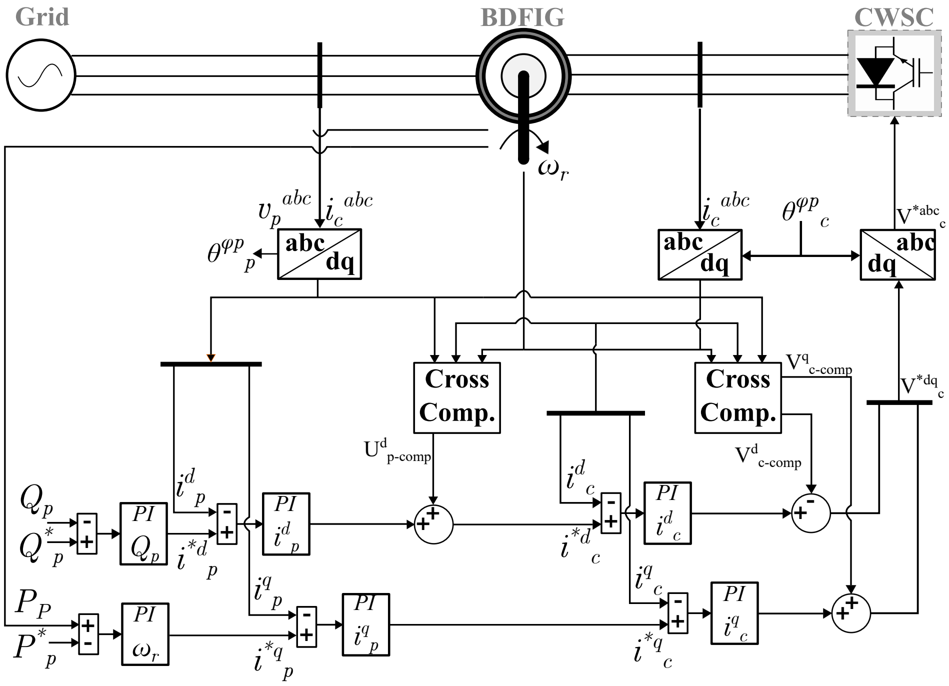

Figure C.9: *Schematic of stator side controller employed.*

GI341 Baumer incremental encoder. The controller is run at a sampling frequency of 5kHz, with data correspondingly recorded at 500Hz.

A vector control approach using cascaded PI controllers as illustrated in Fig. C.9, is employed. CW current control is initialized in the first cascade, from which the PW current control is achieved in the next cascade. From the PW current control, a cascade for power control is derived allowing for the PW side power factor control to be performed. The controller uses machine flux estimates to compensate for non-linearities. These estimates are based on a reduced order dq-model obtained using FEA parameters. The reductions are performed using a technique suggested in [13]. A simplified form of the controller proposed in [110] is then obtained, as discussed in [111].

As mentioned earlier, the input mechanical power to the prototype is measured by the Lorenz torque sensor. The output power generated by the prototype is a product of the PW voltages, currents and power factor. Analog voltmeters and ammeters are connected to the PW terminals for validation. Tests are run at the prototype natural speed of 600 rpm, so it is assumed that the CW neither generates nor absorbs power.

Appendix D

Rotor selection demonstrations using coupled circuit models

D.1 Introduction

In this Appendix[1], the selection process between the nested loops (NL), cage+NL and isolated loops (IL) rotors is examined and demonstrated. Coupled circuit (CC) models are used to evaluate the performances of these rotors as discussed in [63], for BDFM designs at different power ratings (5kW, 75 kW & 250 kW). Different loops per nest are evaluated for each rotor at each power rating. Electromagnetic torque and torque ripple are the output parameters evaluated for each rotor; torque serves as a measure of power output, while the ripple is used to appraise the level of harmonic distortion in the designs. Different pole pair combinations at the selected power ratings are also considered.

D.2 Design specifications and simulations

The power ratings/total power at maximum slip (P_t), the maximum number of loops per nest ($q_{r_{max}}$) at each power rating, and the pole pair combinations considered are given in Table D.1. Loops formed by the bar cage in the cage+NL rotor are regarded similarly to the nested loops. All designs are simulated at 50 Hz and a slip of -0.35. A line voltage of 400 V is used for the designs with power ratings of 5.5 kW & 75 kW, while 525 V is used for the 250 kW designs.

The number of stator slots (N_s), PW flux density (B_1), and electric loading (J_1) for each considered design are given in Table D.2. A stack aspect ratio (λ) of 1 is used for the 5 kW and 75 kW designs, while 1.2 is used for the 250 kW designs.

---

[1] This appendix is based on the accepted local conference paper of Olubamiwa and Gule (2020) [112].

Table D.1: *Initial details of simulated designs*

Power rating (P_t)	$q_{r_{max}}$	p_1/p_2
5.5 kW	4	2/3, 2/4
75 kW	5	2/3, 2/4, 4/6
250 kW	6	2/4, 4/6

Table D.2: *Additional specifications*

P_t	**Stator slots (N_s)**			B_1 **(T)**	J_1 **(kA/m)**	λ
	$2/3$	$2/4$	$4/6$			
5.5 kW	36	48	-	0.25	10	1
75 kW	36	48	72	0.28	17	1
250 kW	-	96	72	0.32	20	1.2

The design methodology used is detailed in [100]. The B_1 and J_1 values used do not necessarily represent optimized values at the selected power ratings. However, the corresponding values were tested with FEA models at the stipulated power ratings for satisfactory performance as recommended in [88].

As mentioned earlier, CC models as detailed in [63], are used to evaluate the performances of the different rotor types for BDFM designs with the listed specifications. The PWs are excited by simulated 3ϕ voltage (grid) sources, while CWs are excited by 3ϕ currents sources to simulate power converters. The CW currents are aligned at ”load angles” relative to the grid voltage. This is done to adjust the outputs of the designs being evaluated, in order to obtain results at desired power factors. Lastly, the CC models are developed in MATLAB®.

D.3 Simulation results and discussion

The torques generated by the 5.5 kW, 75 kW & 250 kW designs are illustrated in Figures D.1, D.3 & D.5 respectively, while the torque ripples of the designs are illustrated in Figures D.2, D.4 & D.6 respectively. The torque and torque ripples [2] are obtained at unity power factor in the synchronous generating mode. The reason for testing at this condition is to provide a comprehensive basis for comparison as explained in [88].

For the 5.5 kW designs, the torques produced by the 3 rotors are close for $p_1/p_2 = 2/3$. The

---

[2] The CC model torque ripple values are not exact ripple values, but are used for comparative purposes.

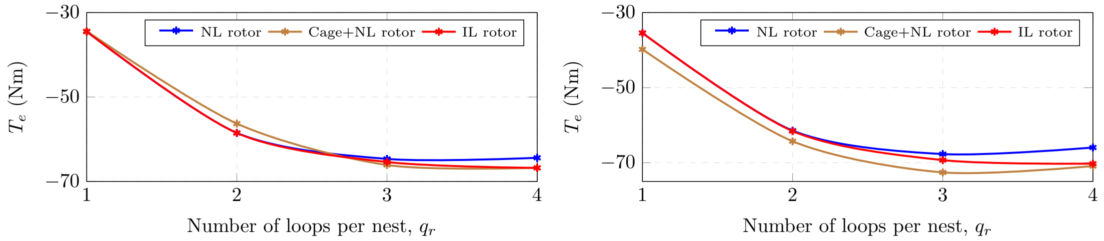

(a) **(b)**

Figure D.1: *Torque generated by 5.5 kW models (a) $p_1/p_2 = 2/3$, (b) $p_1/p_2 = 2/4$.*

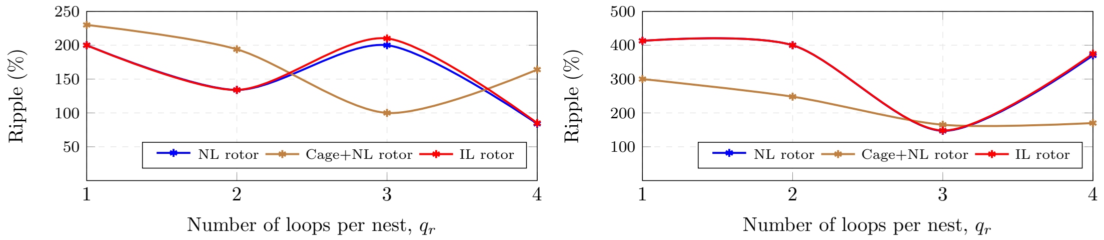

(a) **(b)**

Figure D.2: *Torque ripple of 5.5 kW models (a) $p_1/p_2 = 2/3$, (b) $p_1/p_2 = 2/4$.*

NL and IL rotors with 4 loops have the lowest ripples as illustrated in Figure D.2(a), but the cage+NL rotor with 3 loops has similar ripple and torque. The reduced complexity in fabrication with the cage+NL rotor makes it a preferred rotor topology at this power rating as seen in [100]. For $p_1/p_2 = 2/4$, the cage+NL rotor with 3 loops is also the preferred topology. Although the NL and IL rotors with 3 loops have slightly lower ripples at 2/4 (Figure D.1(b)), the 3 loop cage+NL rotor has higher torque as illustrated in Figure D.1(b).

For the 75 kW designs with $p_1/p_2 = 2/3$, a case for the IL rotor with $q_r = 4$ is apparent. The torque produced with this rotor topology is about the same as the cage+NL counterpart as seen in Figure D.3(a), while the ripple generated is significantly less as illustrated in Figure D.4(a). For $p_1/p_2 = 2/4$, the cage+NL rotor with $q_r = 3$ presents a strong case. The torque produced by this rotor topology is visibly higher than its NL and IL rotor counterparts with very similar ripple as illustrated in Figure D.4(b). In the case of $p_1/p_2 = 4/6$, the IL rotor with $q_r = 4$ is the preferred rotor topology. Although the IL rotor with $q_r = 4$ has similar torque with the cage+NL rotor with $q_r = 4$ as shown in Figure D.3(c), it has significantly less ripple as exhibited in Figure D.4(c), just like in the case of the $p_1/p_2 = 2/3$ combination.

Looking at the 250 kW designs, for $p_1/p_2 = 2/4$, the decision for preferred topology is not clear cut. The cage+NL rotor is the preferred rotor, with $q_r = 3$ & 4 in the mix. The cage+NL rotor with $q_r = 3$ has higher torque as shown in Figure D.5(a), while the cage+NL rotor with $q_r = 4$ has lower ripple as indicated in Figure D.6(a). On the other hand, the rotor topology

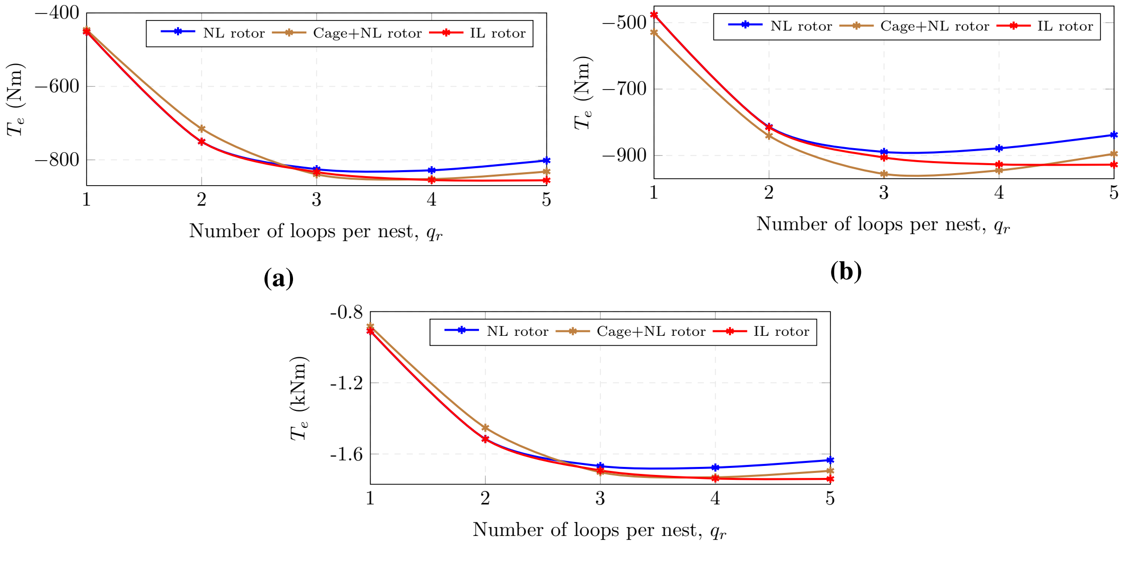

(a) (b) (c)

Figure D.3: *Torque generated by 75 kW models (a)* $p_1/p_2 = 2/3$*, (b)* $p_1/p_2 = 2/4$*, (c)* $p_1/p_2 = 4/6$.

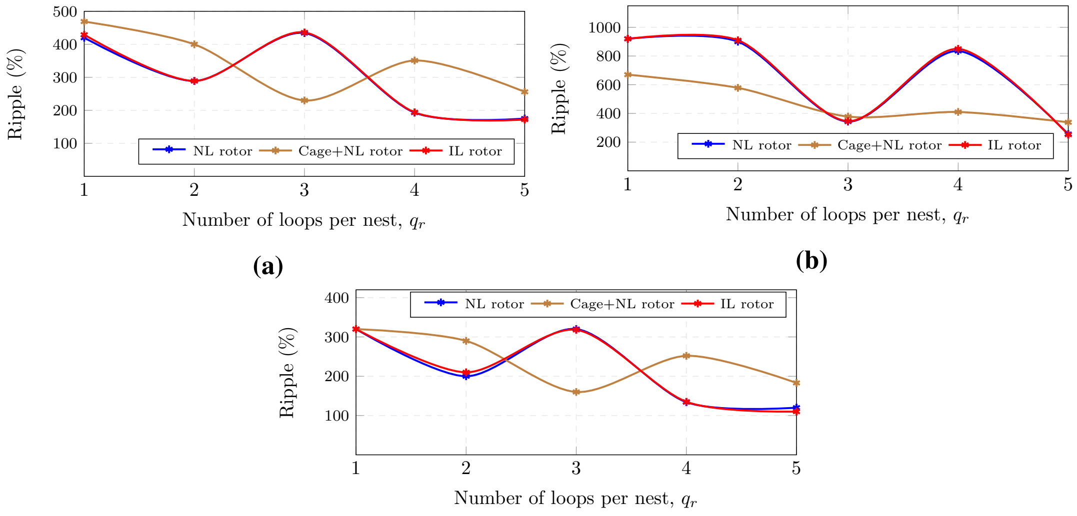

(a) (b) (c)

Figure D.4: *Torque ripple of 75 kW models (a)* $p_1/p_2 = 2/3$*, (b)* $p_1/p_2 = 2/4$*, (c)* $p_1/p_2 = 4/6$.

choice for the $p_1/p_2 = 4/6$ combination is a bit more straightforward. The torque produced by the IL rotor with $q_r = 5$ is the highest torque achieved as illustrated in Figure D.5(b), and the ripple produced by that topology is also the lowest for the pole pair combination as illustrated in Figure D.6(b). Thus, the IL rotor with $q_r = 5$ is the preferred rotor topology for a 250 kW BDFM with $p_1/p_2 = 4/6$.

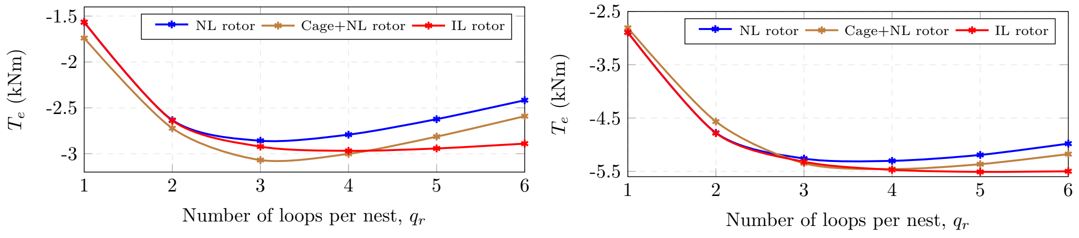

(a) **(b)**

Figure D.5: *Torque generated by 250 kW models (a)* $p_1/p_2 = 2/4$*, (b)* $p_1/p_2 = 4/6$.

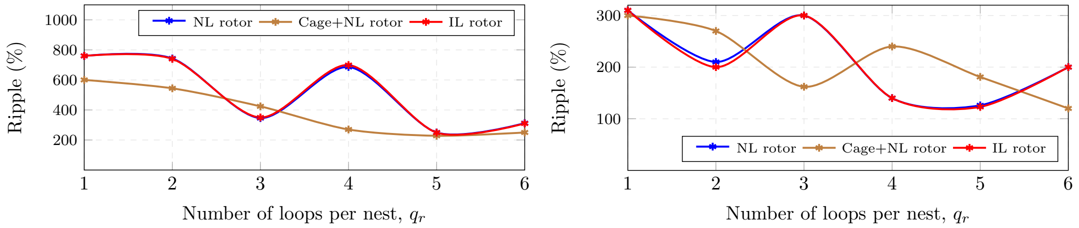

(a) **(b)**

Figure D.6: *Torque ripple of 250 kW models (a)* $p_1/p_2 = 2/4$*, (b)* $p_1/p_2 = 4/6$.

D.4 Conclusion

The selection of suitable rotor topologies of BDFMs has been illustrated. In the selection process, a fast computing CC model is used to determine the performance of three rotor types with different loops per nest for three selected power ratings (5.5 kW, 75 kW & 250 kW). The rotor topologies selection is also investigated across different pole pair combinations at these power ratings.

In terms of torque ripple, the IL rotor is similar to the NL rotor. This is due to similar loop spans of both rotors as detailed in [63]. However, with increasing loops per nest (q_r), the IL rotor has higher torque than the NL rotor for all the power ratings investigated, and at the different pole pair combinations.

In some cases, an IL topology is well placed in terms of torque and ripple, that it is a preferred rotor topology, like in the case of the 250 kW BDFM with a $p_1/p_2 = 4/6$ combination. In other cases investigated in this paper, the cage+NL rotor is the preferred rotor type. In a case like the 250 kW BDFM with a $p_1/p_2 = 2/4$ combination, a bit more analysis like FEA may be required to determine the best choice between the number of loops.

Considering ease of manufacturing, the NL rotor is less elaborate compared to the IL rotor. This is because the NL rotor has a common end ring for all loops, compared to the separate end connections for all loops in the IL rotor. However, it appears that the IL rotor outperforms the NL rotor in bigger machines that require higher q_r. In cases like the 250 kW with

$p_1/p_2 = 2/4$, where the cage+NL rotor is preferred, the choice of q_r can be well down to the ease of manufacturing. Also, in the event of similar preferred performance between the cage+NL and IL rotors which have similar q_r, the cage+NL rotor is less complex with regards to manufacturing.

The 2/4 combination consistently records the highest torque ripple values for all the power ratings tested. The 2/3 pole pair combination torque ripple can be reduced in the 75 kW rating by increasing the number of stator slots, however the effects of UMP may be more pronounced thereby ruling out the combination. It should be noted that the CC model tends to inflate the torque ripple, however the response to q_r changes is comparatively similar to FEA models as illustrated in [63].

Generalizations for every power ratings should not be made based on the results in this paper. There are different design iterations that can still be applied to the instances examined. However, contexts for comparisons have been demonstrated in this paper.